

國立交通大學

光電工程研究所

博士論文

染料敏化太陽電池的金屬氧化物光電極中電子傳遞機

制之研究

1896

**Study on Electron Transport Mechanism in Metal  
Oxide Photoanode Electrode for Dye-Sensitized Solar  
Cells**

研究生：邱偉豪

指導教授：謝文峰 教授

中華民國一百年八月

染料敏化太陽電池的金屬氧化物光電極中電子傳遞機  
制之研究

**Study on Electron Transport Mechanism in Metal  
Oxide Photoanode Electrode for Dye-Sensitized Solar  
Cells**

研 究 生：邱偉豪

Student: Wei-Hao Chiu

指導教授：謝文峰 教授

Advisor: Prof. Wen-Feng Hsieh



A Thesis

Submitted to Institute of Electro-Optical Engineering  
College of Electrical Engineering and  
Computer Science

National Chiao Tung University

In Partial Fulfillment of the Requirements  
for the Degree of

Ph. D.

In

Electro-Optical Engineering

June 2011

Hsin-chu, Taiwan, Republic of China

中華民國一百年八月

# 染料敏化太陽電池的金屬氧化物光電極中電子傳遞機制之 研究

研究生：邱偉豪

指導教授：謝文峰 教授

國立交通大學光電工程研究所

## 摘要

在 2011 年初，原油的價格突破了每桶 110 美元的價格。人們花費越來越多的努力來尋找替代能源，以度過接下來的高油價時代。在這篇論文中主要是探討其中一種替代能源-染料敏化太陽能電池的基礎研究，進而針對染料敏化太陽能電池光電極的結構以及品質進行研究以及探討。

本文的第一部分，首先四針錐狀氧化鋅奈米粉體將被使用於染敏太陽電池之光電極以提供有效率之電子傳遞。在 AM1.5 的光源量測下，以厚度為 42 微米之氧化鋅作為光電極的電池表現出最高效率 4.9%，而其短路電流、開路電壓以及填充因子分別為  $12.3 \text{ mA cm}^{-2}$ 、0.6 V 和 0.65。藉由交流阻抗分析技術，我們發現四針錐狀氧化鋅奈米結構

之光電極有 46 微米的有效電子擴散長度，此結果也與短路電流之相關量測結果一致。另外一方面，對於高黏度之離子液體，我們觀察到四針錐狀氧化鋅奈米結構之光電極相對於一般傳統之光電極結構，也提供了更有效率的離子擴散路徑。而對於四針錐狀氧化鋅奈米結構之光電極這種概念的結構，也適用於其他半導體光電極在 DSC 的未來應用上。

本文的第二部分將使用透過多次電泳沉積無黏結劑之二氧化鈦光電極來填補第一次電泳沉積所產生之裂縫。透過較慢的二次電泳沉積，我們成功地在室溫下製備高品質之二氧化鈦薄膜於 ITO/PEN 塑膠基板上，此元件達到 5.54% 的效率及 0.721 的填充因子。透過交流阻抗分析技術，我們證實了多次電泳沉積所帶來在元件表現上的效益。電子擴散常數在較少裂縫之光電極中增加了約 10 倍。透過散射層的沉積，元件在 AM 1.5 一個模擬太陽光照射下達到的開路電壓、短路電流、填充因子及光電轉換效率分別為 0.763V, 12.06 mA cm<sup>-2</sup>, 0.72 及 6.63%。此外，分別使用兩種有機碘化物(TBAI 和 PMII)的塑膠基板染料敏化電池的實驗結果顯示，含有 TBAI 的 MPN 電解液的塑膠元件比含有 PMII 的表現出較好的長期穩定性。在攝氏 60 度及可見光 1000 小時照射的加速老化測試下，含有 TBAI 的元件維持了 96.9% 的元件效率表現。

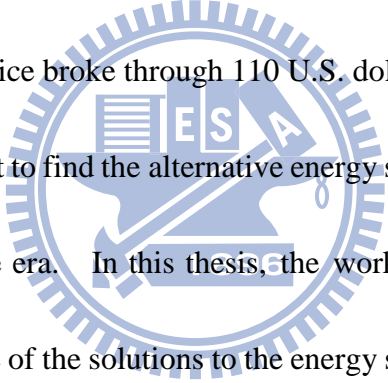
# **Study on Electron Transport Mechanism in Metal Oxide Photoanode Electrode for Dye-Sensitized Solar Cells**

Student: Wei-Hao Chiu

Advisor: Prof. Wen-Feng Hsieh

Institute of Electro-Optical Engineering  
National Chaio Tung University

## **Abstract**



In early 2011, the oil price broke through 110 U.S. dollars per barrel. People are paying more and more effort to find the alternative energy sources that would suffice in the following high-oil-price era. In this thesis, the works are associated with some fundamental research in one of the solutions to the energy sources, dye-sensitized solar cells. The dye-sensitized solar cell is taken as the system where the effects of the structure and the quality of the photoanode electrodes will be studied and rationalized.

Firstly, the tetrapod-like ZnO (T-ZnO) nanoparticles (NPs) are employed to construct an efficient electron transport network as the photoanode of the dye-sensitized solar cells (DSCs). The best performance of DSCs based on 42  $\mu\text{m}$  tetrapod-like ZnO film showed high energy conversion efficiency of 4.9% with high short-circuit current density of  $12.3 \text{ mA cm}^{-2}$ , open-circuit voltage of 0.6 V, and filling

factor of 0.65 under AM 1.5 irradiation. High efficient electron transport may be also ascribed by long effective electron diffusion length of 46  $\mu\text{m}$  determined from the electrochemical impedance spectroscopy (EIS) which is consistent with thickness dependent  $J_{\text{SC}}$  measurement. On the other hand, from time-response photocurrent transient analysis and EIS studies on the ionic diffusion dynamics of the high-viscosity electrolyte, we observed the presence of a tetrapod-like framework as the photoanode provides more efficient ionic diffusion pathway than the conventional photoanode made of C-ZnO (commercial spherical ZnO) nanopowders. And the concept of tetrapod structure is also suitable for other semiconductor photoanode in DSCs for future applications.

In the second part of this thesis, a multiple electrophoretic deposition (EPD) of binder-free  $\text{TiO}_2$  photoanode has been developed to successfully fill the crack occurring after air-drying on the first EPD- $\text{TiO}_2$  film surface. With the slow 2<sup>nd</sup> EPD, high quality  $\text{TiO}_2$  thin films are acquired on flexible ITO/PEN substrates at room temperature and the device efficiency of the dye-sensitized solar cell achieves 5.54% with a high fill factor of 0.721. EIS measurements analyze the great enhancement of the photovoltaic performance through the multiple EPD. The electron diffusion coefficient improved by about 1 order of magnitude in crack-less multiple-EPD  $\text{TiO}_2$  films. With the scattering layer, the device reveals a high conversion efficiency of up to

6.63% under AM 1.5 one sun irradiation, having a short circuit current density, open circuit voltage, and filling factor of  $12.06 \text{ mA cm}^{-2}$ ,  $0.763 \text{ V}$  and  $0.72$ , respectively. Moreover, the durability of dye-sensitized plastic solar cells using two organic iodides (TBAI and PMII) are investigated. Plastic DSCs with MPN-based electrolyte containing TBAI provide good long-term stability than PMII ones. They maintain 96.9 % of baseline efficiency after 100 h under a prolonged visible light irradiation and thermal ( $60 \text{ }^\circ\text{C}$ ) stress aging. We will also report the effects of organic iodides, cell-sealing conditions, and the sheet resistance of indium tin oxide coated polyethylene naphthalate substrate on device durability using the EIS.



# 誌 謝

我常以為，學如逆水行舟，而今輕舟已過萬重山。一路行來，點滴在心，雖然這不是一部完美的論文，但這本論文的完成，要感謝的真人很多，僅以此文表達我的誠摯謝意。

首先衷心的感謝我的指導老師 謝文峰 教授在碩士班兩年以及博士班六年的期間給予的指導與協助。除了在學業上，提供良好的學習環境，對於我們的問題也是不厭其煩的解答，此外在待人處事上，也成為了我的榜樣。

在這八年實驗室的日子中也有許多實驗室的夥伴幫助我很多。阿政學長、維仁學長、志賢學長、黃董、楊松學長也不管在實驗上或是生活上給予許多協助及關心。當然這幾年來也有許許多多的學弟妹一起辛苦的作實驗以及幫忙完成了許多實驗室的雜務以及瑣事。

另外，也要謝謝信民學長帶我進入染料敏化太陽能電池的研究領域，也讓我認識了一群作染敏的高手，使得我的實驗進度可以加快！所以在這也要感謝工研院綠能所的蔡松兩副組長及童永樑博士對我的實驗的強力支持。感謝坤穆、佳樺、明德、孟晉、思萍及曜杉在實驗上給予指導與討論，也謝謝王安、欣怡和竹筠在許多地方上的協助！

最後，也感謝所上的張振雄老師、陳方中老師、盧廷昌老師、台大何國川老師以及中央大學吳春桂老師撥冗參加我的口試，並給我十分寶貴的指導與建議，使得這本論文更加的完善。



當然，還有要在這感謝工研院材化所、綠能所對於我的實驗的支持，以及國科會提拱的實驗經費，讓我的實驗得以順利完成。

最後，我將這篇論文獻給我摯愛的父母。

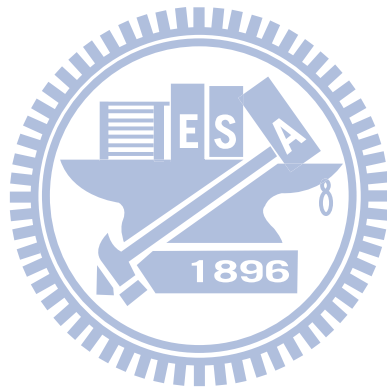


# Table of contents

摘要.....	i
Abstract.....	iii
誌謝.....	vi
Table of contents .....	viii
List of figures.....	x
List of tables.....	xii
Nomenclatures .....	xiii
Chapter 1 Introduction .....	1
1.1 Climate change and energy sources .....	1
1.2 Solar cells – A recent story.....	4
1.3 Objectives of the current work and Organization of dissertation .....	7
Chapter 2 Background .....	9
2.1 Structure, operation, and physical limits of dye-sensitized solar cell.....	9
2.1.1 Sensitizer dyes .....	10
2.1.2 Electrolyte .....	13
2.1.3 Metal oxide photoanode electrode .....	13
2.1.4 Counter electrode.....	17
2.1.5 Charge loss.....	18
2.2 Characterization methods of solar cells .....	19
2.2.1 The solar resource and Air Mass.....	19
2.2.2 IV-measurement .....	21
2.2.3 Incident photon to current conversion efficiency .....	26
2.2.4 Electrochemical impedance spectroscopy and model of the equivalent circuit .....	27
Chapter 3 Experimental setups and procedures .....	32
3.1 Materials .....	32
3.1.1 Commercial materials .....	32
3.1.2 Synthesize tetrapod-like ZnO nanoparticles .....	35
3.1.3 Formation of TiO <sub>2</sub> Nanoscale Materials .....	36
3.2 Preparation of dye-sensitized solar cell .....	36
3.2.1 Photoanode electrode .....	37
3.2.2 Electrolyte .....	40
3.2.3 Counter electrode .....	41
Chapter 4 Towards efficient tetrapod-like ZnO dye-sensitized solar cells .....	50

4.1 Physical properties .....	50
4.2 Sintering effect .....	55
4.3 Optimization of photoanode electrode thickness .....	56
4.4 Efficient electron transporting in tetrapod-like ZnO photoanode .....	60
4-5 Influence of photoanode thickness on the photovoltaic performance of ionic liquid device .....	62
4.5 Ionic diffusion dynamics of ionic-liquid electrolyte .....	67
4.6 Summary .....	73
Chapter 5 Multiple electrophoresis deposited crackless TiO <sub>2</sub> photoanode for flexible DSCs .....	75
5.1 Compress effect on photovoltaic performances .....	75
5.2 Photovoltaic characteristic of multiple electrophoresis deposition .....	79
5.3 Effect of light scattering layer .....	86
5.4 Long-term stability testing .....	89
5.5 Summary .....	95
Chapter 6 Conclusions and Perspectives .....	97
6.1 Conclusion .....	97
6.2 Perspectives .....	99
Reference .....	100
Curriculum Vitae .....	105



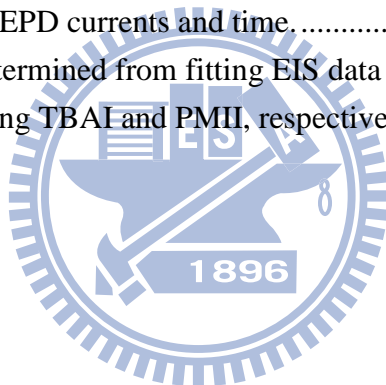
# List of figures

Fig. 1-1. World marketed energy used by fuel types, 1990-2035 .....	2
Fig. 1-2. Thirty years evolution in conversion efficiencies of different photovoltaic technologies. ....	4
Fig. 2-1. Structure and operation principle of dye-sensitized solar cell . ....	11
Fig. 2-2. The common TiO <sub>2</sub> crystal structures .....	14
Fig. 2-3. ZnO wurtzite structure. ....	16
Fig. 2-4. Solar irradiance spectrum above the atmosphere and at the surface. ....	19
Fig. 2-5. Photovoltaic performance of a laboratory N-719-sensitized P-90 TiO <sub>2</sub> solar cell .....	23
Fig. 2-6. The effect of shunt and series resistances on PV performance through computing simulation.....	25
Fig. 2-7. Typical Nyquist and Bode plots of impedance spectra for a DSC. ....	28
Fig. 3-1 . Schematic of the DC plasma reactor. ....	35
Fig. 3-2. Configuration of the dye sensitized solar cells.....	37
Fig. 3-3. Heating curve for ZnO photoanode electrode. ....	38
Fig. 3-4. Sketch schemes of the electrophoretic cell, the preparation of TiO <sub>2</sub> electrodes, and the significant parameters in EPD process.....	39
Fig. 3-5. The transmittance spectra of the substrates used in this study. ....	43
Fig. 3-6. The uniformity of the white light source.....	45
Fig. 3-7. The standard AM 1.5 spectrum compared with the spectrums from the white light source .....	46
Fig. 3-8. The output variation of the white light source. ....	46
Fig. 3-9. Emission spectrum of the white LED array. ....	47
Fig. 3-10. Measured spectral transmittance for ND filters used in this study. ....	48
Fig. 4-1. FESEM and FETEM images of the tetrapod-like ZnO NPs .....	51
Fig. 4-2. XRD patterns of the tetrapod-like ZnO NPs. ....	52
Fig. 4-3. SEM image of T-ZnO and C-ZnO film on FTO/glass .....	53
Fig. 4-4. Optical properties of D149. ....	55
Fig. 4-5. Thickness dependent photovoltaic characteristics of the T-ZnO DSCs with D149 dye.....	57
Fig. 4-6. J-V curve and IPCE spectra obtained with DSSCs based on D149 and CDCA absorption.....	60
Fig. 4-7. Nyquist plot of tetrapod-like ZnO DSCs sensitized by Di49 dye.....	61
Fig. 4-8. Dependences of AN-based and IL-based cell performances on film thickness.....	63
Fig. 4-9. Cell performances of AN-based and IL-based DSCs based on C-ZnO and	

T-ZnO photoanodes.....	66
Fig. 4-10. The photocurrent transient dynamics of IL-based D149-sensitized solar cells .....	68
Fig. 4-11. The EIS characteristics of the IL-based D149-sensitized solar cells .....	70
Fig. 5-1. The correlation between the compression pressure of the electrophoretic deposited TiO <sub>2</sub> thin film and device performance. ....	77
Fig. 5-2. The correlation between the compression time of the electrophoretic deposited TiO <sub>2</sub> film and the current density and conversion efficiency. ....	78
Fig. 5-3. The microscopy pictures of electrophoretically deposited P-90 TiO <sub>2</sub> film on ITO/PEN film.....	79
Fig. 5-4. The effect of different 2 <sup>nd</sup> EPD TiO <sub>2</sub> photoanode on J-V curve of DSC ..	82
Fig. 5-5. The Nyquist plots of DSC device with the different 2 <sup>nd</sup> EPD TiO <sub>2</sub> photoanode. ....	84
Fig. 5-6. Cross-section SEM image of an EPD film for 100 nm TiO <sub>2</sub> and P90 TiO <sub>2</sub> and its IPCE spectra. ....	87
Fig. 5-7. PV characteristics of nanocrystalline TiO <sub>2</sub> DSCs with TiO <sub>2</sub> photoanode deposited multiply by P-90 and 100nm NPs.....	89
Fig. 5-8. The relationship between the sheet resistance of ITO/PEN and the immersion time in electrolyte at 60 °C .....	90
Fig. 5-9. Photovoltaic parameters for plastic DSC with TBAI or PMII after visible light soaking (1 sun) at 60 °C.....	92
Fig. 5-10. EIS results of plastic DSCs with different iodides under one sun light soaking .....	93

# List of tables

Table 1-1. Current use and current potentials of selected renewable energy sources. .....	2
Table 3-1. The compositions of the electrolytes used in different chapter of this thesis. .....	40
Table 3-2. Class AAA Standards and Specifications .....	47
Table 4-1. Cell performance of the DSC with hierarchical 20 $\mu\text{m}$ T-ZnO photoanode electrode sintered at different temperature.....	56
Table 4-2. Photovoltaic performance of IL-based DSCs and corresponding properties of photoanode determined by electrochemical impedance spectroscopy under full sunlight irradiation. ....	72
Table 5-1. Dye-sensitized solar cell performances with one-step or two-step EPD preparation methods.....	80
Table 5-2. Dye-sensitized solar cell performances with two-steps EPD preparation methods by various EPD currents and time.....	81
Table 5-3. Parameters determined from fitting EIS data of plastic DSC with electrolytes containing TBAI and PMII, respectively. ....	94



# Nomenclatures

## Abbreviations

AM	Air mass
AN	Acetonitrile (C <sub>2</sub> H <sub>3</sub> N)
BET	Brunauer-Emmett-Teller
BTU	British thermal unit, equal to about 1,055.05585 joules
C-ZnO	Commercial ZnO
CB	Conduction band
CDCA	Chenodeoxycholic acid
CE	Counter electrode
GIGS	Copper indium gallium (di)selenide (CuIn <sub>x</sub> Ga <sub>(1-x)</sub> Se <sub>2</sub> )
CPE	Constant phase element
DC	Direct Current
DSC	Dye-sensitized solar cell
EC	Ethyl cellulose
EIS	Electrochemical impedance spectroscopy
EMAA	Ethylene-co-methacrylic acid
EL	Electrolyte
EPD	Electrophoretic deposition
FESEM	Field emission scanning electron microscopy
FETEM	Field emission transmission electron microscopy
FF	Filling factor
FTO	Fluorine-doped tin oxide (SnO <sub>2</sub> :F)
HOMO	Highest occupied molecular orbital
HPLC	High-performance liquid chromatography
HTM	Hole transport material
ICT	Intramolecular charge transfer
IL	Ionic liquid
IPA	Isopropyl alcohol
IPCE	Incident photon-to-electron conversion efficiency
ITO	Indium tin oxide (tin-doped indium oxide)
JCPDS	Joint committee on powder diffraction standards
LUMO	Lowest unoccupied molecular orbital
MLCT	Metal-to-ligand charge transfer
MO	Metal oxide
MPN	3-methoxypropionitrile

NP	Nanoparticle
NW	Nanowire
OC	Open circuit
PE	Photoanode electrode
PEN	Polyethylene naphthalate
PMII	1-methyl-3-propyl imidazolium iodide
PV	Photovoltaic
Redox	Reduction-oxidation
RT	Room temperature
SC	Short circuit
t-BuOH	tert-butyl alcohol
T-ZnO	Tetrapod-like ZnO
TBAI	Tetrabutylammonium iodide
TBP	4-tert-butylpyridine
TCO	Transparent conducting oxide
UV	Ultraviolet
V	Voltage
VB	Valence band
VIS	Visible
XRD	X-ray diffraction



## English Symbols

A	Photoanode electrode area	cm <sup>2</sup>
A <sub>v</sub>	Avogadro's constant = 6.02 × 10 <sup>23</sup>	mol <sup>-1</sup>
C*	Concentration of tri-iodide in the bulk electrolyte	mol cm <sup>-3</sup>
C <sub>μ</sub>	Chemical capacitance of the photoanode	μF/cm <sup>-2</sup>
C <sub>Pt</sub>	CPE at the Pt surface	μF/cm <sup>-2</sup>
C <sub>TCO1</sub>	CPE at the photoanode and its substrate interface	μF/cm <sup>-2</sup>
C <sub>TCO2</sub>	CPE at the photoanode substrate and electrolyte interface	μF/cm <sup>-2</sup>
c <sub>m</sub>	Velocity of light in the medium	m s <sup>-1</sup>
d	Nernst diffusion layer thickness	μm
D <sub>eff</sub>	Effective electron diffusion coefficient in photoanode	cm <sup>2</sup> s <sup>-1</sup>
D	Diffusion coefficient of tri-iodide in electrolyte	cm <sup>2</sup> s <sup>-1</sup>
E <sub>g</sub>	Energy gap	eV
h	Planck constant = 6.626068 × 10 <sup>-34</sup> m <sup>2</sup> kg s <sup>-1</sup>	m <sup>2</sup> kg s <sup>-1</sup>
[I <sub>2</sub> ]	Concentration of iodine	mol cm <sup>-3</sup>

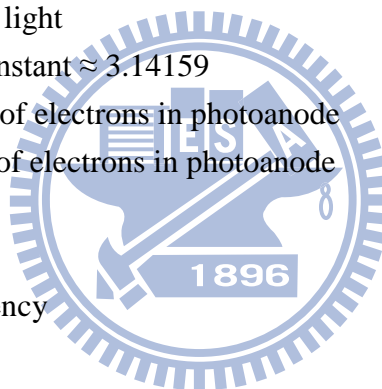


$[I_3^-]$	Concentration of tri-iodide	$\text{mol cm}^{-3}$
$I_{\text{dark}}$	Dark current of the diode	A
$I_{\text{SC}}$	Short-circuit current	A
$I_{\text{S}}$	Saturation current of the diode (typically $10^{-7}$ to $10^{-9}$ A)	A
$I_{\text{ph}}$	Photocurrent that depends on irradiation intensity	A
$I_{\text{inj}}$	Flux of charge from sensitized dyes inject to photoanode	$\text{C m}^{-2} \text{ s}^{-1}$
$J_{\text{SC}}$	Short-circuit current density	$\text{mA cm}^{-2}$
$k_{\text{B}}$	Boltzmann's constant = $1.38 \times 10^{-23}$	$\text{J K}^{-1}$
$k_{\text{eff}}$	Effective rate constant for recombination in photoanode	$\text{s}^{-1}$
$k_{\text{et}}$	Reaction rate constant of the dark current from ZnO to tri-iodide ions in the electrolyte	$\text{s}^{-1}$
$L$	Thickness of the photoanode film	$\mu\text{m}$
$L_{\text{n}}$	Electron diffusion length in the photoanode film	$\mu\text{m}$
$n_{\text{cb}}$	Electron concentration in the conduction band of the photoanode	$\text{cm}^{-3}$
$P$	Compression pressure	MPa
$P_{\text{in}}$	The incident light power usually equal to $100 \text{ mW cm}^{-2}$ under the irradiance of AM1.5 spectrum	$\text{mW cm}^{-2}$
$P_{\text{out}}$	Total output power of the solar cell	$\text{mW cm}^{-2}$
$q$	Elementary charge = $1.6 \times 10^{-19}$	C
$R_{\text{D}}$	DC resistance of diffusion of tri-iodide in the electrolyte	$\Omega$
$R_{\text{k}}$	$r_{\text{W}}/L$	$\Omega$
$R_{\text{Pt}}$	Resistance at the Pt surface	$\Omega \text{ cm}^2$
$R_{\text{S}}$	Transport resistance of substrate and external circuits	$\Omega$
$R_{\text{ser}}$	The series shunt resistance of a solar cell	$\Omega$
$R_{\text{sh}}$	The shunt resistance of a solar cell	$\Omega$
$R_{\text{TCO1}}$	Resistance at the photoanode and its substrate interface	$\Omega \text{ cm}^2$
$R_{\text{TCO2}}$	Resistance at the photoanode substrate and electrolyte interface	$\Omega \text{ cm}^2$
$R_{\text{W}}$	$r_{\text{W}} \times L$	$\Omega$
$r_{\text{k}}$	Charge-transfer resistance related to recombination of electron at the photoanode and electrolyte interface	$\Omega \text{ cm}$
$r_{\text{W}}$	Electron transport resistance in photoanode	$\Omega/\text{cm}$
$S$	Ground state of dye	—
$S^+$	Oxidized dye	—
$S^*$	Excited state of dye	—
$T$	Absolute temperature	K
$V_{\text{T}}$	Thermal voltage that equals $k_{\text{B}}T/q$	V
$V_{\text{OC}}$	Open circuit voltage	V
$Z$	Impedance of the cell	$\Omega$

$Z_N$	Finite Warburg impedance of the electrolyte	$\Omega$
$Z_{PE}$	Impedance of the photoanode electrode	$\Omega$
$Z_{Pt}$	Impedance of the Pt electrode	$\Omega$
$Z_{TCO1}$	Impedance of the photoanode and its substrate interface	$\Omega$
$Z_{TCO2}$	Impedance of the photoanode substrate and electrolyte interface	$\Omega$
$Z'$	Real part of impedance of the cell	$\Omega$
$Z''$	Imaginary part of impedance of the cell	$\Omega$

## Greek Symbols

$\eta$	Energy conversion efficiency of the solar cell	%
$\eta_{COL}$	The electron collection efficiency of the solar cell	%
$\eta_{ING}$	The electron injection efficiency of the solar cell	%
$\eta_{LH}$	The light harvesting efficiency of the solar cell	%
$\lambda$	Wavelength of the light	nm
$\pi$	Transcendental constant $\approx 3.14159$	—
$\tau_d$	Transporting time of electrons in photoanode	s
$\tau_{eff}$	Effective lifetime of electrons in photoanode	s
$\Phi$	The photon flux	$s^{-1}$
$\Omega$	Solid angle	sr
$\omega$	Modulation frequency	$s^{-1}$



# Chapter 1 Introduction

## 1.1 Climate change and energy sources

From the historical period of global industrialization to the present, the energy consumption was growth explosively. U.S. Energy Information Administration predicted in 2005 that the annual world primary energy consumption would increase 49% from 2007 to 2035. Total world energy use rises from 495 quadrillion British thermal units (BTU) in 2007 to 590 quadrillion BTU in 2020 and 739 quadrillion BTU in 2035 [1]. Presently, the energy economy is still highly dependent on three forms of fossil fuels- oil, natural gases and coal with high percentages (see Fig. 1-1). The fossil fuels have contributed to the increase in carbon dioxide (CO<sub>2</sub>) in the atmosphere from 313 ppm in 1960 to about 390 ppm in 2010. The greenhouse effect of combustion-produced carbon dioxide has been become seriously. Until now, people have seen mild effects from global warming caused by the greenhouse effect. The global warming not only melts the ice volume at South Pole led to several meters of sea level rise but also changes the climate to affect the agriculture (food production).

In addition to the fossil fuels, nuclear power is one of the carbon-free energy resources. But notably from the Three Mile Island nuclear accident (1979),

Chernobyl nuclear disaster (1986) and Fukushima nuclear accidents (2011), people learned that the nuclear power isn't 100% safe to operate. So people pay more attention to find clean and safe renewable energy to replace the fossil fuel and nuclear power.

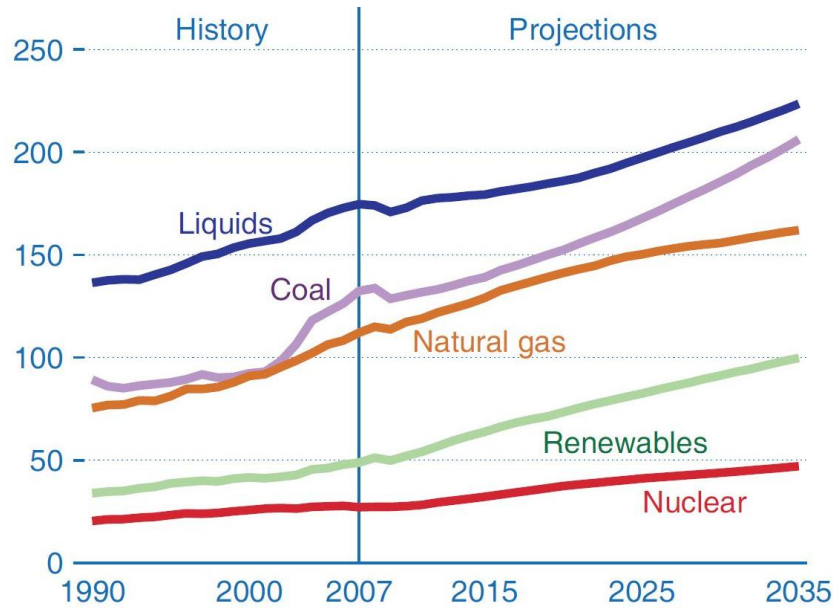


Fig. 1-1. World marketed energy used by fuel types, 1990-2035 (quadrillion BTU) [1]

Table 1-1. Current uses and current potentials of selected renewable energy sources. [2]

Resource	Current use (in 2000)	Technical potential (exajoule/yr)	Theoretical potential (exajoule/yr)
Hydropower	9	50	147
Biomass energy	50	>276	2900
Solar energy	0.1	>1575	3900000
Wind energy	0.12	640	6000

On the other hands, oil might run out in around 40 years at current reserves-to-production (R/P) ratio with a daily consumption of 82.5 million barrels.

A better synopsis is for natural gases that can last for about 60 years and coal, being

the most abundant, for 150 years. [1] Much interesting in renewable energy sources appeared in the wake of the oil crisis in 1970s. Table 1.1 lists the potential of the selected renewable energy sources. Solar power has great potential with more than thousand times comparing to other renewable energy sources, but in 2000 supplied less than 0.1% of the world's total energy supply. As we know, sun is just like a forever-burning fire due to its lifetime (about  $15 \times 10^6$  years) comparing to human's life (100 years). The earth receives about  $10^5$  TW of solar power at its surface. The sun is a free and unlimited energy source. This is a huge energy source that means harvesting the total solar energy for one hour would supply the energy need of the humanity for one year. Many solar photovoltaic power stations with  $< 100$  MW peak power have been built, mainly in Europe. Nowadays, several large photovoltaic electric plants are under planning to construct. Ordos Solar Project in China plans to build a CdTe thin film solar plant with DC peak power of 2 gigawatts (GW) and is scheduled completion date 2019. Planned installations in USA (Topaz Solar Farm, Desert Stateline, Aqua Caliente Solar Project, California Valley Solar Ranch, etc.) will produce about 200 to 500 MW at peak and will be completed between 2013 and 2015. [3]

## 1.2 Solar cells – A recent story

A solar cell can be described as a device that is able to transform the photon energy to electric energy in form of current and voltage. The photovoltaic effect was first recognized by a French physicist A. E. Becquerel in 1839, [4] but the first photovoltaic cell with around 1% efficiency was built by Charles Fritts until 1883. The modern photovoltaic (PV) cell by using a diffused silicon p-n junction was developed at Bell Laboratories in 1954. [5] The cell produced 1 watt of electric power in bright sunlight cost about USD\$ 250, comparing to USD\$ 3 for a coal plant. After taking several improvements, Dr. Berman's team at Solar Power Corporation cut the cost of single crystal Si PV down to USD\$ 10 – 20 per watt in the 1970s. Afterward, people pay considerable attention to boost the cell efficiency and to reduce the fabrication cost.

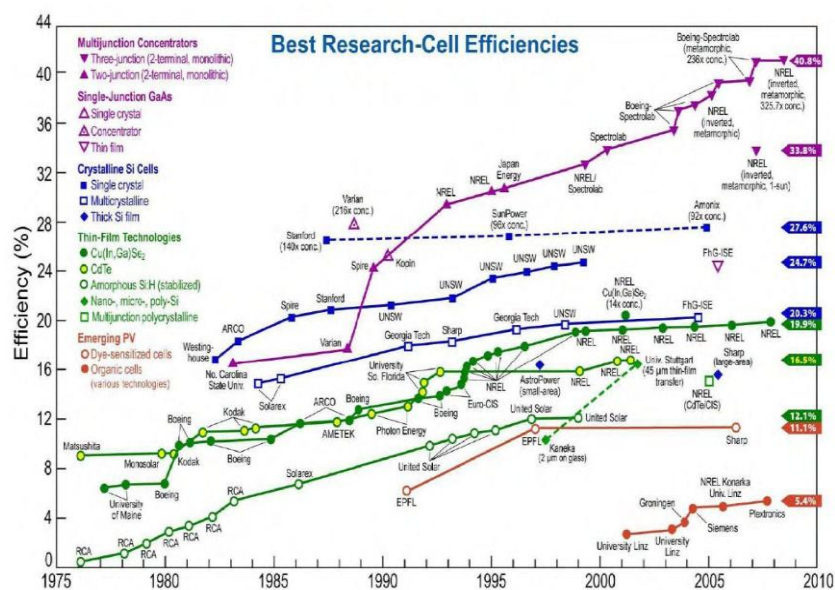


Fig. 1-2. Thirty years evolution in conversion efficiencies of different photovoltaic technologies. (NREL via Solid State Technology)

In parallel, Audubert and Stora discovered the photovoltaic effect in cadmium sulfide (CdS) in 1932, opening up the way of II-VI thin film solar cells. [6] In the following years, *p-n* junctions with CdS and CdTe were studied for a higher efficiency. Wu X. et al. have achieved a CdTe polycrystalline thin-film solar cell demonstrating total-area efficiency of 10.9% in 2000 which was confirmed by the National Renewable Energy Laboratory (NREL). [7] For III-V solar cells, a 1 cm<sup>2</sup> thin-film GaAs device with efficiency of 27.6% has been measured at NREL fabricated by Alta Devices, Inc. [8] A high efficiency of 42.3% has been obtained for the triple junction solar cells consist of indium gallium arsenide (InGaAs, 0.94 eV), gallium arsenide (GaAs, 1.42 eV) and indium gallium phosphide (InGaP, 1.89 eV) under 406 suns concentrated illuminations. [9] Copper indium gallium diselenide (CIGS ; formula :  $\text{CuIn}_x\text{Ga}_{(1-x)}\text{Se}_2$ ) is a direct-bandgap material for thin film PV application, and its bandgap varies continuously with x from about 1.0 eV (for copper indium selenide) to about 1.7 eV (for copper gallium selenide). A team at the NREL achieved 19.9% new world record efficiency in 2008. [8] However, the materials used in these PV technologies include rare elements, such as indium (Crustal abundance = 0.16 ppm ), selenium (0.05 ppm), cadmium (0.15 ppm), and tellurium (0.001 ppm) [10] , could be a restriction if PV became the main energy supplier.

A dye-sensitized solar cell (DSC) is a relatively new class of thin film solar cell. It

had a breakthrough in the early 1990s in École Polytechnique Fédérale de Lausanne (EPFL), Swiss by Prof. Michael Grätzel and Brian O'Regan. With the discovery of the Ru-based N3 dye and the later panchromatic “black dye”, the electrical conversion efficiency was pushed well over 10%. [11, 12] This cell is extremely promising because it is made of low-cost raw materials, such as TiO<sub>2</sub> (Ti of crustal abundance = 6600 ppm [10]) or ZnO (Zn : 79 ppm), and does not need elaborate apparatus to manufacture. Although the Ru-complex dye was widely used in DSC due to its outstanding photovoltaic properties, the Ru element is a rare transition metal belonging to the platinum group of the periodic table and its crustal abundance is only 0.001 ppm. Scientists work on other kind of dye to avoid the lack of Ru element. Several research groups in the world, e.g., Prof. Michael Grätzel in Swiss [13], Prof. Eric Wei-Guang Diau in Taiwan [14], have experimented with a wide variety of Zn-porphyrin dye and reported the efficiency of about 5%. Metal-free organic dyes, such as D149 [15], have also been considerably researched in recent years to replace Ru-dye. [16] Due to several kinds of dyes with different absorption wavelength ranges, DSC is capable of having colorful designs for building-integrated photovoltaic (BIPV) applications.

In 2008, Prof. Grätzel demonstrated 8.2% efficiency DSC consisting of a new solvent-free liquid redox electrolyte, and the device retained over 93% of its initial

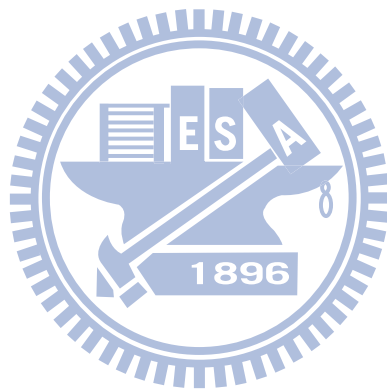


conversion efficiency under the irradiance of AM 1.5G sunlight during successive full-sun visible-light soaking at 60 °C. Recent achievements of long-time stability under accelerated experiments with non-volatile liquid (e.g., MPN) and ionic liquid electrolyte greatly promote the practical application of this low-cost PV and put it currently right at the start of commercialization stage.

### **1.3 Objectives of the current work and organization of dissertation**

The thesis is then subdivided into mainly six parts: Chapter 2 gives a brief background of DSC including the structures, the working principles, and the related mechanisms. Chapter 3 addresses all the experimental processes of device fabrication and characterization techniques. Chapters 4 and 5 discussed this dissertation research. It will be focused on realizing the effects of the structure and the quality of the photoanode electrodes. In Chapter 4, a hierarchical structure of photoanode electrode (PE) made by tetrapod-like ZnO (T-ZnO) was demonstrated. And its electron dynamics in PE and ionic diffusion mechanism in ionic liquid (IL) film will be discussed. Chapter 5 provides a method to resolve the crack issue of low-temperature flexible DSC. And its long-term stability properties are also tested and discussed. A chapter of general conclusions is then made on the basis of all

previous chapters and the direction of future to DSC is also given in Chapter 6.



# Chapter 2 Background

In this chapter, the structure, the operation and the physical limits of dye-sensitized solar cell (DSC) will be described first. And then the characterization methods of DSC, which were used in this study, will be introduced.

## 2.1 Structure, operation, and physical limits of dye-sensitized solar cells

Figure 2-1 shows a schematic representation of the operating principle of DSC including the dye sensitizer, the metal oxide photoanode electrode (PE), the electrolyte, and the counter electrode (CE).

The operation of DSC represents an interesting convergence of photography and photoelectrochemistry, both of which rely on photoinduced charge dynamic at a liquid–solid interface and in pure bulk medium (liquid or solid). These dynamics are listed below and will be discussed in the following:

(I) Dye sensitizers adsorbed on the metal oxide (MO) surface absorb incident photon flux. The dyes are excited from the ground state (S) to the excited state (S\*) *via* the metal to ligand charge transfer (MLCT) transition.



(II) The excited electrons are injected into the conduction band (CB) of the MO, resulting in the oxidation of the dye.



(III) The injected electrons transported between MO nanoparticles (NPs) with diffusion toward the back contact TCO.

(IV) The oxidized dye ( $S^+$ ) accepts electrons from the  $I^-$  ion redox mediator, regenerating the ground state (S), and  $I^-$  is oxidized to the oxidized state,  $I_3^-$ .



(V) Catalyze the redox couple *viz.*  $I^-/I_3^-$  regeneration reaction at counter electrode.



(VI) Interfacial charge recombination



(VII) Back-reaction electron recombination



### 2.1.1 Sensitizer dyes

The current obtained from a DSC is determined by the energy difference between the HOMO and the LUMO of the dye, which is just like the energy bandgap ( $E_g$ ) for inorganic semiconductor materials. Due to the utilization of the long-wavelength region in the solar spectrum, the smaller the HOMO–LUMO energy gap, the larger the current will be obtained.

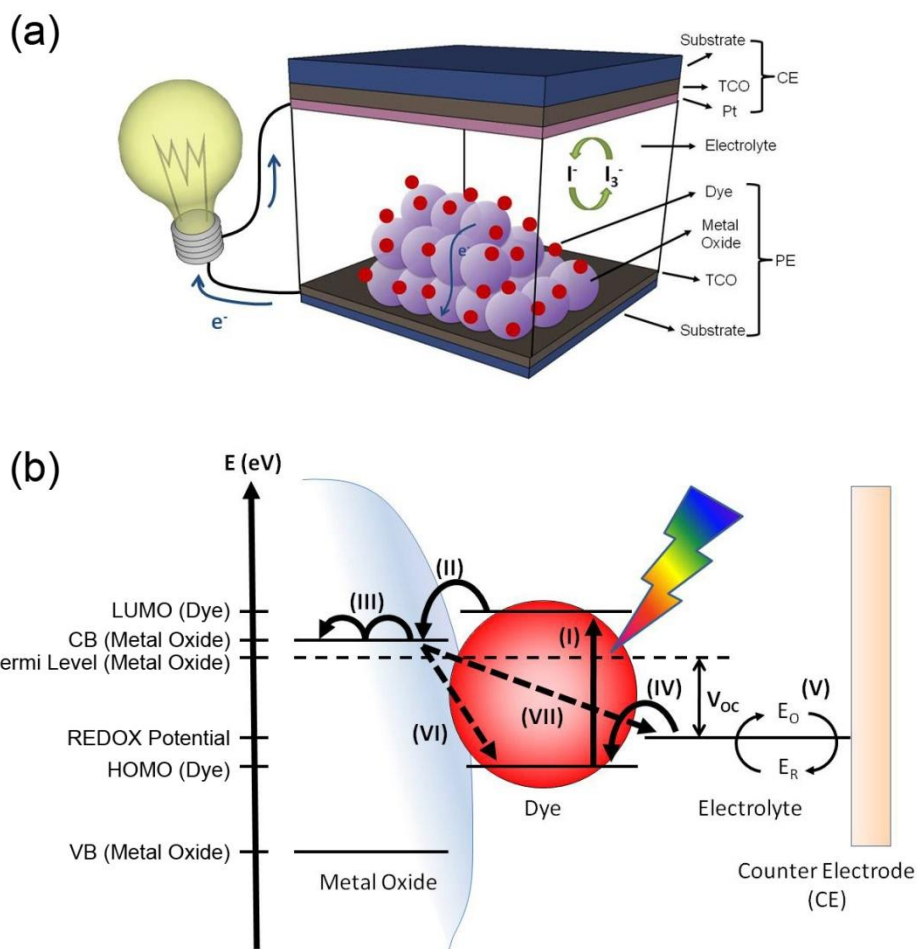


Fig. 2-1. (a) Structure and (b) operation principle of dye-sensitized solar cell (DSC).

Charge separation in the DSC is achieved by photoinduced electron injection ( $\sim$ fs) from the dye molecular excited state of the sensitizer to semiconductor nanoparticles (NPs). For example, for efficient dye molecular, such as Ru-complex dye N719, absorbed on nanocrystalline TiO<sub>2</sub> film, these complexes undergo strong MLCT under visible irradiation and the injecting molecular orbital is the  $\pi^*$  wave function of the carboxylated bipyridyl ligand. The interaction between carboxylate groups with the surface Ti(IV) ions results in good electronic coupling of the  $\pi^*$  wave function with

the 3d orbital manifold of the conduction band of the TiO<sub>2</sub>, leading to very rapid injection dynamics. [17]

The energy level of the LUMO must be sufficiently negative with respect to the CB of MO ( $\Delta E_1$ ) to inject electrons effectively. On the other hand, The HOMO level of the sensitizer must be sufficiently more positive than the redox potential ( $\Delta E_2$ ) of the electrolyte (commonly is I<sup>-</sup>/I<sub>3</sub><sup>-</sup>) to accept electrons effectively and to regenerate excited dye in order to re-absorb photon. And it is reported that the energy gaps ( $\Delta E_1$  and  $\Delta E_2$ ) should be larger than approximately 200 meV to give a suitable driving force for each of the electron-transfer reactions.

Fast dye regeneration is a prerequisite for an efficient DSC due to fast re-absorption of light. In the pure solvent system, the lifetime of dye cation can be as long as milliseconds. [18] However, dye cation quenching of down to microseconds has been observed by introducing redox couples that the most widely used I<sup>-</sup>/I<sub>3</sub><sup>-</sup>. Dye regeneration is faster with increasing I<sup>-</sup> concentrations. On the contrary, dye regeneration in DSCs with solid-state hole conductor system or high viscosity ionic liquid system has not been thoroughly studied and demands further pertinent work.

### ***2.1.2 Electrolyte***

The electrolyte plays the important role of regenerating dye-cations, see Eq. 2-3 with characteristic time  $\sim \mu\text{s}$ , produced by the injection ( $\sim\text{fs}$ ) of electrons from photo-excited dyes to metal oxide (MO) and transporting the positive charge to the counter electrode (CE). Nowadays,  $\text{I}^-/\text{I}_3^-$  redox system is still the best electrolyte for DSCs. Efficiencies of more than 11% with AN-based electrolyte [19] and 8% long-term stability at 80 °C with a low volatile electrolyte [20], such as MPN-based system, have been achieved. The liquid electrolyte has some potential problems, such as the leakage and volatilization of solvents, possible desorption and photodegradation of the attached dyes, and the corrosion of Pt counterelectrode that limits the long-term performance and practical use of DSCs [18, 21, 22]. The room temperature ionic liquids (ILs) have attracted considerable interests as a potential candidate for replacing the volatile organic solvents due to their negligible vapor pressure, stable chemical properties, and high ionic conductivity. Therefore, researchers pay much attention to improve the performance of DSC with IL electrolytes.

### ***2.1.3 Metal oxide photoanode electrode***

The porous metal oxide (MO) photoanode electrode (PE) essentially serves the

purposes of collecting and transporting ( $\sim$  ms) photoinduced electrons injected ( $\sim$ fs) from the photoexcited dye via MO conduction band to the TCO substrate then to the external circuit. High porosity and suitable pore sizes of the porous MO layer increase the dye adsorption capacity and light harvesting ability. The recombination reactions also occur at the surface of PE that will be discussed at the end of this section. Typically, two kinds of semiconductors,  $\text{TiO}_2$  and  $\text{ZnO}$ , are commonly used in DSC and will be discussed later.

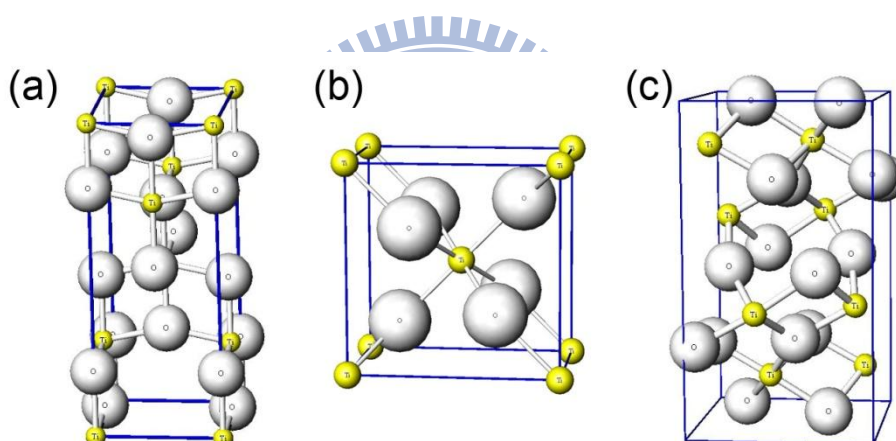


Fig. 2-2. The common  $\text{TiO}_2$  crystal structures : (a) Anatase structure with space group  $I4_1/amd$  or Pearson symbol  $tI12$ . (b) Rutile structure or  $C4$  type structure with space group  $P4_2/mnm$  Or Pearson symbol  $tP6$ . (c) Brookite structure or  $C21$  type structure with space group  $Pbca$  or Pearson symbol  $oP24$ .

Titanium dioxide ( $\text{TiO}_2$ ), also known as titanium(IV) oxide or titania, has two crystalline forms that are anatase and rutile, shown in Fig. 2-2. Anatase appears as pyramid-like crystal and is stable at low temperature, whereas needle-like rutile crystal is dominantly formed at high temperature process. Single crystal of  $\text{TiO}_2$  also has



rutile structure. The densities are  $3.89 \text{ g cm}^{-3}$  and  $4.26 \text{ g cm}^{-3}$  for anatase and rutile respectively. Rutile absorbs ca. 4% of the incoming light in the near-UV region, and band gap excitation generates holes that act as strong oxidants reducing the long-term stability of the dye-sensitized solar cells. The third crystalline form of  $\text{TiO}_2$ , brookite, is difficult to produce and is therefore not of practical interest for DSC. The band-gaps of the crystalline forms are 3.2 eV (the absorption edge at 388 nm) for anatase and 3.0 eV (the absorption edge at 413 nm) for rutile. However, DSC with pure rutile  $\text{TiO}_2$  PE exhibited only 30% smaller short circuit current ( $I_{\text{SC}}$ ) than that with pure anatase  $\text{TiO}_2$  PE, and had the same open circuit voltage ( $V_{\text{OC}}$ ). [23] In addition to the good chemical stability of nontoxic and inexpensive  $\text{TiO}_2$ , anatase  $\text{TiO}_2$  has been the most popular material of study in DSCs compared to other metal oxide material until now.

Zinc oxide is an inorganic compound with the formula  $\text{ZnO}$ . It usually appears as a white powder, nearly insoluble in water. Zinc oxide crystallizes in three forms: hexagonal wurtzite, cubic zinc blende, and the rarely observed cubic rocksalt. The hexagonal wurtzite structure shown in Fig. 2-3 is the most stable at ambient conditions and thus the most common. The hexagonal wurtzite structure has a point group  $6 \text{ mm}$  in Hermann-Mauguin notation or  $C_{6v}$  in Schoenflies notation, and the space group is  $P6_3mc$  or  $C_{6v}^4$ . The lattice constants are  $a = 3.25 \text{ \AA}$  and  $c = 5.2 \text{ \AA}$ ; their

ratio  $c/a \sim 1.60$  is close to the ideal value for hexagonal cell  $c/a = 1.633$ .

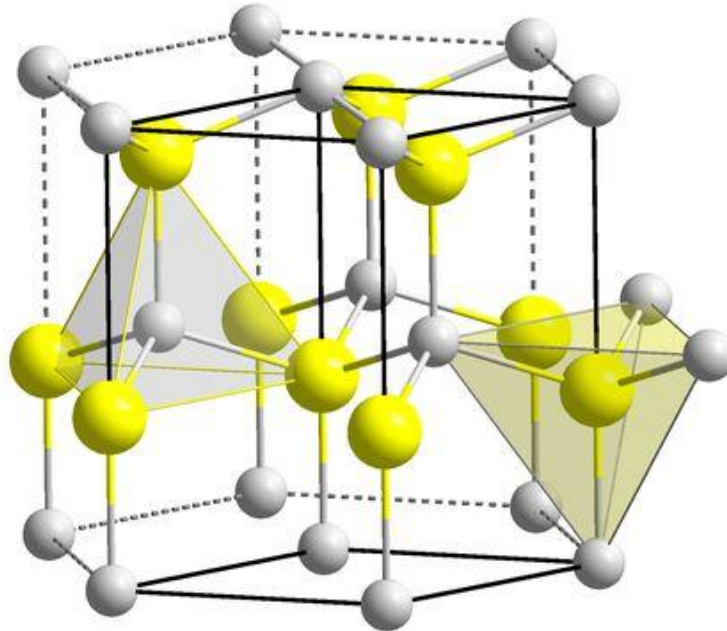


Fig. 2-3. ZnO wurtzite structure, also called *B4* type structure. Space group is  $P6_3mc$ . Pearson symbol is  $hP4$ . Wurtzite is hexagonal stacking of ZnO.

The versatile ZnO is a wide-bandgap (3.37 eV) semiconductor of the II-VI semiconductor group, which is similar to  $\text{TiO}_2$  of 3.2eV. The native doping of ZnO (due to oxygen vacancies) is n-type. This semiconductor has several favorable properties: good transparency, high electron mobility (about  $155 \text{ cm}^2\text{V}^{-1}\text{s}^{-1}$  for high quality thin film [24]), wide bandgap, strong room-temperature luminescence, etc. Those properties are already used in emerging applications for transparent electrodes, heat-protecting windows, electronic applications, acoustic devices or solar energy devices. [25-29] ZnO also can be tailored to various nanostructures (such as

nanowire [30, 31], nanosheet [32-34], nanodendrite [35, 36], popcorn [37, 38], tetrapod [39-41], etc.) as compared to TiO<sub>2</sub>, which provides a promising means for improving the performance of the photoelectrode in DSCs. [42]

#### **2.1.4 Counter electrode**

Tri-iodide ions, I<sub>3</sub><sup>-</sup>, formed by the reduction of dye cations with I<sup>-</sup> ion, are re-reduced to I<sup>-</sup> ions at the counter electrode (CE). To reduce the tri-iodide ions, the counter electrode must have high electrocatalytic activity. Pt-coated (5–10 μg cm<sup>-2</sup>) on TCO substrates are usually used as the CE. Pt-free counter electrodes for the DSC include carbonaceous materials such as graphite [43, 44], carbon black [45, 46], carbon nanotubes [47, 48], activated carbon [49], and organic ion-doped conducting polymers of poly(3,4-ethylenedioxythiophene) (PEDOT) [50, 51] on both indium tin oxide (ITO) and FTO-glass. The electrocatalytic activity of CE directly affects the fill factor of the device. A desirable exchange current density corresponding to the electrocatalytic activity for the reduction of I<sub>3</sub><sup>-</sup> ions is 10 to 200 mA cm<sup>-2</sup>. [52, 53] The obtained counter electrode was optically transparent and of highly dispersed platinum particles for catalyzing I<sup>-</sup>/I<sub>3</sub><sup>-</sup> redox reaction.

### 2.1.5 Charge loss

Due to the relatively small electron diffusion coefficient  $D_{\text{eff}}$  ( $\sim 10^{-5} \text{ cm}^2\text{s}^{-1}$  for  $\text{TiO}_2$ ) and slow electron diffusion process ( $\sim \text{ms}$  for  $\text{TiO}_2$ ), electrons in  $\text{TiO}_2$  porous film may recombine with dye cation  $S^+$ , see Eq. (2-5) with  $\sim \text{ms}$ , and/or the oxidized form of the redox couple in the electrolyte [Eq. (2-6),  $\sim \text{ms}$ ], typically  $\text{I}_3^-$ . These two interactions of molecular species with the surface of metal oxide can affect the solar cell performance in two principal ways. First, they can alter the recombination kinetics of photo-excited electrons with  $\text{I}_3^-$  by passivating the metal oxide. Second, they can charge the surface (either positively or negatively), which will lead to movement of the metal oxide conduction band with respect to the electrochemical potential of the redox couple. Both effects will change  $V_{\text{oc}}$  of the cell and affect the recombination, as has been shown for pyridine and ammonia. [54, 55]

The transfer of electrons from TCO to the triiodine ions in solution (charge recombination) results in another important loss (back-reaction) in DSCs. The charge recombination can be significantly mitigated by using thin compact blocking layers of  $\text{TiO}_2$  [56] or other blocking layers such as Nb-doped  $\text{TiO}_2$  [57],  $\text{Al}_2\text{O}_3$  [58], and  $\text{Nb}_2\text{O}_5$  to get efficient improvement in suppressing the charge recombination.

## 2.2 Characterization methods of solar cells

The dye-sensitized solar cell is a complex device with several interfaces between the components. In this section, some of the most relevant techniques, such as I-V measurement, incident photon-to-electron conversion efficiency (IPCE), electrochemical impedance spectroscopy (EIS), and photocurrent transient measurement, are presented.

### 2.2.1 The solar resource and Air Mass

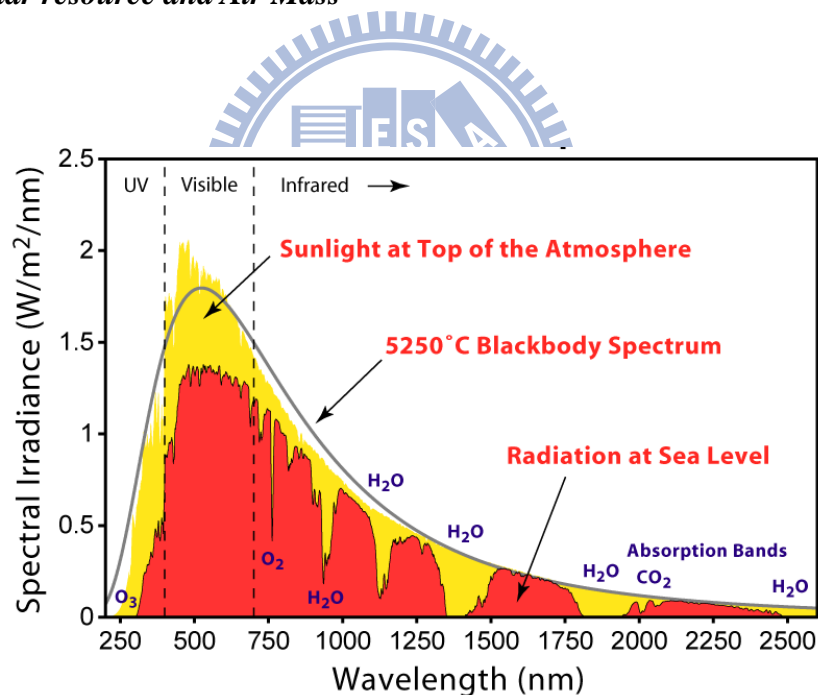


Fig. 2-4. Solar irradiance spectrum above the atmosphere and at the surface. [59]

The solar spectrum is a broad-band light source with different wavelengths, ranging from ultraviolet, visible and infrared regions of the electromagnetic spectrum.

According to the black-body radiation, the energy density per wavelength  $d e_{\gamma} / d \lambda$  can be

expressed as a function of  $\lambda$  by the equation shown below.

$$\frac{de_\gamma}{d\lambda} = \frac{2hc_m d\Omega}{\lambda^5} \frac{1}{e^{(hc_m/\lambda K_B T)} - 1} , \quad (2-7)$$

where  $d\Omega$  is solid angle element,  $c_m$  is the velocity of light in the medium,  $K_B$  and  $h$  is the Boltzmann constant and Planck constant, respectively. The maximum power of

the sun is at a wavelength of about 500 nm by taking  $d^2e_\gamma/d\lambda^2 = 0$  (at about 5,800 K).

The power density at the sun's surface is a huge value of  $62 \text{ MW m}^{-2}$  and it reduces to

$1353 \text{ W m}^{-2}$  at the point just outside the Earth's atmosphere since the solid angle

subtended by the sun,  $\Omega_s$ , is as small as  $6.8 \times 10^{-5} \text{ sr}$ . On passing through the

atmosphere, the spectrum is partially attenuated by the absorption of oxygen, ozone in

the ultraviolet region and water vapor, carbon dioxide, methane in the infrared.

The 'Air Mass' factor describe the attenuation from the absorption increases with the mass of air through which the radiation passes. For a thickness of  $l_0$  of the

atmosphere, the path length  $l$  through the atmosphere for radiation at an incident angle

$\alpha$  relative to the normal to the earth's surface is given by

$$l = l_0 / \cos\alpha . \quad (2-8)$$

The ratio  $l/l_0$  is called the Air Mass factor. The spectrum outside the atmosphere is

denoted as AM0 and AM1 means that sun light perpendicular incidence on the surface

of the earth. The standard spectrum for moderate weather is AM 1.5, which

corresponds to a solar incident angle of  $48^\circ$  relative to the surface normal ( $1/\cos 48^\circ \cong$

1.5) and gives a mean irradiance of  $1,000 \text{ W m}^{-2}$ . But the actual irradiation varies

with seasons, climates, day time and the different altitude area on the earth. For the laboratory measurement, the specification requirements of the solar simulator must be met for ASTM E927-05 standard and will be described in Section 3-3 in detail.

### **2.2.2 IV-measurement**

The photovoltaic (PV) performance of DSCs is estimated from the current-voltage (I-V) measurements, and the photovoltaic parameters, such as open circuit potential ( $V_{OC}$ ), short circuit current ( $I_{SC}$ ), fill factor (FF), and efficiency ( $\eta$ ), are also obtained. These parameters are typically measured under the standard condition of cell temperature 25 °C, incident light radiation of 100 mW cm<sup>-2</sup>, and the spectral power distribution of AM1.5.

Under illumination, the current-voltage characteristics follow the well-know equation below,

$$I(V) = I_{ph} - I_{dark} = I_{ph} - I_s(e^{qV/K_B T} - 1) = I_{ph} - I_s(e^{V/mV_T} - 1) , \quad (2-9)$$

where  $I_{dark}$  is the dark current of the diode,  $I_s$  is the saturation current of the diode (typically 10<sup>-7</sup> to 10<sup>-9</sup> A), and  $V$  is the voltage applied on the terminals of the cell.  $I_{ph}$  is the photocurrent that depends on irradiation intensity and  $V_T$  is often referred to as the thermal voltage that equals  $K_B T/q$  with  $q$  being the elementary charge. For non-ideal devices, an ideality factor ( $0 < m \leq 1$ ) is also used here to describe the weaker dependence of dark current on voltage. Figure 2-1 depicts an experimental

I-V characteristics of a DSC made with N719-sensitized TiO<sub>2</sub> (degusa P90) photoanode with 2 cm<sup>2</sup> active area, and together with the power curve. The following parameter can be derived with the I-V curve.

The V<sub>OC</sub> is measured under the condition when there is no external load connected, i.e., the circuit is broken or open. In this condition, there is no external current flow between the two terminals of the device, i.e.,  $I = 0$  and  $V = V_{oc}$ . From Eq. 2-9,

$$I_{ph} - I_s \left( e^{\frac{V_{oc}}{mV_T}} - 1 \right) = 0 \quad , \quad (2-10)$$

$$V_{OC} = mV_T \ln \left( \frac{I_{ph}}{I_s} + 1 \right) \cong mV_T \ln \left( \frac{I_{ph}}{I_s} \right) \quad . \quad (2-11)$$

V<sub>oc</sub> increases logarithmically with the photocurrent and the light intensity and it is also associated with the dark current. For the ideal diode (m=1), the diode has the minimum dark current and gets the maximum V<sub>oc</sub>.

The  $I_{sc}$  is measured at the condition when the applied voltage,  $V$ , equals zero. From Eq. 2-9,

$$I_{SC} = I_{ph} \quad , \quad (2-12)$$

where  $I_{sc}$  increases linearly with the light intensity.



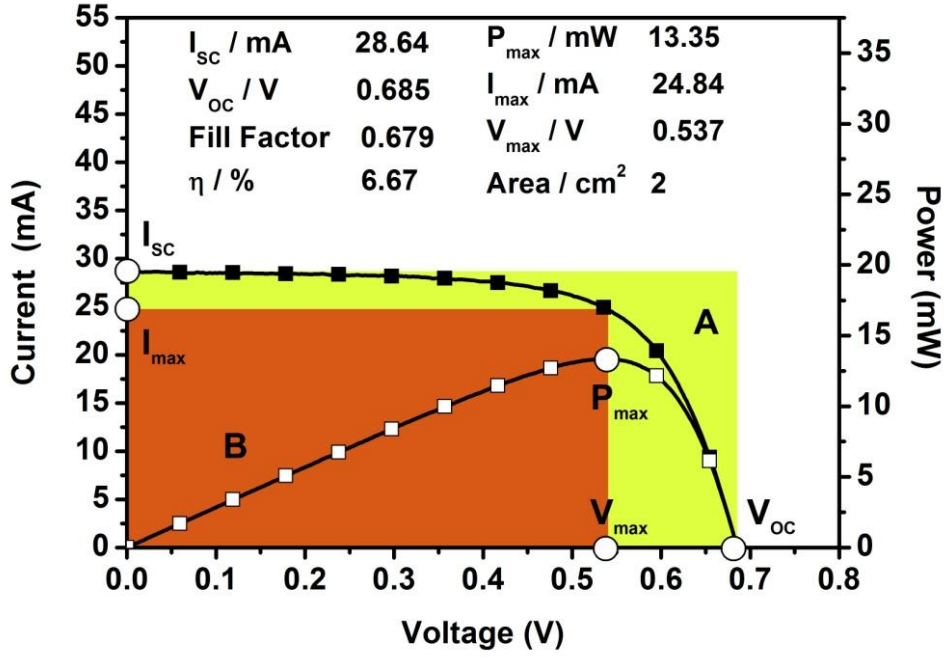


Fig. 2-5. Photovoltaic performance of a laboratory N-719-sensitized P-90 TiO<sub>2</sub> solar cell: I-V curve and parameters of DSCs output current (■) and power (□) as function of voltage measured under AM 1.5 standard test condition.

Fill factor (FF) is the most important parameters of a PV cell. It is defined as the ratio of maximum power output ( $P_{max} = I_{max} \times V_{max}$ ) and the product of  $V_{OC}$  and  $I_{SC}$ .

Therefore, from Fig. 2-1,

$$FF = \frac{I_{max} \times V_{max}}{I_{SC} \times V_{OC}} = \frac{\text{Area B}}{\text{Area A}} \quad (2-13)$$

Combining Eqs. 2-8 and 2-12, we obtain the approximation for  $FF$  in Eq. 2.13,

$$FF = \frac{V_{OC}/mV_T - \ln(1+V_{OC}/mV_T)}{1+V_{OC}/mV_T} \quad (2-14)$$

Typically,  $FF$  of DSC ranges from 0.5 to 0.8 depending on the individual device and usually increases with the decreasing light intensity.

It can be concluded that the more square-like I-V curve is essential for highly

desired FF. Finally, comparing the ratio of total output power ( $P_{out}$ ) with the solar power input ( $P_{in}$ ), the conversion efficiency ( $\eta$ ) can be measured,

$$\eta = \frac{P_{out}}{P_{in}} = \frac{V_{oc} \times J_{sc} \times FF}{P_{in}} . \quad (2-15)$$

The series ( $R_{ser}$ ) and shunt ( $R_{sh}$ ) resistances of a solar cell are also important parameters to its PV performance. In a DSC,  $R_{sh}$  stands for the leakage path across the dye/semiconductor interface, induced by defects in the semiconductor bulk and at the surface of the oxide.  $R_{sh}$  was calculated by the slope of the tangent line at  $I_{sc}$ . [60]  $R_{ser}$  is mainly series connected to the bulk resistances of semiconductor films, TCO substrate, metallic contacts, and electrolyte. It is determined by following methods:

(a) Different illumination level method

The method proposed by Wolf and Rauschenbach [61] is calculated from two I-V curves illuminated by two closed light intensities ( $P_1$  and  $P_2$ ). Series resistance was determined by using the given formula below:

$$R_{ser} = \frac{(V_1 - V_2)}{\Delta I} , \quad (2-16)$$

$$\Delta I = \frac{I_1(P_1 - P_2)}{P_1} , \quad (2-17)$$

where  $V_1$  and  $V_2$  are the voltages at light intensities  $P_1$  and  $P_2$ , respectively, and  $I_1$  is the current at light intensity  $P_1$ .

(b) Constant illumination level method

Ishibashi, et al. [60] proposed this method to calculate  $R_{ser}$  through a single I-V

curve of the solar cell.  $R_{ser}$  is determined from the slope of the plot of  $-dV/dI$  as a function of  $[I_{SC} - I - \{V - R_{ser}(I_{SC} - I) - nK_B T/q\}/R_{sh}]^{-1}$  by using the polynomial approximation.

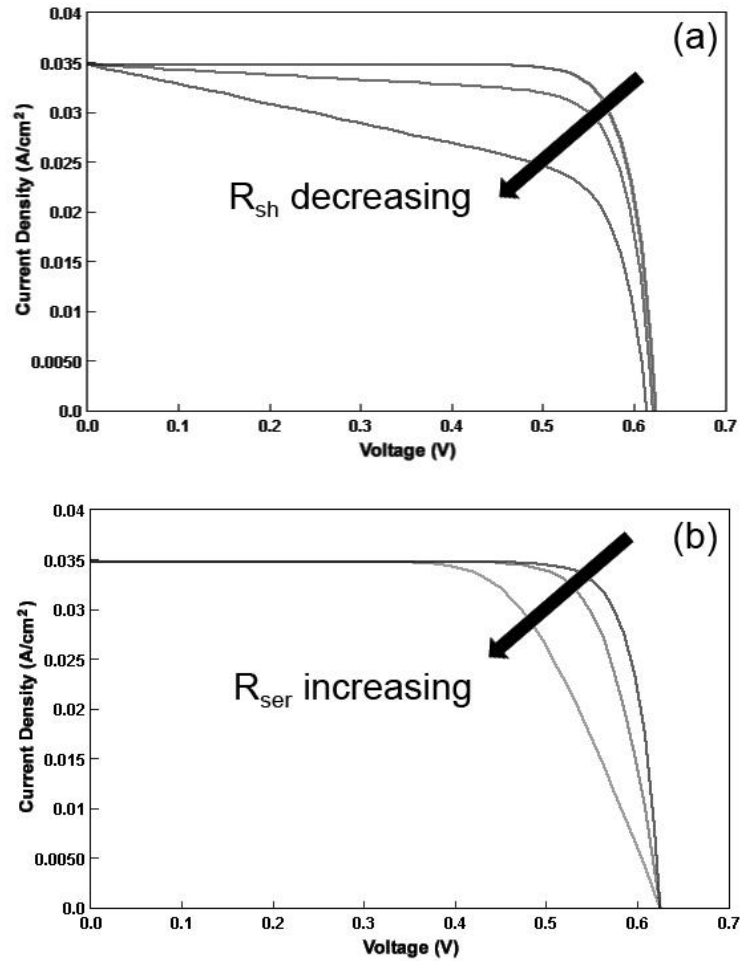


Fig. 2-6. The effect of (a) shunt and (b) series resistances on PV performance through computing simulation. The area of the solar cell is 1 cm<sup>2</sup>.

The main impact of series and shunt resistances is to reduce the fill factor, although excessively high values may also reduce the short-circuit current. In addition, low shunt resistance causes power loss in solar cells by providing an alternate current path

for the light-generated current, the so-called dark current. Such a diversion reduces the voltage from the solar cell. The effect of the series and shunt resistances on the IV curve is shown. [62]

### 2.2.3 Incident proton to current conversion efficiency

Incident proton to current conversion efficiency (IPCE) is the measurement of spectral response of the cell that contains the partial information of quantum efficiencies of photocurrent generation processes such as the light harvesting ( $\eta_{LH}$ ), electron injection ( $\eta_{INJ}$ ), and charge collection efficiency ( $\eta_{COL}$ ) as

$$\eta_{IPCE}(\lambda) = \frac{J_{SC}(\lambda)}{q\Phi(\lambda)} = \eta_{LH}(\lambda)\eta_{ING}(\lambda)\eta_{COL}(\lambda) , \quad (2-18)$$

where  $J_{SC}$  is the short circuit current density of the DSCs at incident monochromatic light with wavelength  $\lambda$ ;  $q$  and  $\Phi$  are the elementary charge and photon flux, respectively. [63] Following each step of conversion,  $\eta_{LH}$  is associated with the ability of the dye in absorbing photons.  $\eta_{INJ}$  represents the excited electron injected from the LUMO of dye molecule to the conduction band of metal oxide. Finally, the electron collection efficiency ( $\eta_{COL}$ ) is the amount of electrons that effectively reach the electron collector (eg. FTO or ITO substrate) avoiding recombination. It should be noted that IPCE measurement is performed under short circuit condition, where electron lifetime is higher. It is noteworthy that the high fraction of IPCE is most

important for efficient DSCs and the mesoporous metal oxide with high surface area is the prerequisite for higher IPCE value.

#### **2.2.4 Electrochemical impedance spectroscopy and model of the equivalent circuit**

Electrochemical impedance spectroscopy (EIS) is one of the most powerful methods to probe DSCs and that can provide sufficient information about the electrochemical reactions in the devices. In EIS experiment, the device is under illumination or dark, and controlled by an applied harmonically modulated bias,  $\Delta V = V_{\text{amp}}e^{i\omega t}$ , as a small perturbation. An increase of  $\Delta V$  on the device will cause a current flow,  $\Delta i = i_{\text{amp}}e^{i(\omega t - \theta)}$ , with a phase delay  $\theta$ . The impedance of the device is thus given by

$$Z_{\text{EIS}} = \left| \frac{\Delta V}{\Delta i} \right| = \left| \frac{V_{\text{amp}}}{i_{\text{amp}}} \right| e^{i\theta} . \quad (2-19)$$

Recently, the interpretation of the EIS spectrum of a DSC has been thoroughly discussed by several models. In this thesis, a transmission line model is used to describe the typical Nyquist and Bode plots of EIS in the system, as shown in Fig. 2-7. This model is explained by the multiple trapping proposed by J. Bisquert, who assumed that the electron diffusion and recombination occur only via the conduction band of metal oxide and by trapping and detrapping events. [64-67] Accordingly, the RC time constants of three peaks are shown in the Bode plot.

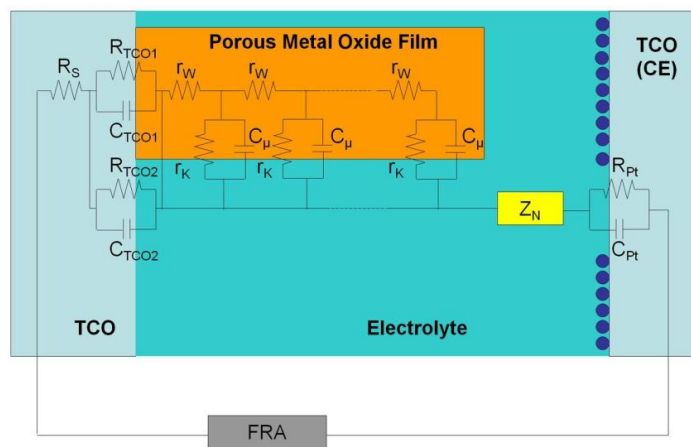
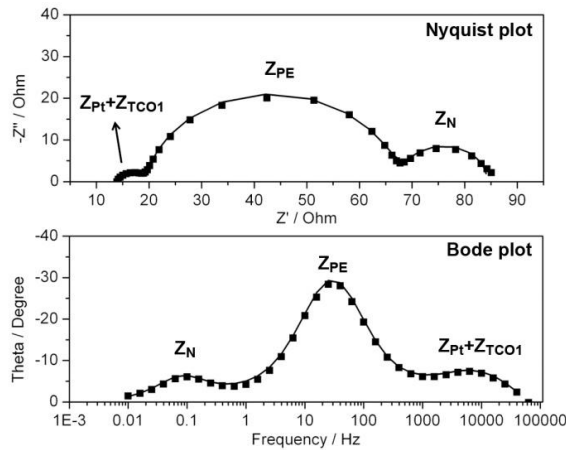


Fig. 2-7. Typical Nyquist and Bode plots of impedance spectra for a DSC. Experimental data are plotted in black squares and the fitting is in solid lines by the transmission line model of equivalent circuit.

In the transmission line model, the whole metal oxide porous film is treated as an interconnected network. Under a modulated bias, electrons are injected from the TCO substrate into the metal oxide and the electron propagates through individual particles with a transport resistance of  $r_w$ . Some of the electrons recombine with the oxidized species in the electrolyte, such as  $I_3^-$  commonly, characterized by a charge transfer resistance of  $r_k$  and a capacitance of  $c_\mu$ , and the rest of the electrons are then recaptured by the TCO current collector during the opposite phase of the sinusoidal

voltage modulation. Assume the thickness of metal oxide porous film is  $L$ , the electron transport resistance is  $R_W = r_W \times L$ , the interfacial charge recombination resistance is  $R_K = r_K/L$  and the chemical capacitance of the film is  $C_\mu = c_\mu \times L$ , where the lower case letters represent that the resistances and the capacitance are normalized to the film thickness. The diffusion–recombination model based on the following three assumptions: (1) electrons in the conduction band diffuse, (2) there is no trap, and (3) an irreversible first-order reaction is assumed for the recombination.

[67] The impedance of the metal oxide porous PE can be obtained as follow:

$$Z_{PE} = \frac{R_W}{\sqrt{\left(\frac{R_W}{R_K}\right)\left(1 + \frac{i\omega}{\omega_K}\right)}} \coth \left[ \sqrt{\left(\frac{R_W}{R_K}\right)\left(1 + \frac{i\omega}{\omega_K}\right)} \right] , \quad (2-20)$$

where  $\omega_K$  is the recombination rate. The equation can be further classified into the following three cases:

(a)  $R_K \rightarrow \infty$ , the limiting case leads to the simple diffusion case,

$$Z_{PE} = R_W \left( \frac{1}{3} - i \frac{\omega}{\omega_d} \right) . \quad (2-21)$$

Thus, the real part,  $Z'_{PE}$ , of impedance  $Z_{PE}$  approaches  $(R_W/3)$  and the imaginary part,  $Z''_{PE}$ , of impedance  $Z_{PE}$  becomes  $\infty$ .

(b)  $R_K \gg R_W$  : When the reaction resistance,  $R_k$ , is finite, Eq. 2-19 is expressed by

Eq. 2-21:

$$Z_{PE} = \frac{1}{3} R_W + \frac{R_K}{1 + \frac{i\omega}{\omega_K}} . \quad (2-22)$$

This equation means that there is a small increase part along the straight line of  $Z'$

$= -Z''$  at high frequency and a large arc at low frequency. The latter corresponds to the recombination process, which is much slower than diffusion through the metal oxide PE in this case. And two important relationships can be derived. The peak frequency of an arc in a Nyquist plot,  $\omega_{\max}$ , is given as

$$\omega_{\max} = \omega_K . \quad (2-23)$$

The dc resistance,  $R_{dc}$ , at  $\omega = 0$  is given as

$$R_{dc} = \frac{1}{3}R_W + R_K . \quad (2-24)$$

(c)  $R_K \ll R_W$  leads to the following equation:

$$Z_{PE} = \sqrt{\frac{R_W R_K}{1 + \frac{i\omega}{\omega_K}}} . \quad (2-25)$$

This case must be avoided for attainment of the highly efficient cells. The following two relationships are also derived.

$$\omega_{\max} = \sqrt{3}\omega_K , \quad (2-26)$$

$$R_{dc} = \sqrt{R_W R_K} . \quad (2-27)$$

From the shapes of the Nyquist plot of the PE impedance (in the 10–100 Hz range),  $\omega_K$  and  $R_K$  are estimated from the peak frequency,  $\omega_{\max}$ , and the diameter by using Eqs. 2-22, 2-23, 2-25 and 2-26, respectively. The effective electron diffusion coefficient in metal oxide porous film can be calculated by the following equation:

$$D_{\text{eff}} = \left(\frac{R_K}{R_W}\right)L^2 \omega_K . \quad (2-28)$$

The electron diffusion length in metal oxide porous film,  $L_n$ , is given by

$$L_n = L \sqrt{\frac{R_K}{R_W}} . \quad (2-29)$$



Regeneration of  $I_3^-$  at the counter electrode (CE) is characterized by  $R_{Pt}$  and  $C_{Pt}$ , which are the charge transfer resistance and double layer constant phase element (CPE, stands for an imperfect capacitor) at the platinized TCO, respectively.  $R_{TCO1}$  and  $C_{TCO1}$  are the resistance and the CPE at the TCO and photoanode contact, respectively. The subscript “TCO2” stands for the interface at the exposed TCO/electrolyte, and the resistance and the CPE change with surface conditions (blocking layer and cleanliness). The impedances at these three interfaces can be described approximately by the following simple RC circuit,

$$Z = \frac{1}{\frac{1}{R} + i\omega C} \quad (2-30)$$

The finite Warburg impedance of the low frequency arc (in the mHz range) describes the diffusion of tri-iodide ions in the electrolyte,

$$Z_N = R_D \frac{1}{\sqrt{\frac{D_I}{\delta^2}}} \tanh \left[ \sqrt{\frac{D_I}{\delta^2}} \right],$$

$$R_D = \frac{k_B T}{m^2 q^2 A_V C^* D_I \delta}, \quad (2-31)$$

$$\omega_{\max} \approx 2.5 \frac{D_I}{\delta^2},$$

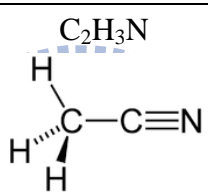
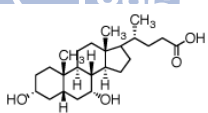
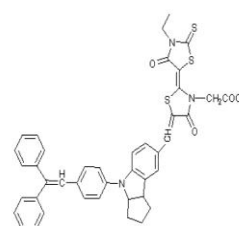
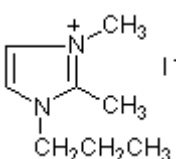
where  $D_I$  and  $\delta$  represent the diffusion coefficient of  $I_3^-$  and the thickness of the liquid film, respectively. The number of electrons transfer in each reaction,  $m$ , is 2 in  $I_3^-/I^-$  redox case.  $A_V$  and  $C^*$  are Avogadro's constant and the concentration of  $I_3^-$  in the bulk, respectively.

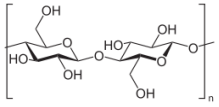
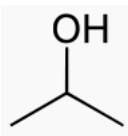
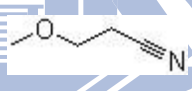
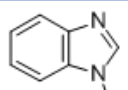
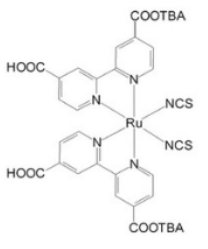
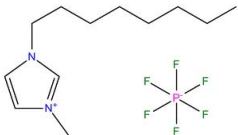
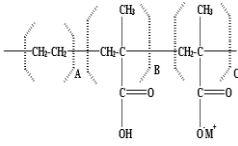
# Chapter 3 Experimental setups and procedures

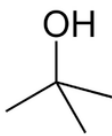
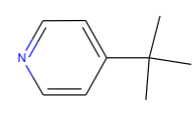
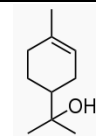
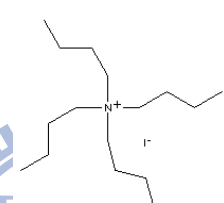
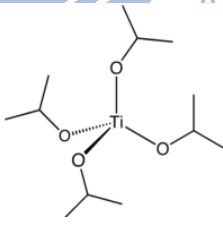
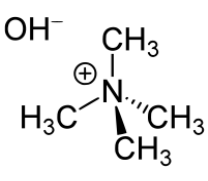
## 3.1 Materials

### 3.1.1 Commercial materials

Here, the materials and reagents used in our experiments without further purification are listed below.

Name	Chemical Formula	Supplier	Note
Acetonitrile (AN)	$C_2H_3N$ 	J.T. Baker	HPLC grade
Chenodeoxycholic acid (CDCA)	$C_{24}H_{40}O_4$ 	Sigma-Aldrich	
Chloroplatinic acid hexahydrate	$H_2PtCl_6 \cdot 6H_2O$	Showa	
D149 indoline dye	$C_{42}H_{35}N_3O_4S_3$ 	Mitsubishi Paper Mills Limited	
1,2-dimethyl-3-propylimidazolium iodide (PMII)	$C_8H_{15}N_2I$ 	Merck	

Ethyl cellulose (EC)	$[C_6H_7O_2(OH)_{3n}(C_2OH_5)_n]_x$	Fluka	5–15 mPa s, #46070
			30–70 mPa s, #46080
Fluorine-doped tin oxide glass (FTO glass)	—	Nippon Sheet Glass Co. Ltd.	8-10 $\Omega/\square$ 3 mm thick
Indium tin oxide coated polyethylene naphthalate film (ITO/PEN)	—	Tobe, Inc	10 $\Omega/\square$ 120 $\mu\text{m}$ thick
Iodine	$I_2$	Sigma-Aldrich	99.8%
Isopropyl alcohol (IPA)	$(CH_3)_2CHOH$ 	Merck	Analysis Grade
Lithium iodide	$LiI$	Merck	
3-methoxypropionitrile (MPN)	$C_4H_7NO$ 	Alfa Aesar	
N-methylbenzimidazole (NMBI)	$C_8H_8N_2$ 	Sigma-Aldrich	
N719 Ruthenium dye	$C_{58}H_{86}N_8O_8RuS_2$ 	Solaronix (Aubonne, Switzerland)	
1-Octyl-3-methylimidazolium hexafluorophosphate ( $C_8\text{MImPF}_6$ )	$C_{12}H_{23}N_2PF_6$ 		
Surlyn		DuPont	Random copolymer poly (EMAA)

Sodium borohydride	$\text{NaBH}_4$		
<i>tert</i> -butyl alcohol ( <i>t</i> -BuOH)	 $\text{C}_4\text{H}_{10}\text{O}$	Sigma-Aldrich	
4- <i>tert</i> -butylpyridine (TBP)	 $\text{C}_9\text{H}_{13}\text{N}$	Sigma-Aldrich	
Terpineol	 $\text{C}_{10}\text{H}_{18}\text{O}$	Fluka	Anhydrous, #86480
Tetrabutylammonium iodide (TBAI)	 $\text{C}_{16}\text{H}_{36}\text{NI}$	ACROS	
Titanium isopropoxide	 $\text{C}_{12}\text{H}_{28}\text{O}_4\text{Ti}$		
P90 $\text{TiO}_2$	$\text{TiO}_2$	Degussa AG, Germany	a kind gift
Tetramethylammonium hydroxide (TMAH)	 $\text{C}_4\text{H}_{13}\text{NO}$	Sigma-Aldrich	
Zinc powder	$\text{Zn}$	Alfa Aesar	10 $\mu\text{m}$ size
Commercial $\text{ZnO}$ (C-ZnO) NPs	$\text{ZnO}$	Seedchem, Australia	

### 3.1.2 Synthesize tetrapod-like ZnO nanoparticles

In this study, a novel DC plasma reactor was used to synthesize tetrapod-like ZnO (T-ZnO) nanoparticles (NPs) at 70 kW operation power and atmospheric pressure. The synthesis rate of the T-ZnO NPs could be over  $1 \text{ kg hr}^{-1}$  easily. Here, the briefly synthesis procedure is described as the following. Commercial zinc powder (Alfa Aesar) with an average particle size of  $10 \mu\text{m}$  with less than 50 ppm impurities of Cr, Fe and Pb were used as the raw material. In the plasma flame, the zinc powders subsequently undergo vaporization, oxidation and quench processes. Here the plasma-forming gas, carrier gas, and quenching gas are 50%Ar + 50%N<sub>2</sub>, N<sub>2</sub>, and Air + N<sub>2</sub>, respectively.

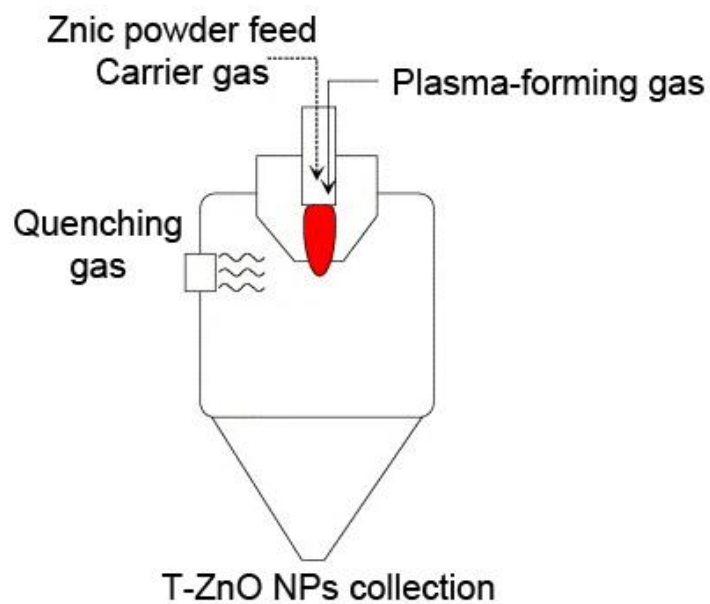
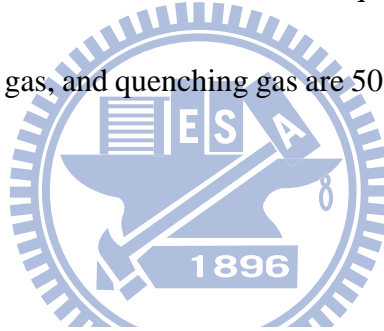


Fig. 3-1 . Schematic of the DC plasma reactor.

### ***3.1.3 Formation of TiO<sub>2</sub> Nanoscale Materials***

Through sol-gel growth in a basic solution, the scattered TiO<sub>2</sub> NPs with ca. 100 nm diameter were synthesized. Mixing 58.6g titanium isopropoxide with 290 mL distilled water yielded a colloidal suspension, which was then filtered and placed in an autoclave containing 20mL tetramethylammonium hydroxide (TMAH) at 250°C for 12 hours. Finally, the solution in the autoclave was washed by DI water and centrifuged.

## **3.2 Preparation of dye-sensitized solar cell**

The dye-sensitized solar cell is basically sandwiched together with the photoanode electrode (PE), electrolyte, and counter electrode (CE), shown in Fig. 3-2. The internal space of the PE and CE was separated by a hot-melting spacer, such as Surlyn, and was filled through a hole with an electrolyte solution. Finally, the hole was sealed with a cover glass (0.1 mm thickness) by using a hot-melt film or UV adhesive cured by OPAS RS-300. In this section, the preparations of the electrodes and the composition will be detail described.

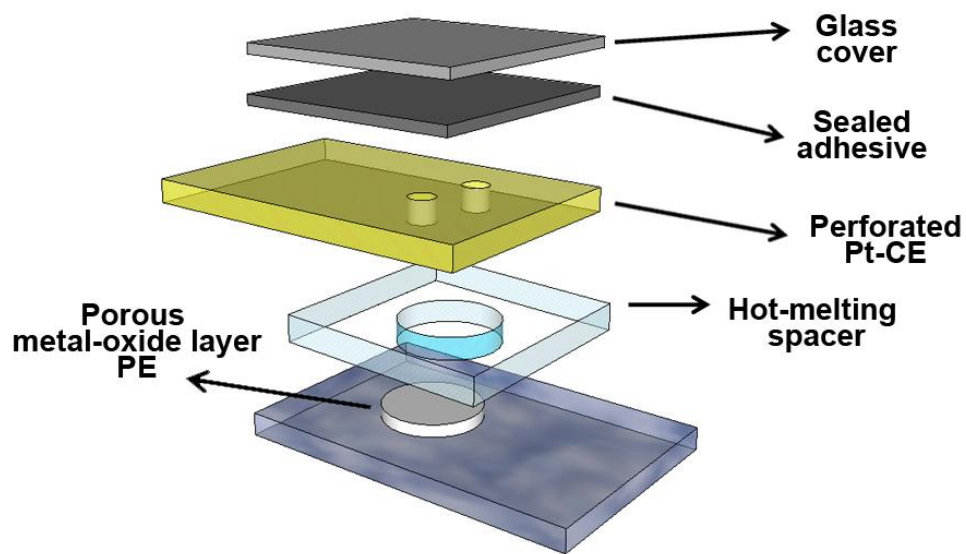


Fig. 3-2. Configuration of the dye sensitized solar cells.

### 3.2.1 Photoanode electrode

#### *ZnO photoanode electrode*

Both for tetrapod-like ZnO (T-ZnO) and commercial ZnO (C-ZnO), the ZnO pastes for screen-printing were prepared typically by mixing ZnO powder, ethyl cellulose (EC), and terpineol, and the detailed procedure is as follows. EC (5–15 mPa s, #46070, Fluka) and EC (30–70 mPa s, #46080, Fluka) were dissolved in ethanol to yield 10 wt% solution, individually. 12g EC (5–15) and 12g EC (30–70) were added to a round bottomed rotavap flask containing 12g ZnO powders, and 25g terpineol. The mixture paste was dispersed in an ultrasonic bath. And a rotary-evaporator (BUCHI V850) is used to remove the ethanol and water in the mixture paste. Finally, the paste was made with a three-roll mill (EXAKT E50).

To prepare the ZnO photoanode electrode (PE), the NSG FTO glass used as current collector was first cleaned in a detergent solution using an ultrasonic bath for 15 min, and then rinsed with water and ethanol. After UV-O<sub>3</sub> treatment for 20 min, a layer of ZnO paste with 0.238cm<sup>3</sup> area was coated on the FTO glass by screen-printing without blocking layer on the substrate. And then, the substrate was kept in a clean box for 10 min so that the paste can relax to reduce the surface irregularity and then dried for 10 min at 90 °C. This screen-printing procedure with ZnO paste (coating, storing and drying) was repeated to get an appropriate thickness of 5 to 42 μm for the PE. The electrodes coated with the ZnO pastes were gradually heated under O<sub>2</sub> flow as the temperature evolution shown in Fig. 3-3, in order to remove the organic EC in the paste and neck the NPs.

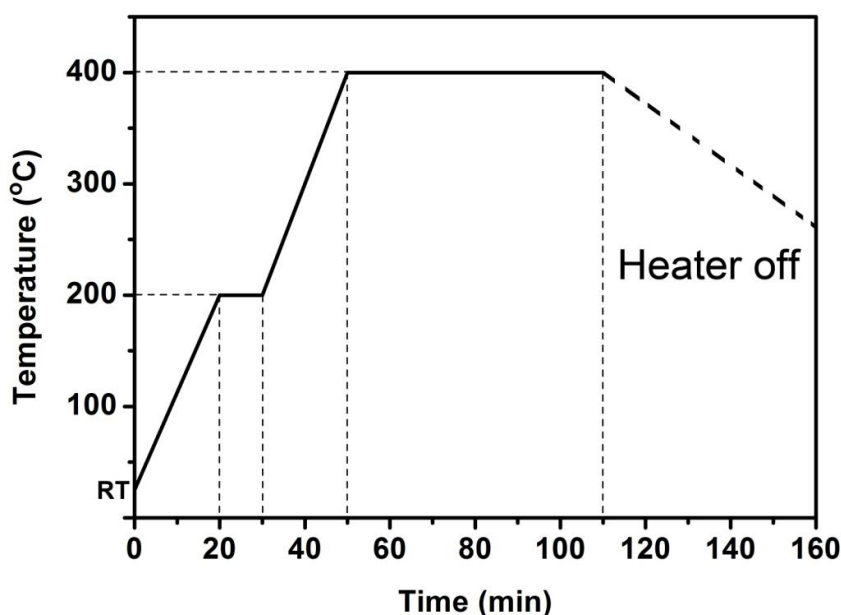


Fig. 3-3. Heating curve for ZnO photoanode electrode.



After cooling to room temperature (RT), the ZnO PE was immersed into a solution made of 0.5 mM D149 organic sensitizer and 1 mM CDCA in AN/*t*-BuOH mixture (*v/v* = 1 : 1) at 65 °C for 30 min, and the PE was then rinsed with AN to remove excess dye molecular on it.

### *Flexible TiO<sub>2</sub> photoanode electrode*

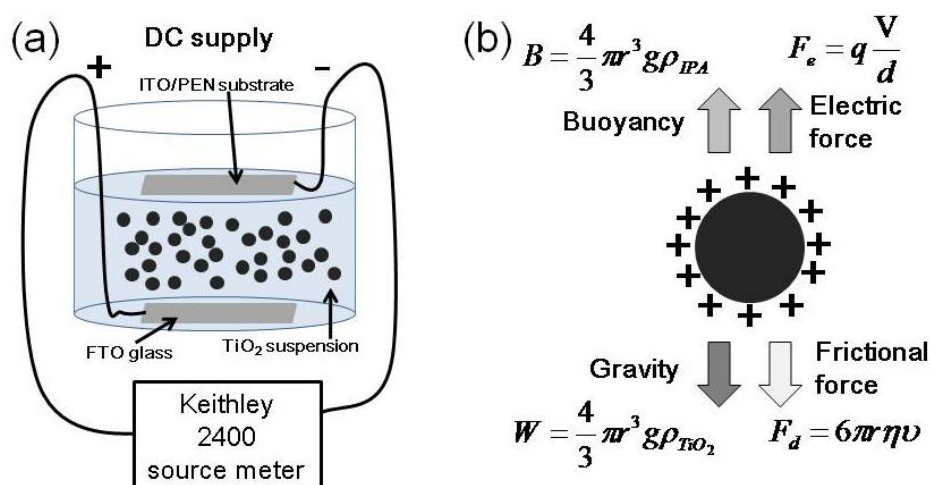


Fig. 3-4. Sketch schemes of the electrophoretic cell, the preparation of TiO<sub>2</sub> electrodes, and the significant parameters in EPD process.

ITO/PEN substrates were cleaned with mild soap and ethanol, thoroughly rinsed with deionized water (18.2 MΩ), then dried by a clean air stream. In this part, electrophoretic deposition (EPD) was used to fabricate the flexible TiO<sub>2</sub> photoanode film on ITO/PEN substrate. The TiO<sub>2</sub> suspension for EPD consisted of 0.25g TiO<sub>2</sub> in 100mL IPA, and stirred with a magnetic stirrer overnight; it was ultrasonically

dispersed for 1.5 hrs before adding into the electrophoretic cell as shown in Fig. 3-4 (a). The two electrophoretic electrodes of fluorine-doped tin oxide (F:SnO<sub>2</sub>, FTO) conductive glass, and ITO/PEN film were separated by 1.5 cm, and served as the cathode and anode electrode, respectively. The dispersed TiO<sub>2</sub> NPs, that have positive electric surface charge, are forced by an external electric field to overcome the gravity and the friction force, and deposited onto the ITO/PEN substrate. A Keithley 2400 Source Meter was applied as a power supply for different currents and deposition durations at the constant current mode which was more effective and controllable than the constant voltage mode [68]. After drying TiO<sub>2</sub>-deposited ITO/PEN substrate at RT and one atmospheric pressure, high pressure treatment enhanced the photovoltaic performance of the device.

The EPD TiO<sub>2</sub> PE was immersed in a solution of 0.5 mM N719 dye solution in AN/*t*-BuOH (v/v=1:1) binary solvent at 40 °C for 4 hrs to adsorb sufficient N719 dye for light harvesting. To remove the remaining dye, the dye-sensitized photoanode was rinsed with AN, and dried under atmosphere condition at RT.

### ***3.2.2 Electrolyte***

The electrolyte plays an important role in the process of dye regeneration or the so-called hole-transport material (HTM). For different functions or optimization for

different cells, the composition of the electrolyte will be quite different. In this research, we used several electrolytes listed in Table 3-1.

Table 3-1. The compositions of the electrolytes used in different chapter of this thesis.

Electrolyte #	Compositions	Used in
EL 1	0.6 M PMII, 0.05 M I <sub>2</sub> , and 0.5 M TBP in AN	4-3 ~ 4-4
EL 2	0.2 M I <sub>2</sub> , 0.5M TBP in PMII/C <sub>8</sub> MImpF <sub>6</sub> mixture (v/v=35:65)	4-5
EL 3	0.4 M LiI, 0.4 M TBAI, 0.04M I <sub>2</sub> and 0.5 M NMBI in AN/MPN mixture (v/v=1:1)	5-1 ~ 5-3
EL 4	0.8 M TBAI, 0.1 M I <sub>2</sub> , and 0.5 M NMBI in MPN	5-4
EL 5	0.8 M PMII, 0.1 M I <sub>2</sub> , and 0.5 M NMBI in MPN	5-4
EL 6	0.5 M PMII, 0.05 M I <sub>2</sub> in MPN	5-4
EL 7	0.5 M LiI, 0.05 M I <sub>2</sub> in MPN	5-4

### 3.2.3 Counter electrode

#### *High-temperature process*

To prepare the counter Pt-electrode, two holes (< 1 mm diameter) were drilled in the FTO glass by a drilling machine. The perforated substrate was washed in a detergent solution using an ultrasonic bath for 15 min, and then rinsed with water and ethanol. After removing residual organic contaminants by heating in air for 20 min at 400 °C, the Pt catalyst was deposited on the FTO glass by dip-coating with the H<sub>2</sub>PtCl<sub>6</sub>

solution (2 mg Pt in 1 ml IPA) with repetition of the heat treatment at 400 °C for 20 min.

### ***Low-temperature process***

The screen-printing paste prepared by dissolving H<sub>2</sub>PtCl<sub>6</sub>·6H<sub>2</sub>O (0.6, 1.2, and 1.8 w.t.%) in terpineol solution were screen-printed on the substrate using a 250 mesh screen and then dried at 60 °C for 20 min. Then the Pt ions on the electrodes were reduced by immersing it in 10mM NaBH<sub>4</sub> aqueous solution at 40 °C. And the reduced reaction is shown below. After 2 h, the electrodes were rinsed with distilled water and then dried at 60 °C for 20 min. Then, the UV-O<sub>3</sub> post-treatment were applied for 20 min:



### ***3.2.3 Sealing and additional materials***

A sealing material prevents the leakage and the evaporation of the electrolyte solvent. Chemical stability and mechanical strength of the sealing material against the chemical components in the electrolyte and the cell-broken is required. Surlyn (Du Pont), a copolymer of ethylene and acrylic acid, meets the chemical requirements. For mechanical strength requirements, the additional UV-gel is used in this study.

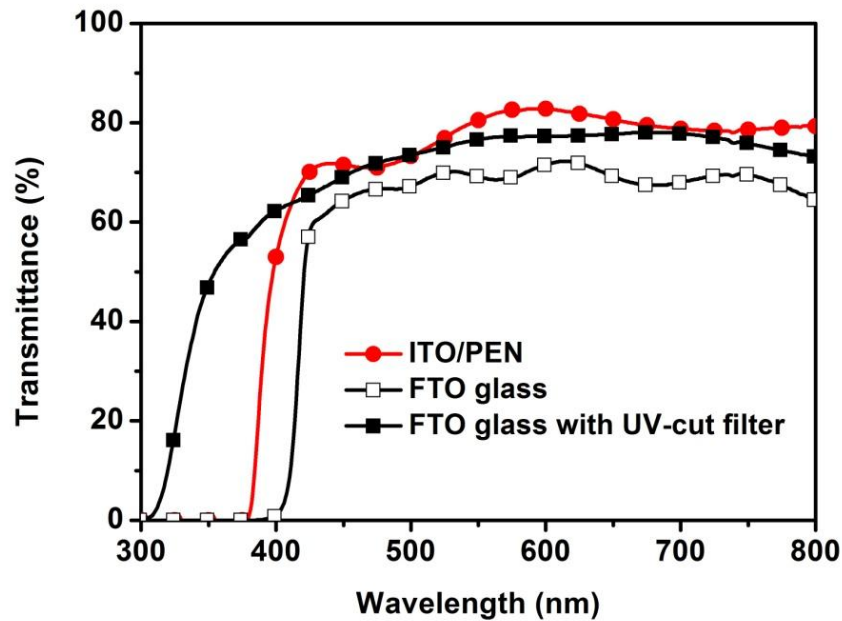


Fig. 3-5. The transmittance spectra of the substrates used in this study.

In order to avoid the degradation of dye in long-term stability test, it is necessary to use UV-cut filters in DSC with FTO/glass substrates to cut the photon with energy 4.13eV (300 nm) to 3.1eV (400 nm) shown in Fig. 3-5. However, the DSC made by polymer ITO/PEN substrate in this study didn't use any UV-cut filter due to the cut-off wavelength of ITO/PEN is about 380 nm.

### 3.3 Device measurement

To establish the characteristics of the DSC, solar cells and its components will go through the testing measurements applied below:

The morphologies and dimensions of the samples were characterized using a

JEOL-6500 field emission scanning electron microscope (FESEM) operated at 10 KeV. The advanced structures were analyzed using a JEOL JEM-2100F field emission transmission electron microscope (FETEM) operated at 200 KeV. The surface area of the nanoparticles (NPs) was achieved by Micromeritics ASAP (Accelerated Surface Area and Porosimetry System) 2010. The phases were characterized using an X-ray diffractometer (XRD, Philip PW1700) operated at 40 keV and 40 mA with Cu K $\alpha$  radiation. The scanning step size and the collection time for each step were set at 0.02° and 5 s, respectively. The film thickness of the photoanode was measured by Surfcoorder ET-3000 (Kosaka Laboratory Ltd.). The macro-structure of the sample was observed by an optical microscopy (Nikon). The UV-visible spectra were measured on a Hitachi U-2800 spectrophotometer.

For current–voltage characteristics, the white light source (Yamashita Denso, YSS-100A) was used to give an irradiance of 100 mWcm<sup>-2</sup> (the equivalent of one sun at AM1.5) on the surface of the solar cell, and the data was collected by an electrochemical analyzer (Autolab, PGSTAT30) at a temperature of 25±2 °C. The scan rates of AN-based and IL-based DSC were 0.05 and 0.005 Vs<sup>-1</sup>, respectively. The light power was calibrated by using a reference cell of silicon photodiode (BS-520, Bunko Keiki) before each measurement. The spatial uniformity, spectral content and temporal stability testing, which were classified every month, are shown in Figs. 3-6,

3-7, and 3-8. The calibration certificate validates Class AAA performance for ASTM E927-05 standard. The white light source is certified to Class AAA performance for all 3 standards shown in Table 3-2 in order to ensure the accuracy of the measurement.

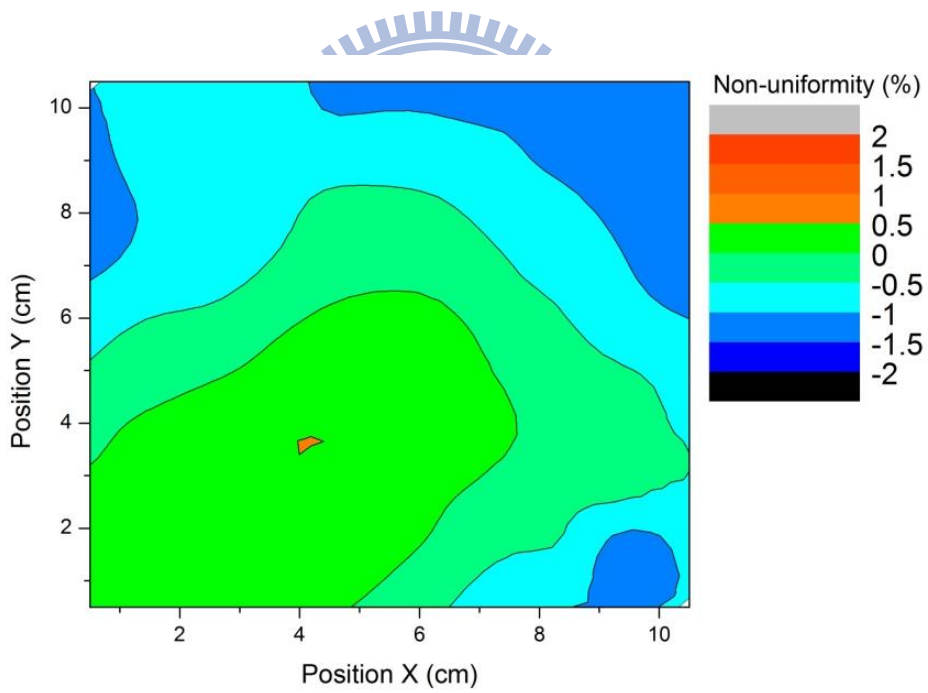


Fig. 3-6. The uniformity of the white light source (Yamashita Denso, YSS-100A).

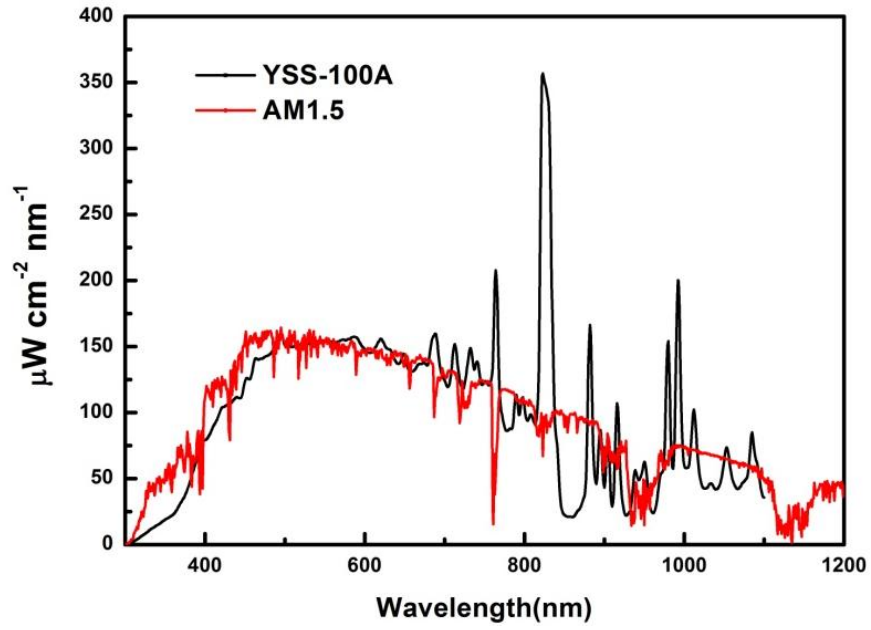


Fig. 3-7. The standard AM 1.5 spectrum compared with the spectrums from the white light source (Yamashita Denso, YSS-100A).

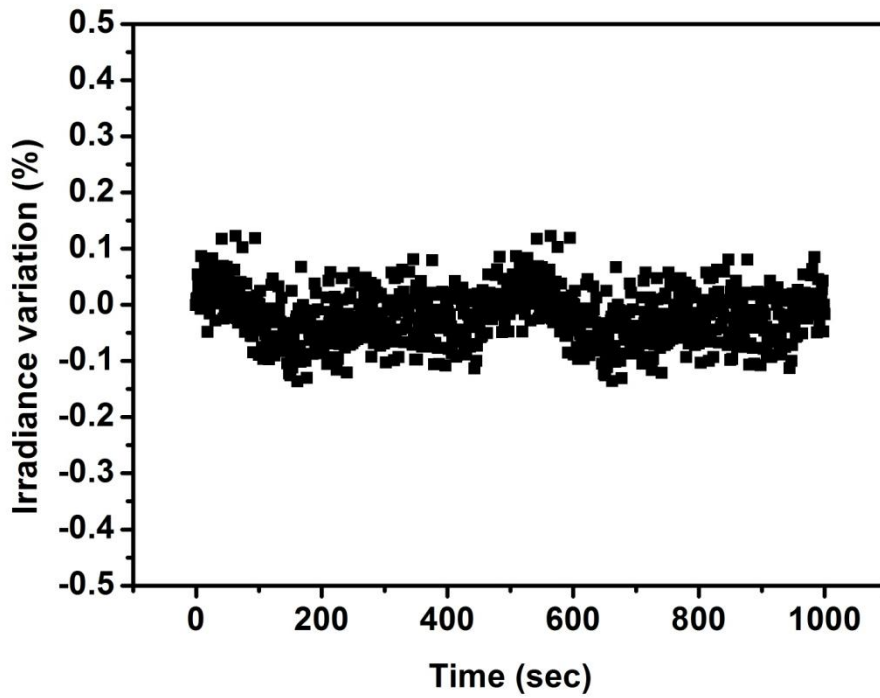


Fig. 3-8. The output variation of the white light source (Yamashita Denso, YSS-100A) utilizing a 1 second data acquisition time and after 15 minutes lamp warm-up.



Table 3-2. Class AAA Standards and Specifications

Organization	IEC	JIS	ASTM
Performance Parameter	60904-9-2007	C 8912	E92-05
Spectral Mismatch	0.75% - 1.25%	0.75% - 1.25%	0.75% - 1.25%
Non-Uniformity of Irradiance	2.0%	<±2%	2%
Temporal Instability	0.5% STI	<±1%	2%
	<2.0% LTI		

The impedance measurements were carried out applying a bias of the open circuit voltage ( $V_{oc}$ ), by using an electrochemical analyzer (Autolab, PGSTAT30) at a temperature of  $25 \pm 2$  °C. The EIS measurements of AN-based DSC were recorded in a frequency range from 50 mHz to 1 MHz with AC amplitude of 10 mV, and the frequency range was set from 1 mHz to 1 MHz for the IL-based DSC.

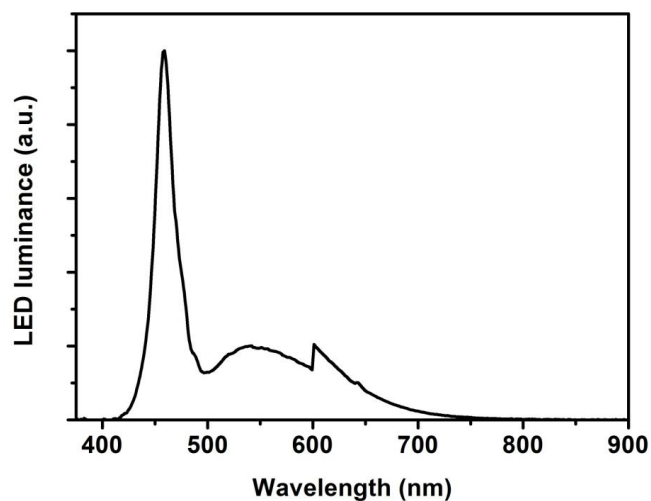


Fig. 3-9. Emission spectrum of the white LED array.

An IPCE measurement system (C-995, PV-measurement Inc.) measured the action spectra of the incident monochromatic photon-to-current conversion efficiency (IPCE) for solar cells. A white LED array, whose emission spectrum is shown in Fig. 3-9 and covers the range of dye absorption, serves as an additional light bias source in IPCE measurement. In order to minimize the capacitance effect of the DSC [69], the chopper frequency was set to 4 Hz.

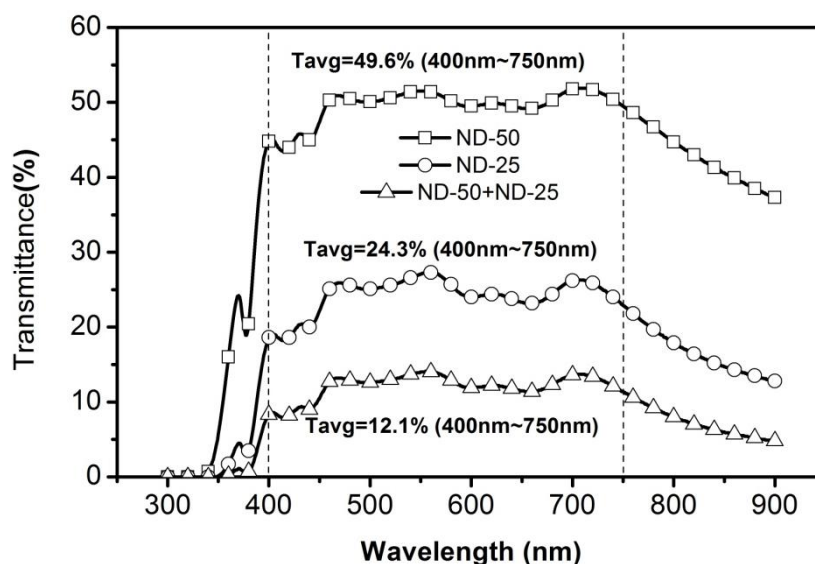


Fig. 3-10. Measured spectral transmittance for ND filters used in this study.

All photocurrent transient experiments were performed at RT by illumination with the white light source (Yamashita Denso, YSS-100A) and series neutral density (ND) filter (Edmund Optics). In Fig. 3-10, the transmittance spectra of ND filter are uniformly attenuated in the 400-700nm wavelength range, which is also the mainly response range for dye absorber. The time evolution of the photocurrent was

collected with the electrochemical analyzer (Autolab, PGSTAT30).

The durability test in this study including visible light irradiation ( $100 \text{ mW/cm}^2$ ) and thermal stress ( $60 \text{ }^\circ\text{C}$ ) aging of hermetically sealed cells with UV-cut filter was performed with a sun test xenon arc lamp (ATLAS Ci3000 xenon Fadeometer). Following a period of continuous light irradiation, PV measurements were taken after the cells cooled to RT.



# Chapter 4 Towards efficient tetrapod-like ZnO dye-sensitized solar cells

In this chapter, we reported that the photoanode film composed by tetrapod-like ZnO (T-ZnO) nanoparticles (NPs), which were fabricated by a novel DC plasma method, with D149 dye provides good electron transport and light harvesting to achieve conversion efficiency as high as 4.9%. On the other hand, the T-ZnO porous framework is for not only efficient electron transporting in ZnO photoanode but also well ionic diffusion in the electrolyte film. These related behaviors were also analyzed and discussed via the IPCE, photocurrent transient dynamics, and EIS.

## 4.1 Physical properties

The quality of photoanode film is an important issue for the performance of the DSCs, due to the condition of the dye absorption and ability of electron transport in the photoanode. Figure 4-1(a) shows the top-view image of screen-printing tetrapod-like ZnO (T-ZnO) film. The T-ZnO nanoparticles (NPs) construct a good and dense porous thin film on the FTO glass substrate by connecting with each other and forming

a porous network. The porous network can provide an efficient pathway to transport the photocurrent injected from the excited dye molecules. Each of the T-ZnO NPs consists of four crystalline pods with a diameter and a length of about 30 nm and 100–400 nm, respectively. Further examinations of the crystalline quality of the T-ZnO powders were performed with FETEM as shown in Fig. 4-1(b). The high resolution FETEM image shows each arm of the T-ZnO was preferentially oriented in the c-axis direction with the single-crystal wurtzite structure, and the distance between lattice planes was measured to be 5.2 Å corresponding to the lattice constant of ZnO (002) plane, which is the same as a single crystalline nanowire (NW).

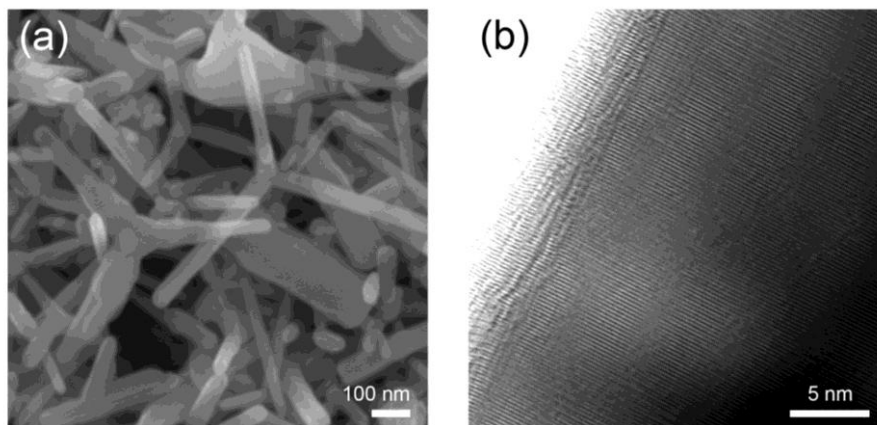


Fig. 4-1. (a) The top-view FESEM images of the T-ZnO NPs after screen-printing on FTO glass, (b) the FETEM image of T-ZnO pod.

Figure 4-2 shows the  $\theta$ -2 $\theta$  X-ray diffraction pattern of T-ZnO NPs that the spacing values and relative intensities of the peak coincide with the JCPDS card no. 36-1451

for ZnO powder and corresponds to the presence of hexagonal wurzite crystallite with cell constants of  $a = 3.2 \text{ \AA}$  and  $c = 5.2 \text{ \AA}$ . No excess peaks were detected, which indicates that the impurity is very low to be detected.

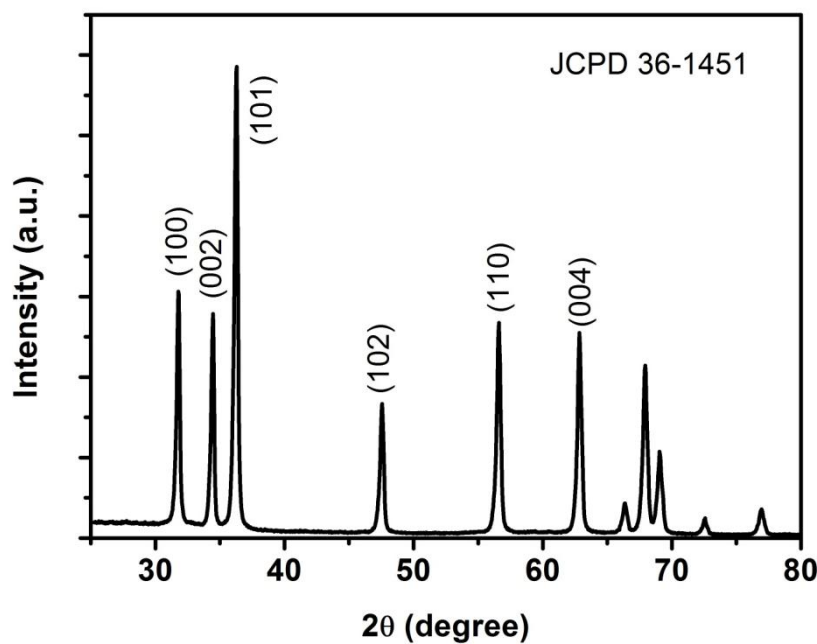


Fig. 4-2. XRD patterns of the tetrapod-like ZnO NPs.

After high temperature necking, the electrons can travel from one tetrapod unit to the neighborhood unit via the interface electron hopping mechanism as the DSC with the photoanode made of NPs so that the electron diffusion driving force in the porous film only depends on the film thickness  $L$ . [70, 71] Thus, the high crystalline ZnO pods can improve the electron transport in the porous network. On the other hand, the electrolyte material is filled in the pore of the photoanode that affects the diffusion of the  $I_3^- / I^-$  couples in the electrolyte.

In order to realize the diffusion dynamics of  $I_3^-/I^-$  couples in the electrolyte, two kinds of ZnO PEs were made by commercial ZnO (called C-ZnO) and tetrapod-like ZnO (T-ZnO) nanoparticles (NPs). Their cross-section SEM images of an assembly of the films on FTO/glass are shown in Fig. 4-3. Highly porous nanostructure can be observed in both of these 26 $\mu\text{m}$  thick PEs. The surface areas of the C-ZnO and T-ZnO NPs are about 18.03 and 15.72  $\text{m}^2\text{g}^{-1}$ , respectively. However, the porous network that constructed by the T-ZnO provides not only an efficient electron diffusion path [39] in the photoanode but also a larger pore size to that made of C-ZnO nanopowders due to the special shape of tetrapod-like morphology.

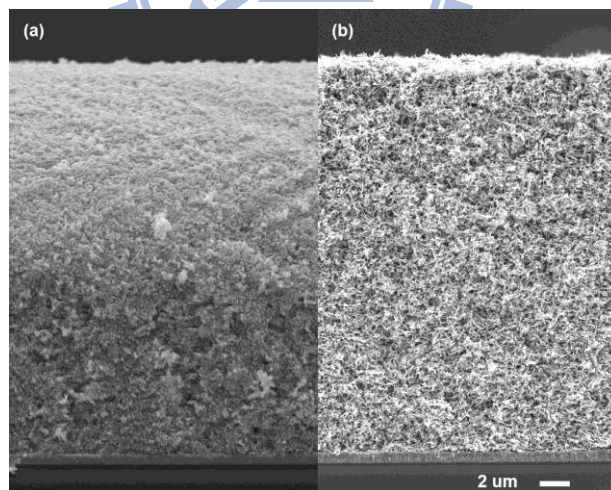
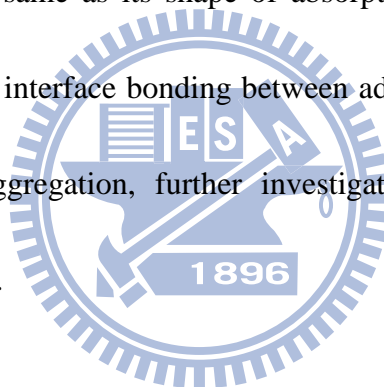


Fig. 4-3. SEM cross-section image of screen-printed ZnO film on FTO/glass. (a) C-ZnO (b) T-ZnO. Scale bar: 2  $\mu\text{m}$ .

Figure 4-4 shows the photoluminescence (PL) spectra of D149 on ZnO and light absorption spectra D149 in acetonitrile at the concentration of 0.015 mM, respectively.

The absorption spectra of D149 in solution consist of two branches. The 388 nm peak is ascribed to a mixture of intramolecular charge transfer (ICT) and the  $\pi-\pi^*$  excitation from the HOMO to the LUMO + 1, on the other hand, the main absorption peak, located at 530 nm, is ascribed to an ICT transition from the HOMO to the LUMO. [72, 73] The molar coefficient of D149 is  $68\,700\text{ M}^{-1}\text{ cm}^{-1}$  at 526 nm [15] that is almost five times larger than the ruthenium dye N719 ( $13\,900\text{ M}^{-1}\text{ cm}^{-1}$  at 541 nm). The broad PL peak centered around 680 nm. The shape of PL spectra is usually symmetry and the same as its shape of absorption spectra. But the detail here is complex due to the interface bonding between adsorbed D149 dye molecules and ZnO and the dye aggregation, further investigations are needed for better understanding its dynamics.





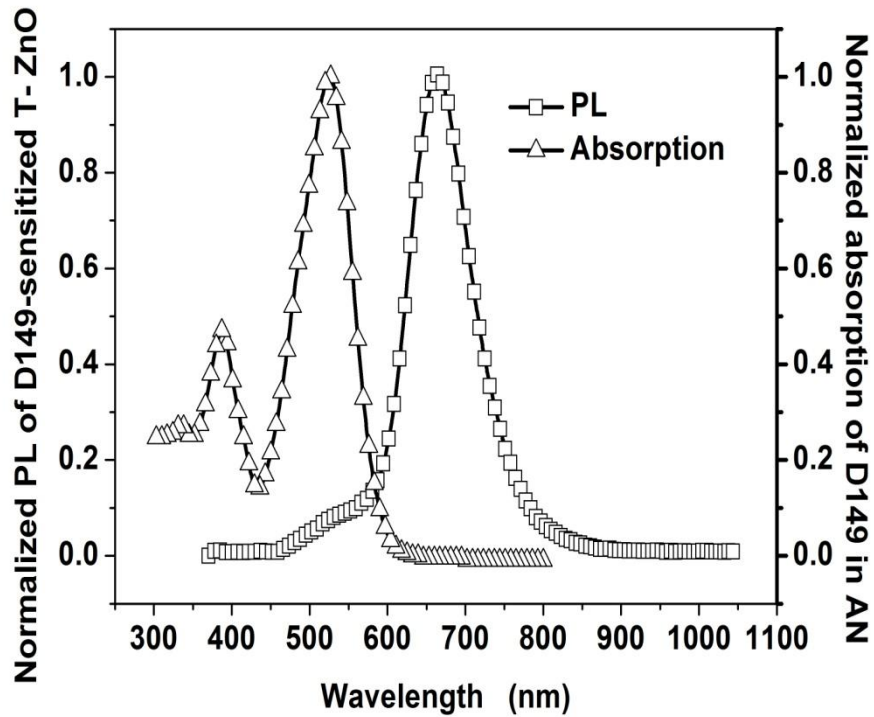


Fig. 4-4. Optical properties of D149. The photoluminescence was optically excited with 430nm laser.

## 4.2 Sintering effect

Table 4-1 shows the PV performance of DSC with T-ZnO electrode (~ 20 μm thickness) sintering at different temperatures. From the Table, it is observed that the PV characteristics of device with non-sintering process are not too low comparing to previous experience for traditional TiO<sub>2</sub> DSC. Similar results with no need for calcination are also reported by Prof. Yang's group. [74] However, when the sintering temperature increases, the PV performance of DSCs is improved, especially for the short circuit current density ( $J_{SC}$ ). Until the sintering temperature arrived 500 °C, the open circuit voltage ( $V_{OC}$ ) and filling factor (FF) drop instantaneously. So in

the next experiments, the sintering temperature is set at 400 °C.

Table 4-1. Cell performance of the DSC with hierarchical 20  $\mu\text{m}$  T-ZnO photoanode electrode sintered at different temperatures.

Sintering Temperature (°C)	$V_{OC}$ (mV)	$J_{SC}$ ( $\text{mA cm}^{-2}$ )	FF	Efficiency (%)
0	607	7.61	0.693	3.21
150	611	7.74	0.686	3.25
200	610	9.36	0.674	3.84
300	611	10.10	0.666	4.12
400	619	10.61	0.649	4.26
500	602	10.29	0.609	3.78

- 0°C stand for non-sintering process.
- The electrolyte (EL 1) is 0.6 M PMII, 0.05 M  $\text{I}_2$ , and 0.5 M TBP in AN.
- The PV characteristics were measured under one sun irradiation (AM 1.5G, 100  $\text{mW cm}^{-2}$ ).

### 4.3 Optimization of photoanode electrode thickness

In order to improve the DSCs' performance, it is important to optimize the thickness of the porous photoanode layer, because the photovoltaic characteristics significantly depend on the thickness of the porous photoanode electrode (PE). In this section, the thickness of the tetrapod-like ZnO (T-ZnO) PE were varied from 5  $\mu\text{m}$  to 42.2  $\mu\text{m}$ , and the photovoltaic characteristics of the DSCs' performance can be seen in

Fig. 4-5.

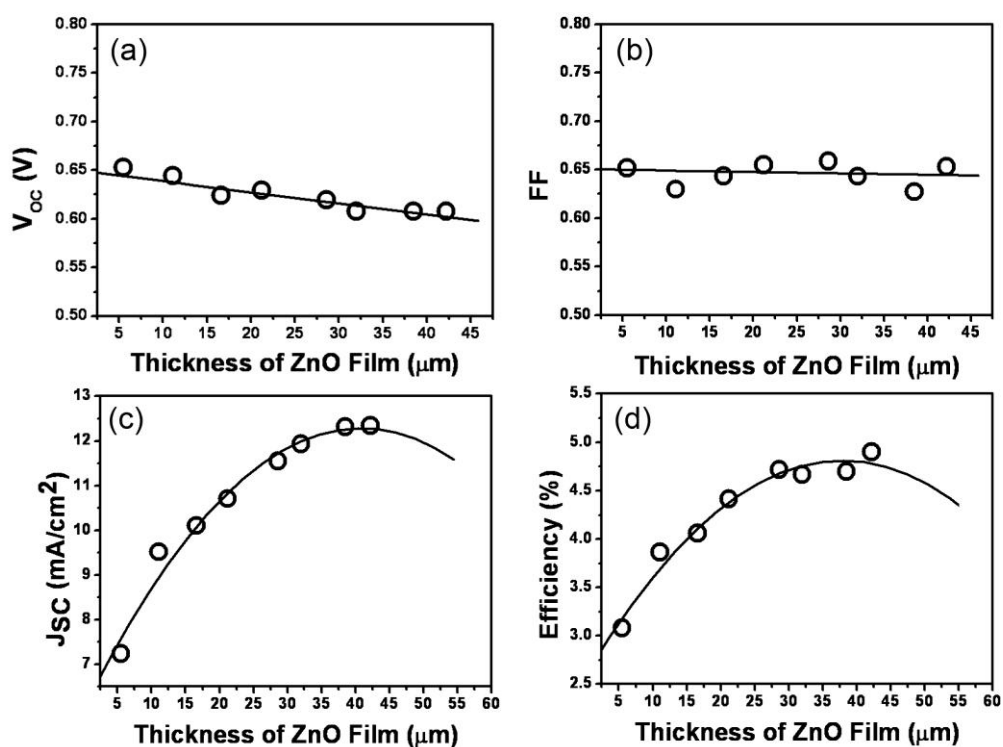


Fig. 4-5. Thickness dependent photovoltaic characteristics of the T-ZnO DSCs with D149 dye. (a) Open-circuit photovoltage,  $V_{oc}$ , (b) Fill factor, FF, (c) Short-circuit photocurrent density,  $J_{sc}$ , and (d) Energy conversion efficiency,  $\eta$ . A strong correlation of  $J_{sc}$  and  $\eta$  is found. The lines are plotted to guide the eyes. The electrolyte is EL 1 (0.6 M PMII, 0.05 M I<sub>2</sub>, and 0.5 M TBP in AN). The PV characteristics were measured under one sun irradiation (AM 1.5G, 100  $\text{mW cm}^{-2}$ ).

First, the open-circuit voltage ( $V_{oc}$ ) decreases linearly with the increase of ZnO film thickness. The  $V_{oc}$  is the difference of the electron Fermi levels of the PE and the electrolyte, so the behavior of  $V_{oc}$  is suggested by an inhomogeneous density of the light in the porous ZnO film to contribute an inhomogeneous electron Fermi level of photoanode. In Fig. 4-5(b), the filling factor (FF) keeps almost a constant of 0.65 with increasing the ZnO film thickness to 42.2  $\mu\text{m}$ . On the other hand, the series resistance of the cell, which includes the resistance of FTO, PE, electrolyte, and Pt counter

electrode (CE), may not change too much with the thickness of PE due to the low resistance of the high crystalline ZnO tetrapod network. And it also indicates that the T-ZnO network exhibits efficient electron transport for such thick ZnO PEs. The  $J_{sc}$  is increasing with the thickness of T-ZnO film in contrast with the  $V_{oc}$ , because a greater photoanode surface area with thicker film is obtained to enhance the dye loading and the current. However, the  $J_{sc}$  does not increase linearly with the increase of ZnO film thickness because the larger surface area of the PE also has more recombination sites. The maximal  $J_{sc}$  is obtained presently with 42.2  $\mu\text{m}$  thick film from Fig. 4-5(c). It is therefore important to note that the optimization of PE thickness by using T-ZnO is about twice as thick as that by using ZnO nanosheet structure photoanode. [34] Finally, the energy conversion efficiency of the solar cells can be calculated by

$$\eta = \frac{V_{oc} J_{sc} FF}{P_{in}} \quad (4-1)$$

where  $P_{in}$  is the optical power of 100  $\text{mW cm}^{-2}$  under AM 1.5G.

From the above results, the magnitude of the variation of both  $V_{oc}$  and FF is smaller than that of  $J_{sc}$ . Therefore, the energy conversion efficiency ( $\eta$ ) is dominated by  $J_{sc}$  as shown in Fig. 4-5(d). The energy conversion efficiency has a peak value of 4.9% for our 42.2  $\mu\text{m}$  thick DSC. From the above results, the 42.2  $\mu\text{m}$  tetrapod-like ZnO dye-sensitized solar cell with D149 and CDCA absorption shows a good photovoltaic performance and the photocurrent–voltage (J–V) curve is shown in Fig. 4-6(a). The

photovoltaic characteristics are comparable to the previous literature [34] with  $J_{sc}$ ,  $V_{oc}$ , FF, and the efficiency being  $12.4 \text{ mA cm}^{-2}$ , 607 mV, 0.65, and 4.9%, respectively. The high photocurrent density is attributed to the good electron transport in ZnO porous network and the high absorption coefficient of the D149 dye. The absorbance of D149 in acetonitrile (open circles) shown in Fig. 4-6(b) revealing peaks at 526 and 388 nm. Here, the IPCE for the cells with D149 and CDCA absorption (open squares) reaches more than 60% in the spectral range from 490 nm to 600 nm that is contributed from the D149 absorption peak of 526 nm; whereas, the absorption peak of D149 at 388 nm contributes more than 40% to IPCE in the range from 390 nm to 450 nm. The IPCE spectra of D149 dye and CDCA adsorbed on ZnO film (after 400 nm) is similar to pure D149 absorption spectra in solution but exhibits a red shift and peak broadening due to the interaction of the anchoring carboxyl group to the ZnO surface, and the results indicate that the excited electron can transport efficiently through the porous ZnO network and a large photocurrent is also obtained. On the other hand, the other IPCE peak around 370 nm mainly results from the exciton absorption of the ZnO photoanode, because the IPCE of the cells without absorption dye (open triangles) reveals almost the same peak.

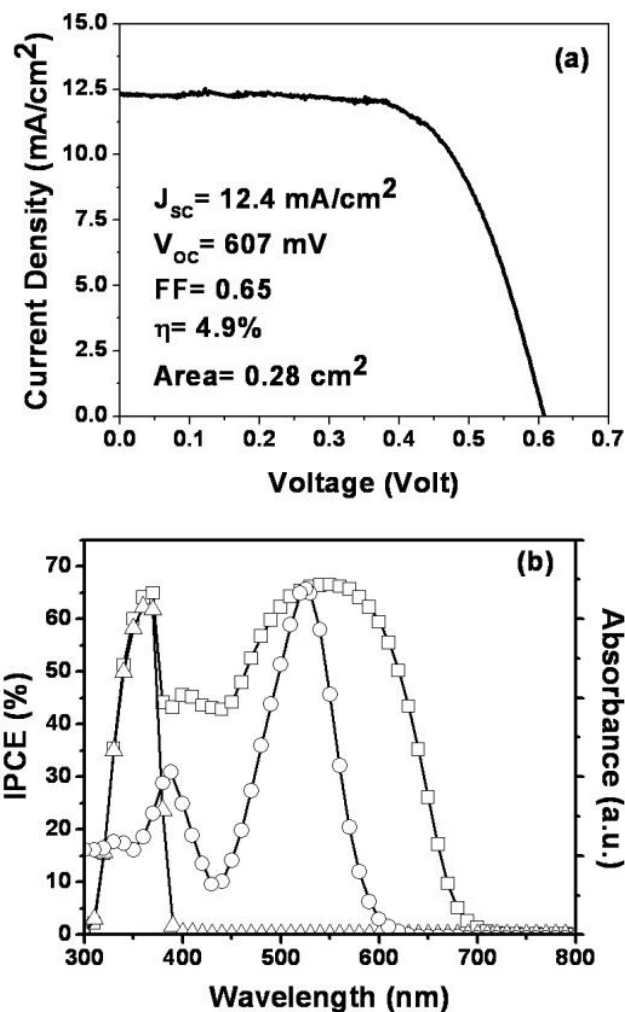


Fig. 4-6. (a) J-V curve obtained with DSCs based on D149 and CDCA absorption under AM 1.5 radiation ( $100 \text{ mW/cm}^2$ ). (b) Absorption spectra of D149 in AN ( $-\circ-$ ) and the IPCE spectra for  $42 \text{ }\mu\text{m}$  T-ZnO DSCs with D149 and CDCA absorption ( $-\square-$ ) and without any absorption ( $-\Delta-$ ). The electrolyte (EL 1) was a mixture of  $0.5 \text{ M PMII}$ ,  $0.03 \text{ M I}_2$ , and  $0.5 \text{ M TBP}$  in AN.

## 4.4 Efficient electron transporting in tetrapod-like ZnO photoanode

In this section, the EIS measurement is also employed to analyze the performance of the tetrapod porous network photoanode, and the Nyquist Cole–Cole plot of the  $42.2 \text{ }\mu\text{m}$  tetrapod-like ZnO (T-ZnO) DSC is shown in Fig. 4-9. The effective electron transporting coefficient ( $D_{\text{eff}}$ ) of  $42.2 \text{ }\mu\text{m}$  T-ZnO DSC is  $1.533 \times 10^{-3} \text{ cm}^2 \text{ sec}^{-1}$  which is

much larger than that of traditional TiO<sub>2</sub>-based DSCs (about 10<sup>-5</sup> cm<sup>2</sup> sec<sup>-1</sup>).[75] And the effective electron diffusion length for the 42.2 μm T-ZnO DSC is estimated by the relation:  $L_n = (D_{eff} \times \tau_n)$ , to be 45.57 μm. It means the optimal thickness of photoanode is around 46 μm that is consistent with the results of thickness dependent J<sub>SC</sub> measurement discussed in last section. The series resistance (R<sub>Stot</sub>) estimated from EIS fitting is 30.2 Ω via the well-known relation (Eq. 4-3) [76] indicating consistent with 28.9 Ω calculated from the I-V curve of Fig. 4-6 (a).

$$R_{Stot} = R_S + R_{Pt} + R_{TCO1} + \frac{1}{3}R_W + R_K + R_D \quad (\text{Eq. 4-2})$$

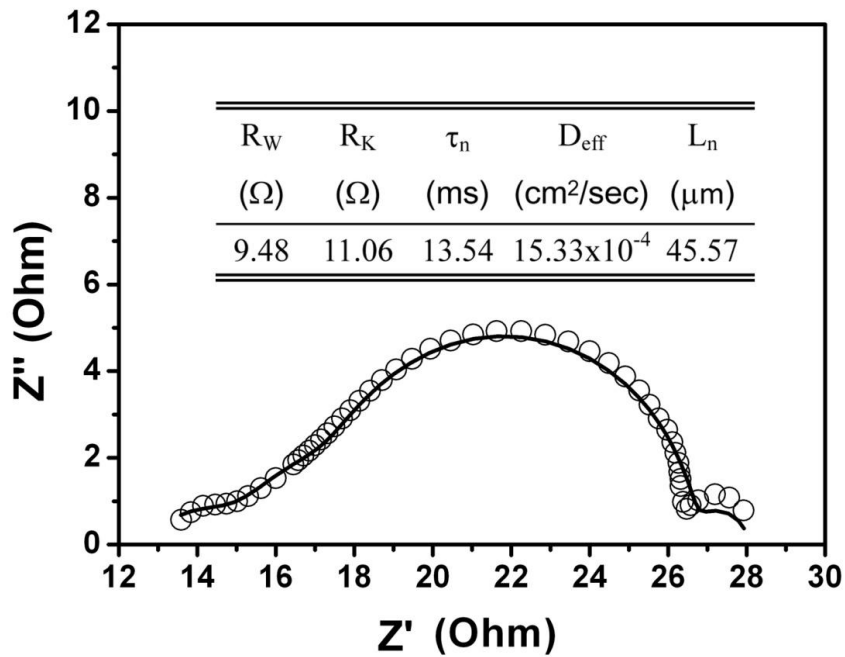


Fig. 4-7. Nyquist plot of the 42.2 μm tetrapod-like DSCs sensitized by Di49 dye. The empty circles in are the measurement data points, and the solid curve is the fitting result based on the equivalent circuit model as shown in Fig 2-7. The data was collect by applying a bias of the open circuit voltage (V<sub>OC</sub>) under solar simulator (AM 1.5G, 100 mW cm<sup>-2</sup>). The electrolyte (EL 1) of the device was a mixture of 0.5 M PMII, 0.03 M I<sub>2</sub>, and 0.5 M TBP in AN.

## 4-5 Influence of photoanode thickness on the photovoltaic performance of ionic liquid device

In order to obtain the high performance DSCs, the thickness of T-ZnO photoanode were varied deposited to 42  $\mu\text{m}$  in pervious section. Under one sun irradiation, the results of photovoltaic characteristics with filling AN-based and IL-based electrolytes by varying different PE thickness are shown in Fig. 4-8. AN-based electrolyte (EL 1) is a mixture of 0.5 M PMII, 0.03 M  $\text{I}_2$ , and 0.5 M TBP in AN. IL-based electrolyte (EL 2) is composed by 0.2 M  $\text{I}_2$ , 0.5M TBP in PMII/ $\text{C}_8\text{MImPF}_6$  mixture (v/v=35:65). Figure 4-8(a) gives the open-circuit voltage ( $V_{\text{OC}}$ ) results for DSCs with two types of electrolytes, the  $V_{\text{OC}}$  of both types decrease linearly with the increase of ZnO film thickness. The inhomogeneous light density through the porous ZnO films contributes an inhomogeneous quasi-Fermi level of photoanode. A 200mV  $V_{\text{OC}}$  drops in IL-based DSCs relative to that of AN-based for the same thickness is due to the higher  $\text{I}_2$  concentration in IL-based DSCs, and can be explained by charge recombination model [55] between photoanode and the  $\text{I}_3^- / \text{I}^-$  couples in electrolyte with the following equation,

$$V_{\text{OC}} = \left[ \frac{kT}{q} \right] \ln \left[ \frac{I_{\text{inj}}}{n_{\text{cb}} k_{\text{et}} [\text{I}_3^-]} \right], \quad (4-3)$$

where  $k$  is Boltzmann constant,  $T$  is the absolute temperature,  $q$  is the electronic elementary charge,  $I_{\text{inj}}$  is the flux of charge from sensitized dyes,  $n_{\text{cb}}$  is electron



concentration in the ZnO,  $k_{et}$  is the reaction rate constant of the dark current from ZnO to tri-iodide ions in the electrolyte, and  $[I_3^-]$  is the concentration of tri-iodide ions in the electrolyte. The behaviors of the short-circuit photocurrent ( $J_{SC}$ ) are illustrated in Fig. 4-8(b).  $J_{SC}$  of AN-based DSCs increases continuously with film thickness, and reaches a maximum value of  $11.4 \text{ mA cm}^{-2}$  at thickness of  $26 \mu\text{m}$ . In contrast,  $J_{SC}$  of IL-based DSCs has a plateau value close to  $5 \text{ mA cm}^{-2}$  in the device whose thickness is about  $18 \mu\text{m}$ .

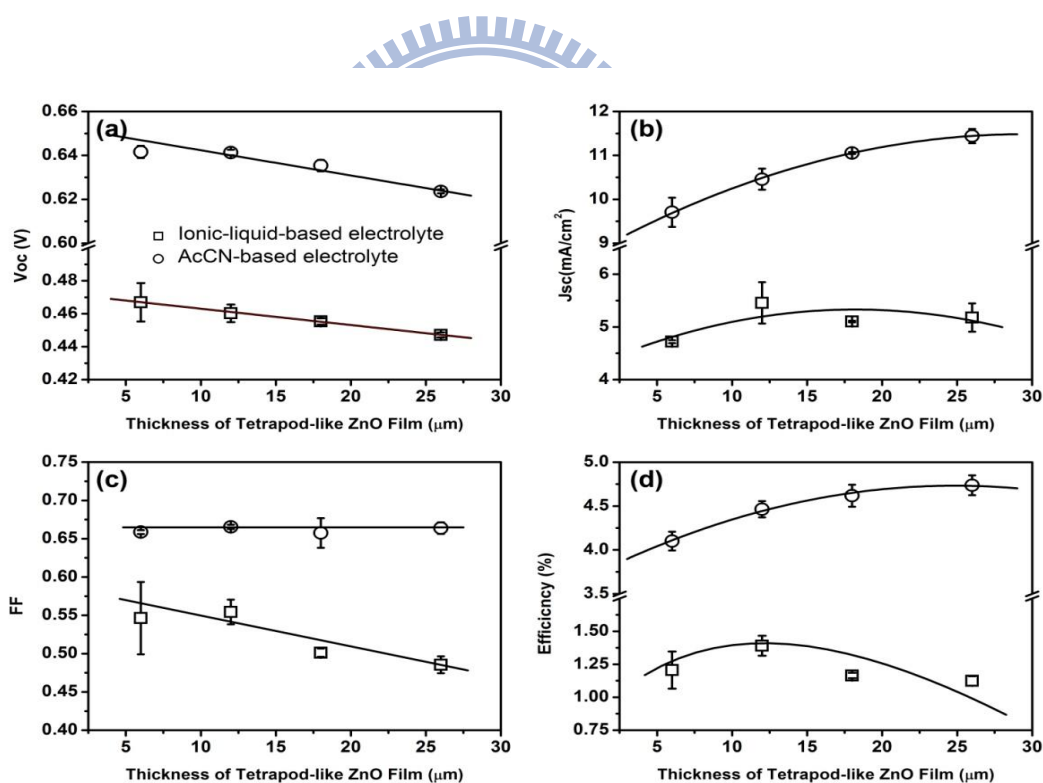


Fig. 4-8. Dependences of cell performances on film thickness including (a) open-circuit voltage ( $V_{OC}$ ), (b) short-circuit photocurrent density ( $J_{SC}$ ), (c) filling factor (FF), and (d) solar conversion efficiency.

The open-circle and open-square symbols correspond to the DSCs filling by AN-based and IL-based electrolytes, respectively. The lines are plotted to guide the eyes, and the error bars from the data of two devices are also shown in the figures. AN-based electrolyte (EL 1) is a mixture of 0.5 M PMII, 0.03 M  $I_2$ , and 0.5 M TBP in AN. IL-based electrolyte (EL 2) is composed by 0.2 M  $I_2$ , 0.5M TBP in PMII/ $C_8\text{MImPF}_6$  mixture (v/v=35:65). All data was obtained under one sun irradiation.

The FF remains a constant for the AN-based DSCs, while the IL-based DSCs show a prominent decline in FF with increasing film thickness. The different behavior observed in  $J_{SC}$  and FF results from the higher viscosity of the ionic liquid that limits the mass-transport of the  $I_3^-/I^-$  couples in electrolyte and increases the resistance of the electrolyte. The maximal conversion efficiency of the AN-based and IL-based DSCs, which can be calculated by  $\eta = J_{SC} \times V_{OC} \times FF$  under one sun irradiation, are 4.73% and 1.39% for 26  $\mu\text{m}$  and 12  $\mu\text{m}$  thick T-ZnO, respectively. Therefore, in the IL-based DSCs, the thickness of the photoanode isn't the strongest influence factor to optimize the device; on the contrary, the characteristics of the ionic liquid and the morphology of the photoanode should be paid more attention to.

To realize the differences between the T-ZnO framework as the PE and the conventional PE made of spherical C-ZnO nanopowders, the J-V curves of these two DSC devices are shown in Fig. 4-9 (a). The photovoltaic parameters obtained with AN-based DSCs using 26  $\mu\text{m}$  T-ZnO photoanode (open square symbol) are  $V_{OC}=0.622\text{V}$ ,  $J_{SC}=11.55 \text{ mA cm}^{-2}$ ,  $FF=0.67$ , and  $\eta=4.81\%$ . In IL-based DSCs, however, the lower performances are obtained, in which the photovoltaic parameters of 26  $\mu\text{m}$  T-ZnO DSCs (open triangle symbol) are  $V_{OC}=0.448\text{V}$ ,  $J_{SC}=5.37 \text{ mA cm}^{-2}$ ,  $FF=0.48$ , and  $\eta=1.15\%$ . And those of 26  $\mu\text{m}$  C-ZnO DSCs (solid triangle symbol) are  $V_{OC}=0.444\text{V}$ ,  $J_{SC}=3.95 \text{ mA cm}^{-2}$ ,  $FF=0.49$ , and  $\eta=0.87\%$ . The high photocurrent of

11.55 mA cm<sup>-2</sup> are attributed to the high absorption coefficient of D149 in AN-based system, but the photocurrent in IL-based system (triangle symbol) reduces to less than a half of that in AN-based system (square symbol). It is believed that the higher viscosity of the IL-based electrolyte leads to the ionic-transport limitation of the photocurrent. On the other hand, the photocurrent of IL-based DSCs using T-ZnO photoanode is almost 1.3 times larger than that using C-ZnO photoanode, due to the larger pore size in the tetrapod-like framework provides an efficient ionic diffusion pathway to improve the ionic-transport limitation. Moreover, the IPCE spectra provides a conversion efficiency measurement of wavelength-dependent photons that incident on the DSCs to photocurrent flowing between the photoanode and counter electrodes. The IPCE spectra of these devices are shown in Fig. 4-9(b). High IPCE are obtained with T-ZnO DSCs filled with AN-based electrolyte; the peak values are observed at about 550 nm and 390 nm, which are contributed from the absorption peak of D149 dye and the absorption of ZnO, respectively. Although D149 has a strong green light absorption (68700 Mol<sup>-1</sup> cm<sup>-1</sup> at 526 nm), the plateau IPCE value about 30% is observed from 500 nm to 600 nm in T-ZnO DSCs filled with IL-based electrolyte. It results in the slow ionic diffusion in the high velocity IL electrolyte that slows down the oxidation-reduction reaction of the dye molecule. Furthermore, the IPCE reduction of all spectral range is also observed. Additionally, almost 4 times IPCE decreasing from

400 to 450 nm between two electrolyte systems is also due to the light absorption of higher iodine concentration in the IL-based system [77].  $J_{SC}$  agrees with the value integrated by IPCE spectrum with standard AM 1.5G sunlight, the reasons from IPCE can explain the  $J_{SC}$  difference of 26  $\mu\text{m}$ -thick DSCs between AN-based and IL-based electrolytes.

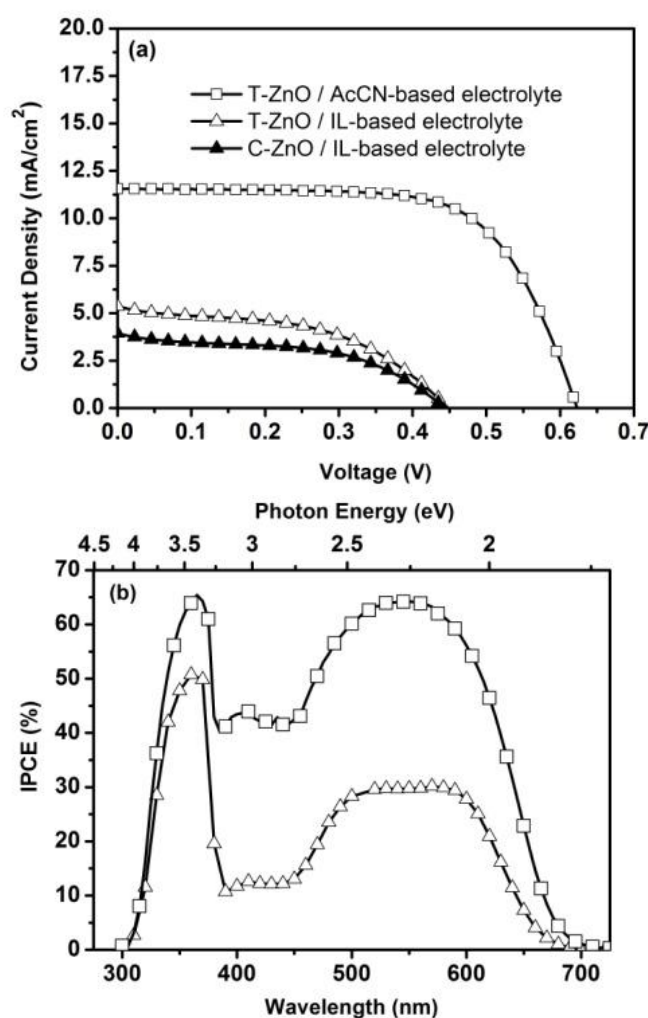


Fig. 4-9. Cell performances of AN-based (square symbol) and IL-based (triangle symbol) DSCs based on 26 $\mu\text{m}$ -thick ZnO nanostructure photoanodes that were constructed by commercial (solid symbol, C-ZnO) and tetrapod-like (open symbol, T-ZnO) ZnO powders. (a) The J-V curve of these DSC devices (100  $\text{mWcm}^{-2}$ , AM 1.5G) and (b) The IPCE spectra of these DSC devices. AN-based electrolyte (EL 1) is a mixture of 0.5 M PMII, 0.03 M I<sub>2</sub>, and 0.5 M TBP in AN. IL-based electrolyte (EL 2) is composed by 0.2 M I<sub>2</sub>, 0.5M TBP in PMII/C<sub>8</sub>MImPF<sub>6</sub> mixture (v/v=35:65).

## 4.5 Ionic diffusion dynamics of ionic-liquid electrolyte

### Photocurrent transient measurement

In order to understand the ionic-transport mechanism, the time-response photocurrent transients are carried out. Figure 4-10(a) is the plot of the time-response photocurrent for a 12  $\mu\text{m}$  thick T-ZnO DSCs filled with IL-based electrolyte exposed under different sun light intensity with an on-off irradiation shutter. At the beginning of the shutter opening, the higher photocurrent is obtained because there are enough  $I^-$  ions to provide the oxidation-reduction reaction of the dye molecule. As the time goes, the  $I^-$  ions around the dye molecules diminish due to the slow diffusion of the  $I_3^-/I^-$  couples, so that the photocurrent decreases continuously in a few seconds. Finally, the photocurrent comes to an equilibrium value, which depends on the ionic-diffusion ability of the ionic liquid electrolyte. As lowering the light intensity, the reduction ratio of the photocurrent is also decreasing because the lower the sunlight exposure on the device, the less  $I^-$  ions are needed to regenerate the excited dye molecule. So even in the viscous ionic liquid electrolyte with slow ionic-diffusion, and the diffusion of  $I_3^-/I^-$  ions to and from the counter electrode is already fast enough to provide sufficient enough redox agents that regenerate the excited dye molecules. Figure 4-10(b) shows the ratio of the final to initial photocurrent as functions of film thickness and sunlight intensity. For the IL-based DSCs with T-ZnO

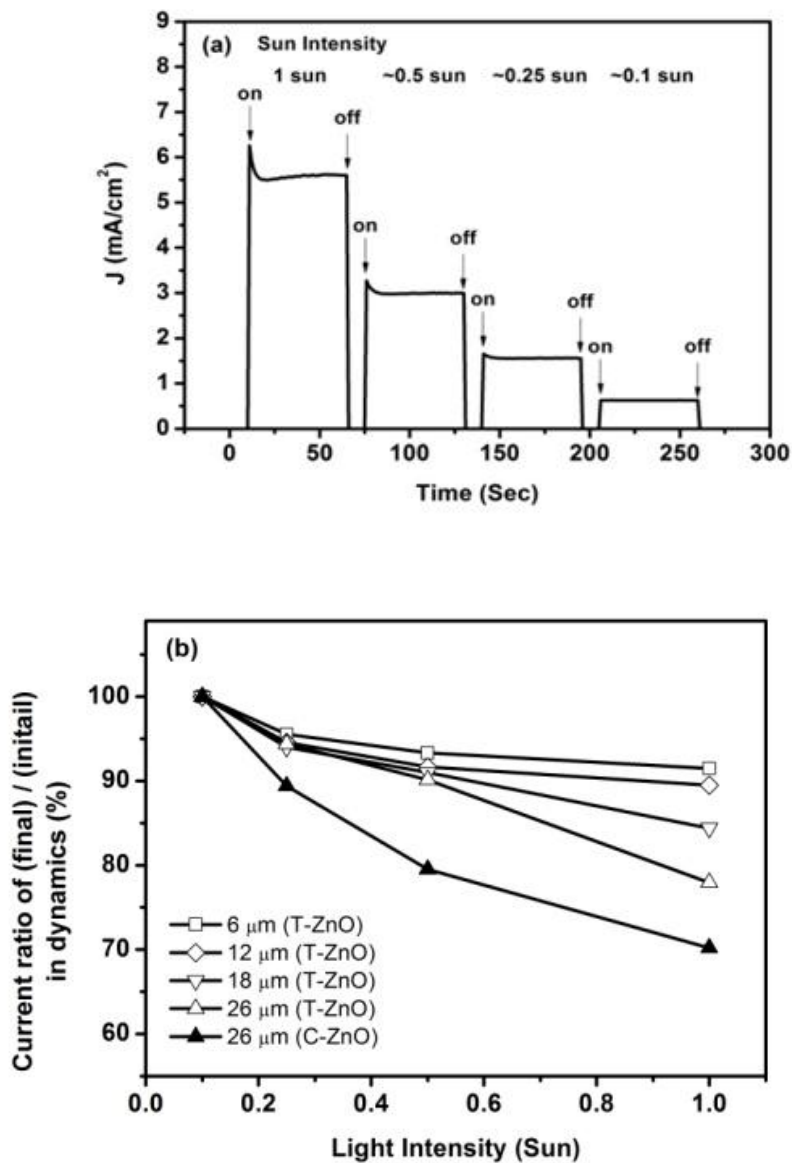


Fig. 4-10. The photocurrent transient dynamics of IL-based D149-sensitized solar cells. (a) Photocurrent dynamics obtained with the IL-based DSC device for 12 $\mu\text{m}$ -thick tetrapod-like ZnO (T-ZnO) photoanode; (b) Ratio of the final to the initial value of the photocurrent as a function of sun intensity for two types of 26 $\mu\text{m}$  photoanodes. Open symbol represents photoanode using T-ZnO powders and solid one represents commercial ZnO (C-ZnO) powders. AN-based electrolyte (EL 1) is a mixture of 0.5 M PMII, 0.03 M I<sub>2</sub>, and 0.5 M TBP in AN. IL-based electrolyte (EL 2) is composed by 0.2 M I<sub>2</sub>, 0.5M TBP in PMII/C<sub>8</sub>MImPF<sub>6</sub> mixture (v/v=35:65).

and the sunlight intensity. In the DSCs of thicker photoanode, the longer effective ionic-transport pathway is obtained, so the role of the ionic diffusion is also more

important. Moreover, the comparison of the DSCs using 26  $\mu\text{m}$  thick T-ZnO and C-ZnO photoanodes clarifies that the efficient ion-transport pathway of the self-assemble photoanode by T-ZnO improves the ionic diffusion, then the higher short-circuit photocurrent of T-ZnO DSCs is achieved.

### EIS analysis

The electrical impedance spectroscopy (EIS) is one of the useful methods to explore the characteristics of each component in DSC devices; in particular, the parameters about the photoanode electrode and the electrolyte will be discussed here. In this study, the equivalent electric circuit model [39, 66] is shown and discussed in Chapter 2. In this model,  $Z_N$  symbolizes the Warburg diffusion impedance, and can be described by the following equation [67],

$$Z_N = \frac{R_D}{\sqrt{j\omega/W_{sc}}} \tanh[\sqrt{j\omega/W_{sc}}], \quad (\text{Eq. 4-4})$$

where  $R_D$  is the dc resistance of impedance of diffusion of tri-iodide,  $W_{sc} = D \times d^{-2}$ ,  $d$  is the Nernst diffusion layer thickness, and  $D$  is the diffusion coefficient of  $I_3^-$ .

Figure 4-11(a) shows the EIS Nyquist plots of the IL-based DSC devices with 26 $\mu\text{m}$  C-ZnO photoanode and different thicknesses of T-ZnO photoanodes under one sun irradiation (AM 1.5G). The corresponding Bode plots are also shown in the inset of this figure. The related fitting parameters with related photovoltaic performances

are listed in Table 4-2. Generally, all of the DSCs exhibit three semicircles, which are commonly assigned to the electrochemical reaction of Pt counter electrode, ZnO photoanode, and Warburg diffusion process of the electrolyte from high to low frequency, respectively.

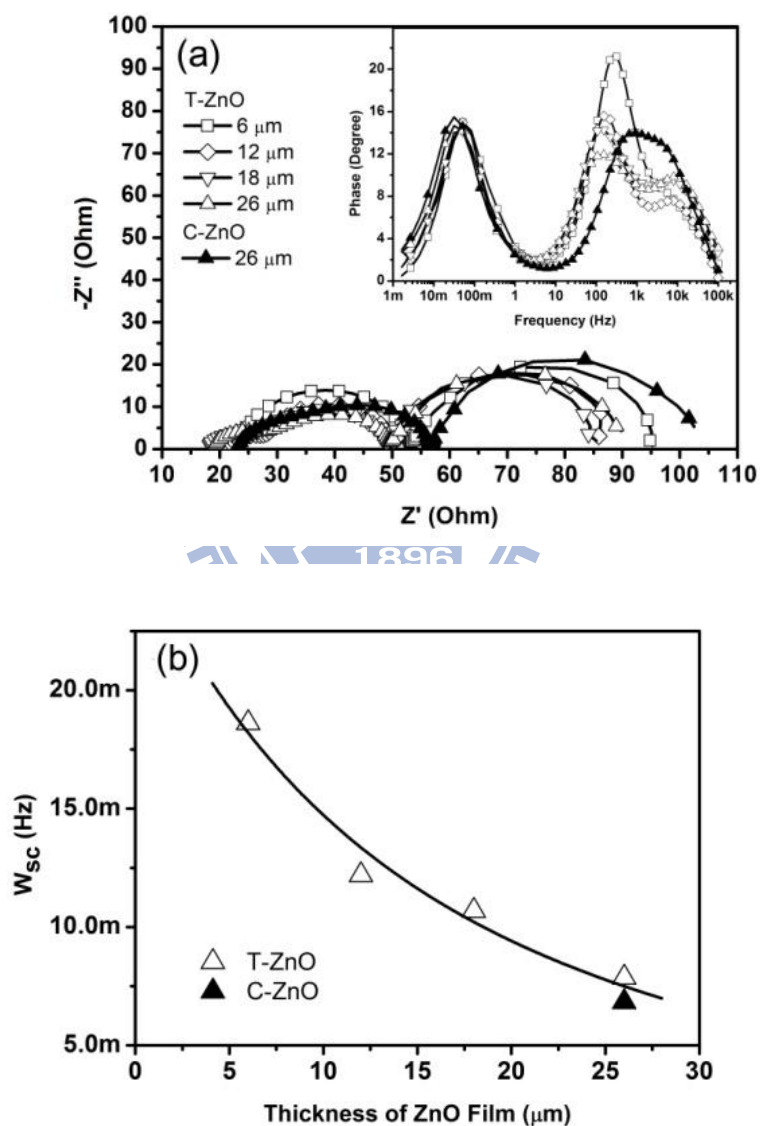


Fig. 4-11. The electrical characteristics of the IL-based D149-sensitized solar cells. (a) Cole-Cole plots for DSCs employed by commercial ZnO (C-ZnO) photoanode and different thicknesses of tetrapod-like ZnO (T-ZnO) photoanodes. The inset shows the corresponding Bode plots. The equivalent circuit model used to analyze the experimental data is in Fig 2-7. The electrolyte (EL 2) is composed by 0.2 M  $\text{I}_2$ , 0.5M TBP in PMII/ $\text{C}_8\text{MImPF}_6$  mixture (v/v=35:65). (b) Plot of  $W_{sc}$  and the DSC devices with various ZnO photoanodes, and the solid line is the fitting curve of T-ZnO DSCs.



Figure 4-11(b) shows  $W_{sc}$  for the DSCs by using 26  $\mu\text{m}$  C-ZnO photoanode and different thicknesses of T-ZnO photoanodes. Given a  $x$ - $\mu\text{m}$  thick photoanode provides  $ax$   $\mu\text{m}$  of effective Nernst diffusion layer in the framework pore, so the total Nernst diffusion layer in the DSCs with 30  $\mu\text{m}$  spacer may be described as  $d = a \times (30 - x)$   $\mu\text{m}$ , and the related parameters are obtained through well fitting to data by  $W_{sc} = D \times [ax + (30 - x)]^{-2}$ . For the T-ZnO DSCs, the effective thickness multiply factor  $a$  is 2.0, and the diffusion coefficient of the electrolyte ( $D$ ) is about  $2.3 \times 10^{-7} \text{cm}^2 \text{s}^{-1}$ . Moreover, the effective thickness multiply factor in DSCs for 26  $\mu\text{m}$  thick C-ZnO photoanode is estimated to 2.1, based on the same diffusion coefficient of the electrolyte. There is no doubt that the length of the ionic diffusion pathway is one of the influence factors to affect the performance of IL-based DSCs. Comparing to these 26  $\mu\text{m}$  thick DSCs, the difference of these ionic diffusion pathways is only 5%, but the corresponding photovoltaic performance is not only 5%. So it is believed that the continuous ionic diffusion pathway assembled spontaneously by the T-ZnO provides a more efficient ionic diffusion loop than that made of C-ZnO nanopowders in conventional DSCs, due to the different pore size of these devices.

Table 4-2. Photovoltaic performance of IL-based DSCs and corresponding properties of photoanode determined by electrochemical impedance spectroscopy (EIS) under full sunlight irradiation.

ZnO material	Thickness ( $\mu\text{m}$ )	$V_{OC}$ (mV)	$J_{SC}$ ( $\text{mAcm}^{-2}$ )	FF	$\eta$ (%)	$R_W$ ( $\Omega$ )	$R_K$ ( $\Omega$ )	$k_{eff}$ (Hz)	$D_{eff}$ ( $\text{cm}^2\text{s}^{-1}$ )
T-ZnO	6	475	4.73	0.58	1.30	12.3	30.9	269.1	$2.1 \times 10^{-4}$
T-ZnO	12	464	5.73	0.54	1.44	9.1	23.6	132.7	$4.9 \times 10^{-4}$
T-ZnO	18	456	5.11	0.50	1.17	27.1	24.1	79.6	$2.1 \times 10^{-4}$
T-ZnO	26	448	5.37	0.48	1.15	48.8	11.9	51.4	$8.4 \times 10^{-5}$
C-ZnO	26	444	3.95	0.49	0.87	77.5	7.2	57.8	$3.6 \times 10^{-5}$

a. IL-based electrolyte (EL 2) is composed by 0.2 M  $I_2$ , 0.5M TBP in PMII/C8MImPF6 mixture (v/v=35:65).

In addition, the effective rate constant for recombination ( $k_{eff}$ ) varies inversely with the thickness of the tetrapod-like DSCs, which is listed in Table 4-2. The effective rate constant for recombination is generally identified to the recombination rate of electrons in the photoanode and  $I_3^-$  ions in the electrolyte, which is so-called back-recombination rate. The possible interpretation of this behavior is that the thicker photoanode not only provides larger area with more recombination sites on it but also decreases the volume of the electrolyte and the mole number of  $I_3^-$  at the equilibrium state. Finally, in Table 4-2, the effective electron diffusion coefficients in photoanode are also estimated by the relation equation [67],  $D_p = (R_K / R_W) L^2 k_s$ , where L stands for the thickness of the photoanode, and are also consistent to the  $J_{SC}$  of the DSCs performance shown in Fig. 4-8.

## 4.6 Summary

The electron collection is one of the most important issues to make a high efficiency cell. Here, a trade-off solution to optimize the electron transport properties and the photoanode surface area is given, and the high energy efficient ZnO-based DSCs with efficient electron collection is also demonstrated. By using the tetrapod-like ZnO porous network as the photoanode the D149 dye-sensitized solar cells are found to exhibit high-performance. The photovoltaic characteristics are greatly affected by the thickness of the tetrapod-like ZnO photoanode, and the optimized thickness of the D149-sensitized tetrapod-like ZnO photoanode is 42.2  $\mu\text{m}$  with conversion efficiencies of 4.9 % at present, due to the good electron transport ability of ZnO tetrapod network. The good electron diffusion properties with  $D_{\text{eff}} = 1.53 \times 10^{-3} \text{ cm}^2 \text{ sec}^{-1}$  and  $L_n = 46 \mu\text{m}$  are also estimated by the electrochemical impedance spectroscopy. On the other hands, the good conductivity tetrapod ZnO photoanode is easy to make mass production with screen-printing method or doctor-blade method, in contrast to the other 1D nanostructure photoanode. And the concept of tetrapod structure powder is also suitable to other semiconductor photoanode in DSCs for future applications.

In DSCs with liquid electrolyte system, the scientists only care about the electron diffusion in the photoanode, and ignore the ionic diffusion ability in electrolyte film. But the ionic diffusion dynamics in IL-based electrolyte cannot be out of consideration,

because poor performance of IL-based DSCs results from the slow ionic diffusion. In this study, the screen-printing photoanode from T-ZnO nanopowders provides an efficient ionic diffusion pathway for ionic liquid electrolyte. So the concept of tetrapod structure powder is also suitable to other semiconductor photoanode in IL-based or gel-type DSCs for future applications, especially in a binder-free system.

In summary, the photovoltaic performances of IL-based DSCs with tetrapod-like framework photoanode are affected by the length of the ionic diffusion pathway in the photoanode, and the best performance of DSCs is obtained with conversion efficiency of 1.44% at present. By using the time-response photocurrent transients and the electrochemical impedance spectrum analysis, the T-ZnO DSCs have a better solar conversion efficiency and larger short-circuit photocurrent than that made of commercial powders, because the tetrapod-like framework provides a suitable structure of efficient ionic diffusion process. It is believed that the T-ZnO nanopowder is one of the feature materials to make solvent-free DSCs, due to not only the efficient electron diffusion in photoanode but also the fast ionic diffusion in the electrolyte film.

# **Chapter 5 Multiple electrophoresis deposited crackless TiO<sub>2</sub> photoanode for flexible DSCs**

The research of dye-sensitized solar cells has concentrated almost exclusively to the glass substrate based technology, which has already been pushed close to commercialization. So the manufacturing methods for the preparation of the nanostructured TiO<sub>2</sub> electrodes onto plastic sheets concentrating should be also simultaneously improved. In screen-printing photoanode calcined at high temperature, organic binder plays a role to avoid the crack of the mesoporous film. However, the melt point of the organic binder (eg. 375 °C for EC) is higher than that of the flexible polymer substrate (eg. 200 °C for PEN). In this chapter, we report a method through multiple electrophoretic deposition (EPD) to make a crackless film, and achieve a high performance dye-sensitized solar cell (DSC). And its long-term stability was also discussed.

## **5.1 Compress effect on photovoltaic performances**

Although the compress treatment has been widely used in producing mesoporous

photoanode electrode of flexible substrate DSCs [78, 79], the correlation between applied pressure and device performance should also be clarified in this work. Therefore, a detailed experimental was performed under different compress pressures condition to obtain the performance of the assembled DSCs devices, and the results are shown in Fig. 5-1. The thickness of electrophoretic deposited TiO<sub>2</sub> film is about 20 μm, and reduces to 6-8 μm via different applied pressures. Between a non-compressed and a 100MPa-pressed TiO<sub>2</sub> films, J<sub>SC</sub> increased rapidly from 1.7 to 11 mA cm<sup>-2</sup>, respectively. J<sub>SC</sub> saturates at about 11 mA cm<sup>-2</sup> until the 500 MPa pressure. It is believed that the high external pressure (over 100MPa) not only melt the surface of TiO<sub>2</sub> nanoparticles (NPs) to form a good porous photoanode for electron transporting, but also increase the adhesion strength between the TiO<sub>2</sub> film and ITO/PEN substrate[78]. The slight changes of V<sub>OC</sub> with different pressure (P) from non-pressed to 500 MPa were not significant but related to the film thickness. The fill factor (FF) was observed almost a constant about 0.7 in the range 0 (non-pressed) to 400 MPa, but FF of the DSCs with 500 MPa pressure dropped to 0.4 due to the crack of the ITO film by the compress jig. Consequently, the 6% overall efficiency with 100 MPa pressure treatment was achieved, and the 100 MPa pressure treatment will use in next experiments.

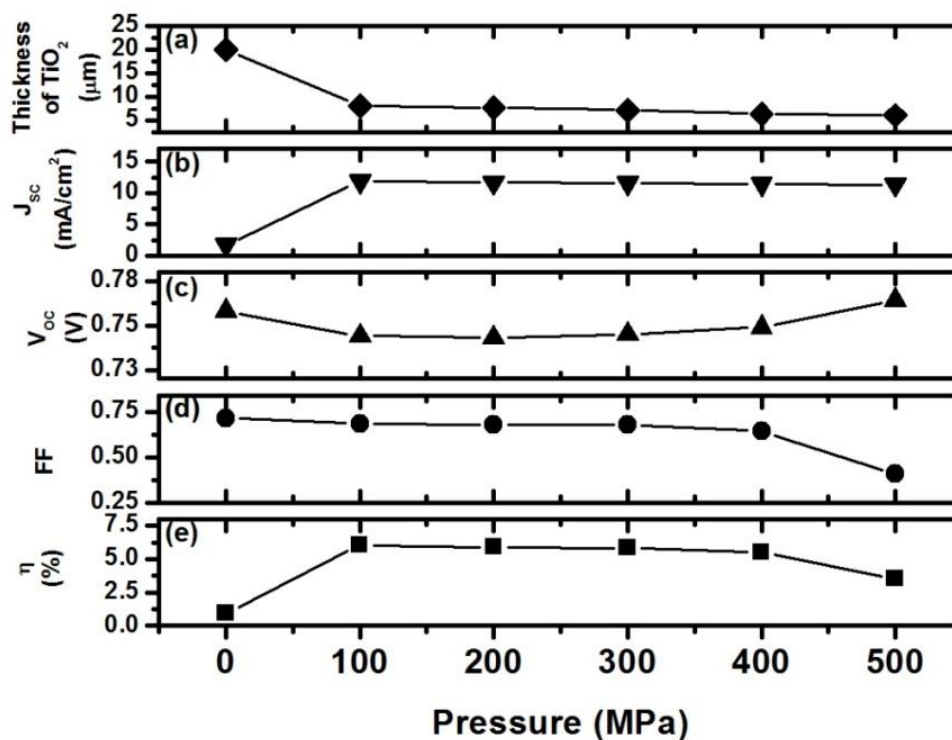


Fig. 5-1. The correlation between the compression pressure of the electrophoretic deposited TiO<sub>2</sub> thin film and device performance. The parameters of the non-compressed photoanode were plotted at the 0 MPa position. The electrolyte (EL 3) is 0.4 M LiI, 0.4 M TBAl, 0.04M I<sub>2</sub> and 0.5 M NMBI in AN/MPN mixture (v/v=1:1). The PV characteristics were measured under one sun irradiation (AM 1.5G, 100 mW·cm<sup>-2</sup>).

Figure 5-2 shows the influence of compression time on J<sub>SC</sub> and conversion efficiency. By compressing TiO<sub>2</sub> film 1 sec at P = 100 MPa, J<sub>SC</sub> and conversion efficiency (η) reach 11.45 mA/cm<sup>2</sup> and 6.05 %, but only slightly improving the cell performance is made with increasing the compression time. Minimum compression time for achieving relatively high energy-conversion efficiencies is a very important issue in the future of roll-to-roll process applications.





## 5.2 Photovoltaic characteristic of multiple electrophoresis deposition

For low-temperature fabricated DSCs especially by electrophoresis deposition (EPD), the volatile organic compounds such as isopropyl alcohol (IPA), methanol, or ethanol were the solvent of the binder-free suspension or paste. Cracks in the film would constantly occur after air-drying that degraded the device performance. We applied one-step and two-steps EPDs separately in this experiment to deposit P-90 TiO<sub>2</sub> NPs onto ITO/PEN flexible substrates. For one-step EPD, we applied a constant current density of 20 A cm<sup>-2</sup> for 5 mins; whereas, two-step EPD was performed twice for 2.5 mins with the same conditions but via air-drying the sample between the steps. The charge density in EPD stayed constant in these two processes.

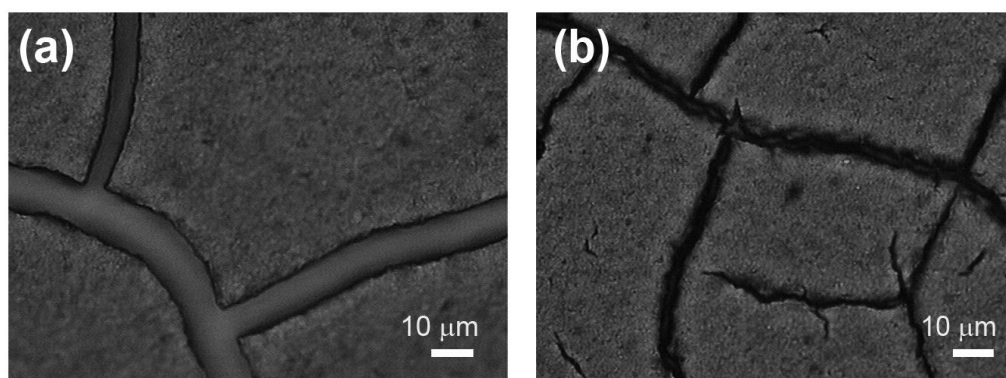


Fig. 5-3. The microscopy pictures of electrophoretically deposited P-90 TiO<sub>2</sub> film on ITO/PEN film by one-step process (a) and two-step process (b) before 100MPa compression.

Table 5-1. . Dye-sensitized solar cell performances with one-step or two-step EPD preparation methods. All photoanodes were compressed by 100 MPa pressure prior to device assembly.

Method	Process EPD current density [time] ( $\mu\text{A cm}^{-2}$ [min])	$J_{\text{sc}}$ ( $\text{mA cm}^{-2}$ )	$V_{\text{oc}}$ (mV)	FF	$\eta$ (%)
One-step	20 [5]	8.81	780	0.595	4.09
Two-steps	20 [2.5]+ 20 [2.5]	8.94	784	0.690	4.83

- The film thickness is about 5  $\mu\text{m}$  after 100MPa compression.
- The electrolyte (EL 3) is 0.4 M LiI, 0.4 M TBAl, 0.04M  $\text{I}_2$  and 0.5 M NMBI in AN/MPN mixture (v/v=1:1).
- The PV characteristics were measured under one sun irradiation (AM 1.5G, 100  $\text{mW cm}^{-2}$ ).

Fig. 5-3 shows the surface morphology examined by an optical microscope, illustrating the interconnected P-90  $\text{TiO}_2$  NPs thin film. Huge microcracks in the one-step process deposited films (Fig. 5-3 (a)) are wider and deeper than those of the two-steps ones (Fig. 5-3 (b)). These results suggest that the 2<sup>nd</sup> EPD could fill the cracks produced in the 1<sup>st</sup> EPD to form a better quality microstructure photoanode. To understand the role of thin films made by the one-step and two-step EPDs in DSC devices, three photoanodes for each method were prepared and assembled into DSC devices, whose performances are listed in Table 5-1. Because the same deposition charges density of 6  $\text{mC cm}^{-2}$  prepared all DSCs, we obtained a similar thickness of 5  $\mu\text{m}$  with almost the same  $J_{\text{sc}}$  and  $V_{\text{oc}}$  of about 8.94  $\text{mA cm}^{-2}$  and 0.784 V. However, slightly improving the filling factor (FF) from 0.595 to 0.690 for the one made of two-step EPD may explain the fewer cracks of EPD film. In this plastic-based DSC with two-steps EPD photoanode, we achieved a conversion efficiency of 4.83%. The

two-step EPD photoanode has better film quality to improve the DSC device efficiency.

In order to enhance the dye absorption and increase the thickness of the mesoporous photoanode made by EPD, we increased the total deposition charge density from 6 to 12 mC cm<sup>-2</sup>. Meanwhile, to clarify the effect of the device performance by different deposition rates, we varied the EPD current density from 20 to 5 μA cm<sup>-2</sup>. Table 5-2 provides the performance data of various DSCs. By increasing the applied EPD current density, the deposition thickness, as expected, increases from 5 to 20 μA cm<sup>-2</sup>. The higher applied EPD current density causes the higher internal EPD voltage (or electric field), thus, the TiO<sub>2</sub> NPs in the solvent could easily overcome the gravity and friction force of the solvent. In contrast with the V<sub>oc</sub>, J<sub>sc</sub> increases with the TiO<sub>2</sub>-film thickness because the more photoanode surface area with the thicker film not only enhances the dye loading but also creates more inhomogeneous light intensity in the

Table 5-2. Dye-sensitized solar cell performances with two-steps EPD preparation methods by various EPD currents and time.

Process EPD current density [time] (μA cm <sup>-2</sup> [min] )	L (μm)	J <sub>sc</sub> (mA cm <sup>-2</sup> )	V <sub>oc</sub> (V)	FF	(%)
20 [5]+ 20 [5]	ca. 10.1	10.86	0.723	0.654	5.13
10 [10]+ 10[10]	ca. 6.8	10.11	0.751	0.646	4.92
5 [20]+ 5 [20]	ca. 5.2	8.45	0.781	0.710	4.68

- The symbol L stands for the P-90 TiO<sub>2</sub> film thickness after 100MPa pressure.
- The electrolyte (EL 3) is 0.4 M LiI, 0.4 M TBAI, 0.04M I<sub>2</sub> and 0.5 M NMBI in AN/MPN mixture (v/v=1:1).
- The PV characteristics were measured under one sun irradiation (AM 1.5G, 100 mW cm<sup>-2</sup>).

film, decreasing the effective Fermi level of TiO<sub>2</sub> photoanode.

The DSCs with the slowest deposition rate (5 μA cm<sup>-2</sup>; 20 mins) have the highest filling factor of 0.71. This result suggests that the slower deposition rate, the better quality of TiO<sub>2</sub> photoanode is - although the most efficient DSCs with a conversion efficiency of 5.13% was obtained using a two-step EPD with current density of 20 μA cm<sup>-2</sup> for 5 mins in each step. The reason is because thicker TiO<sub>2</sub> film provides a larger area for dye adsorption.

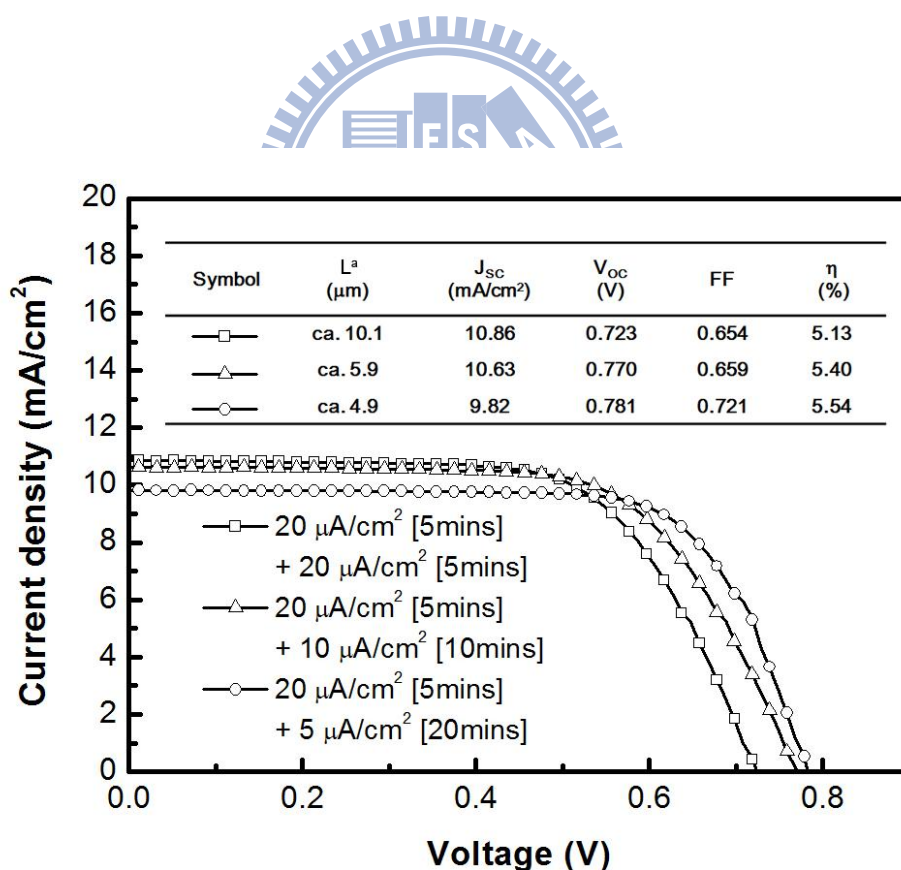


Fig. 5-4. The effect of different 2<sup>nd</sup> EPD TiO<sub>2</sub> photoanode on J-V curve of DSC. The inset table shows the detail photovoltaic parameters under AM 1.5G one sun irradiation. The electrolyte (EL 3) is 0.4 M LiI, 0.4 M TBAI, 0.04M I<sub>2</sub> and 0.5 M NMBI in AN/MPN mixture (v/v=1:1). a. The symbol L stands for the TiO<sub>2</sub> film thickness after 100MPa pressure.

The cracks produced in the 1<sup>st</sup> EPD film could be filled in the 2<sup>nd</sup> EPD and the larger applied current density provides the faster deposition rate. We therefore further prepared the DSCs with three deposition rates for the 2<sup>nd</sup> TiO<sub>2</sub> EPD, i.e., (20  $\mu\text{A cm}^{-2}$ ; 5 mins), (10  $\mu\text{A cm}^{-2}$ ; 10 mins), and (5  $\mu\text{A cm}^{-2}$ ; 20 mins), but with the same 1<sup>st</sup> EPD condition (20  $\mu\text{A cm}^{-2}$ ; 5 mins). Figure 5-4 shows the current density–voltage (J–V) curves of these three devices. The inset table summarizes the corresponding thickness (L) of TiO<sub>2</sub> film after 100 MPa pressure, short-circuit current ( $J_{\text{SC}}$ ), open-circuit voltage ( $V_{\text{OC}}$ ), fill factor (FF), and solar-to-electricity conversion efficiency ( $\eta$ ).

Although we maintained the same product of current density and deposition time in the three samples, the results reveal quite large difference in film thickness. The slowest deposition rate for a 4.9  $\mu\text{m}$  thick device and the fastest deposition rate for 10.1  $\mu\text{m}$  one indicates that the cracks produced after drying the 1<sup>st</sup> EPD film may have been filled up more at the slow EPD rate than at the fast rate; therefore the thickness of TiO<sub>2</sub> film is not linearly proportionate to the 2<sup>nd</sup> EPD rate. With increasing photoanode thickness from 4.9 to 10.1  $\mu\text{m}$ ,  $V_{\text{oc}}$  decreases from 0.781 V to 0.723V, whereas,  $J_{\text{SC}}$  mainly ascribed to the enlargement of the surface area for dye adsorption. The fastest deposited (thickest) DSC is only 1  $\text{mA cm}^{-2}$  larger than that of the slowest (thinnest) deposited one. We acquired maximal FF of 0.721 and a conversion

efficiency of 5.54% for the DSC fabricated with the slowest 2<sup>nd</sup> deposition rate (5  $\mu\text{A cm}^{-2}$ ).

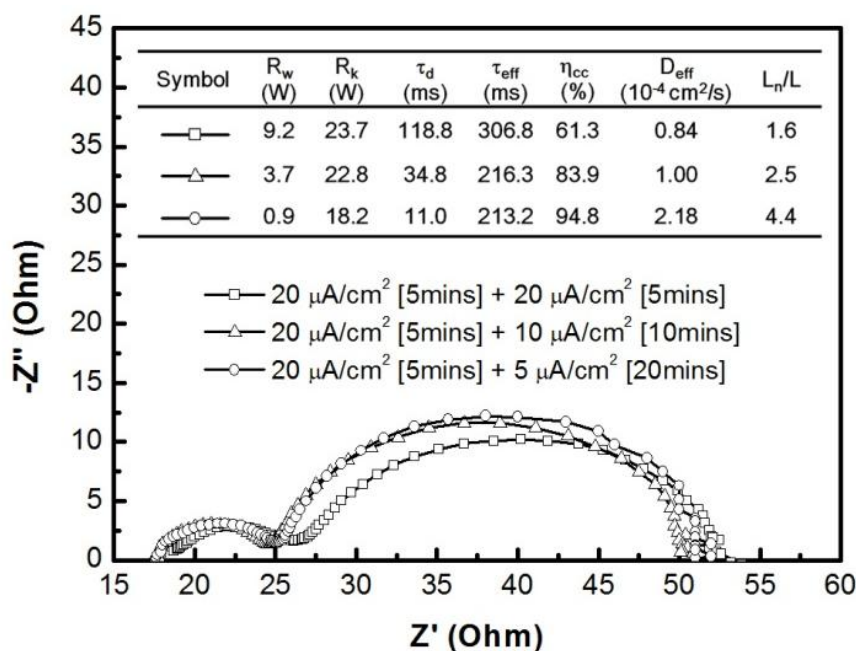


Fig. 5-5. The Nyquist plots of DSC device with the different 2<sup>nd</sup> EPD  $\text{TiO}_2$  photoanode. The data was measured at  $V_{OC}$  under AM 1.5 one-sun irradiation and fitted based on the equivalent circuit model as shown in Fig 2-7. The inset table listed the detail fitting parameters of photoanode. The electrolyte (EL 3) is 0.4 M LiI, 0.4 M TBAI, 0.04M  $\text{I}_2$  and 0.5 M NMBI in AN/MPN mixture (v/v=1:1).

To investigate the interfacial charge transfer processes occurring in the each component of DSCs, the electrochemical impedance spectroscopy (EIS), such as the photoanode, electrolyte, and Pt counter electrode [66, 67], has been used widely. Figure 5-5 compares the Nyquist plots of the DSCs with different 2<sup>nd</sup> EPD rates which were analyzed and fitted with the well-known transmission-line impedance model (Fig. 2-7) which is discussed in Chapter 2 and also used in the research of this thesis [39, 80]. The 1<sup>st</sup> semicircle (in the kHz range) typically stands for the behavior of the Pt

counter electrode, and the 2<sup>nd</sup> semicircle, determined by only one parameter,  $(\omega_k/\omega_d) = (R_K/R_W)$ , represents the impedances related to charge-transfer processes in the TiO<sub>2</sub> photoanode [67].

The inset table of Fig. 5-5 summarizes the fitting results, suggesting that the charge-transfer resistance ( $R_W$ ) decreases by about 1 order of magnitude by reducing the 2<sup>nd</sup> EPD rate of the TiO<sub>2</sub> film from 20  $\mu\text{A cm}^{-2}$  to 5  $\mu\text{A cm}^{-2}$ . The slower 2<sup>nd</sup> EPD rate provides better fill-in for the cracks formed during drying of the 1<sup>st</sup> EPD film for more efficient electron transport pathway in the TiO<sub>2</sub> photoanode. The effective electron lifetime ( $\tau_{\text{eff}}$ ), the lifetime of electrons being recombined, and back-injection into the electrolyte is inversely proportional to the fitting peak frequency ( $\omega_{\text{max}}$ ) of the 2<sup>nd</sup> semicircle in the case of  $R_K \gg R_W$ . The effective electron diffusion time in TiO<sub>2</sub> photoanode ( $1/\omega_d$ ), given as  $\omega_d = \omega_k/(R_K/R_W)$ , decreases from 118.8 to 18 ms as the 2<sup>nd</sup> EPD rate decreases. The effective electron diffusion coefficient in the photoanode ( $D_{\text{eff}}$ ) is calculated using the relation:  $D_{\text{eff}} = (R_K/R_W)(L^2/\tau_{\text{eff}})$ , where  $L$  is the thickness of photoanode. An efficient  $D_{\text{eff}}$  of  $2.18 \times 10^{-5} \text{ cm}^2 \text{ s}^{-1}$  was obtained from the DSC made with the slowest 2<sup>nd</sup> EPD rate at 5  $\mu\text{A cm}^{-2}$ . The electron diffusion length expresses the competition between the collection and the recombination of electrons. The effective diffusion length ( $L_n$ ) can be expressed as  $L_n = (D_{\text{eff}} \tau_{\text{eff}})^{0.5}$ . As shown in Fig. 5-5, the obtained  $L_n/L$  increases about three times by decreasing the 2<sup>nd</sup> EPD rate from

20  $\mu\text{A cm}^{-2}$  to 5  $\mu\text{A cm}^{-2}$ . All the fitting parameters from EIS analysis indicate that the DSC devices with the higher quality  $\text{TiO}_2$  film deposited by the slower deposition rate (5  $\mu\text{A cm}^{-2}$ ) have more efficient electron transport in the photoanode to achieve a higher conversion efficiency of 5.54%.

### 5.3 Effect of light scattering layer

Through multiple EPDs, including slow 2<sup>nd</sup> EPD to completely fill the cracks produced in drying 1<sup>st</sup> EPD film and the fast-deposited (20  $\mu\text{A cm}^{-2}$  deposition current density for 5 mins deposition) scattering layer of 100nm  $\text{TiO}_2$  NPs, the scattering layer efficiently scattered sunlight, especially for long wavelengths.

The cross-section SEM images of the three kinds of EPD  $\text{TiO}_2$  films are showed in Figure 5-6 (a) that are composed of  $\text{TiO}_2$  crystalloid nanoparticles (NPs) with a porous structure. The P-90 NPs size is about 15 nm and the optically scattering  $\text{TiO}_2$  NPs is about 100 nm (also denoted by 100 nm  $\text{TiO}_2$ ). The 100 nm  $\text{TiO}_2$  was well deposited on the transparent film composed by P-90 NPs without any lager pinholes and these three kinds of  $\text{TiO}_2$  films were prepared to device assembling.



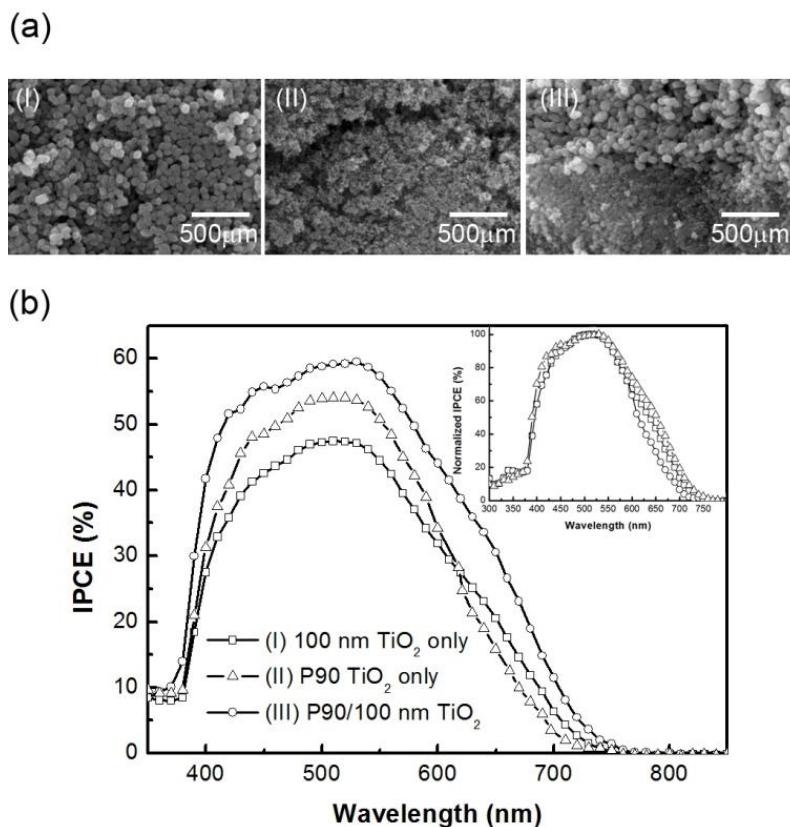


Fig. 5-6. (a) Cross-section SEM image of an EPD film for (I) 100 nm TiO<sub>2</sub>; (II) P90 TiO<sub>2</sub>; (III) P90 TiO<sub>2</sub> and 100nm TiO<sub>2</sub> as double-layer film on ITO/PEN substrate. (b) IPCE spectra and normalized IPCE spectra (inset figure) of DSCs with these three kinds of nanocrystalline TiO<sub>2</sub> film. The electrolyte (EL 3) is 0.4 M LiI, 0.4 M TBAI, 0.04M I<sub>2</sub> and 0.5 M NMBI in AN/MPN mixture (v/v=1:1).

Figure 5-6(b) shows the typical monochromatic incident photon-to-electron conversion efficiency (IPCE) spectra, which is to scale the spectral response of the photovoltaic devices. Around the distinct peak at 540 nm attributed to the metal-to-ligand charge transfer absorption band of the N719 dye, the DSCs with only P-90 NPs were obtained the IPCE value about 54 % which was greater than the ones with only 100 nm NPs (IPCE value about 47 %) because of the greater amount of the N719 dye on TiO<sub>2</sub> film. The DSCs consisting of both P-90 and 100nm NPs showed the greatest IPCE value of 60 % due to enough surface area for dye absorption with

good light scattering. The inset of Fig. 5-6(b) presents the normalized IPCE of three kinds of DSCs. The shapes of the three IPCE curves are almost the same in the wavelength range of 400–600 nm. On the other hand, in the wavelength range above 600 nm, the IPCE of DSC consisting of 100 nm TiO<sub>2</sub> NPs is greater than the P-90 one, meaning of the lack of the light-scattering effect for P-90 NPs. It suggests that the high IPCE in DSCs based on relatively thin films can be improved by enhanced light absorption with enough surface area for dye absorption and good light scattering layer with larger size NPs, which was consistent with the work reported by H. Arakawa, *et al.* in 2004 [81]. On the other hand, a good quality film with no crack is necessary for electron collection that may also lead to an improvement in IPCE.

Finally, Fig. 5-6 shows the excellent photovoltaic performance without an antireflection layer under AM 1.5G one sun irradiation. Its short circuit current density ( $J_{SC}$ ), open circuit voltage ( $V_{OC}$ ), and filling factor (FF) are 12.06 mA cm<sup>-2</sup>, 0.763 V, and 0.72 respectively, yielding an overall conversion efficiency ( $\eta$ ) of 6.63%.

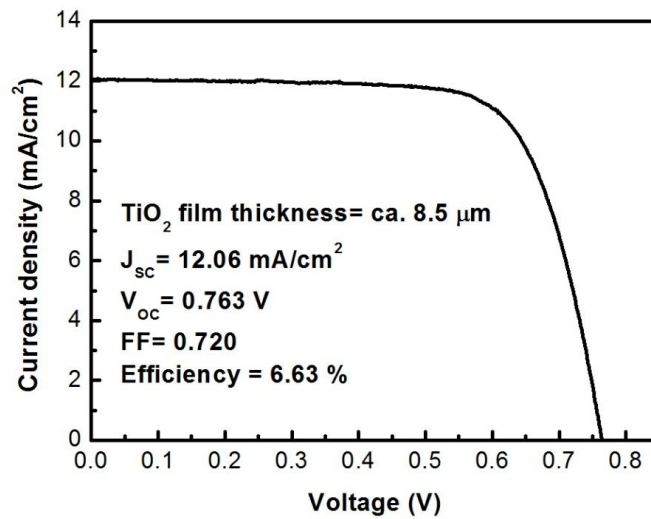


Fig. 5-7. PV characteristics of nanocrystalline TiO<sub>2</sub> DSCs with TiO<sub>2</sub> photoanode deposited multiply by P-90 and 100nm NPs measured under AM 1.5G sun irradiation using 0.238 cm<sup>2</sup> size of black mask. The electrolyte (EL 3) is 0.4 M LiI, 0.4 M TBAI, 0.04M I<sub>2</sub> and 0.5 M NMBI in AN/MPN mixture (v/v=1:1).

## 5.4 Long-term stability testing

Before investigating the durability of plastic DSC, it is important to test the stability of ITO/PEN in electrolyte and to check the sealing material and condition in the plastic cell. Figure 5-8(a) shows the variation of sheet resistance of ITO/PEN immersed in two electrolytes for 1000 h which are electrolyte 6 (EL 6 : 0.5 M PMII/0.05 M I<sub>2</sub> in MPN) and electrolyte 7 (EL 7 : 0.5 M LiI/0.05 M I<sub>2</sub> in MPN). The sheet resistance of ITO/PEN immersed in electrolyte I increases slightly from 11.2 to 12.2 ohm sq<sup>-1</sup>; however, that in electrolyte II increases significantly from 11.1 to 18.6 ohm sq<sup>-1</sup>. The OM images of ITO/PEN surface are also showed in Figure 3b, which clearly observed by cracking phenomenon of ITO film after immersing in electrolyte II for 1000 h.

This indicates that the ITO/PEN film in the electrolyte containing LiI is unstable, implying a chemical etching reaction. [82]

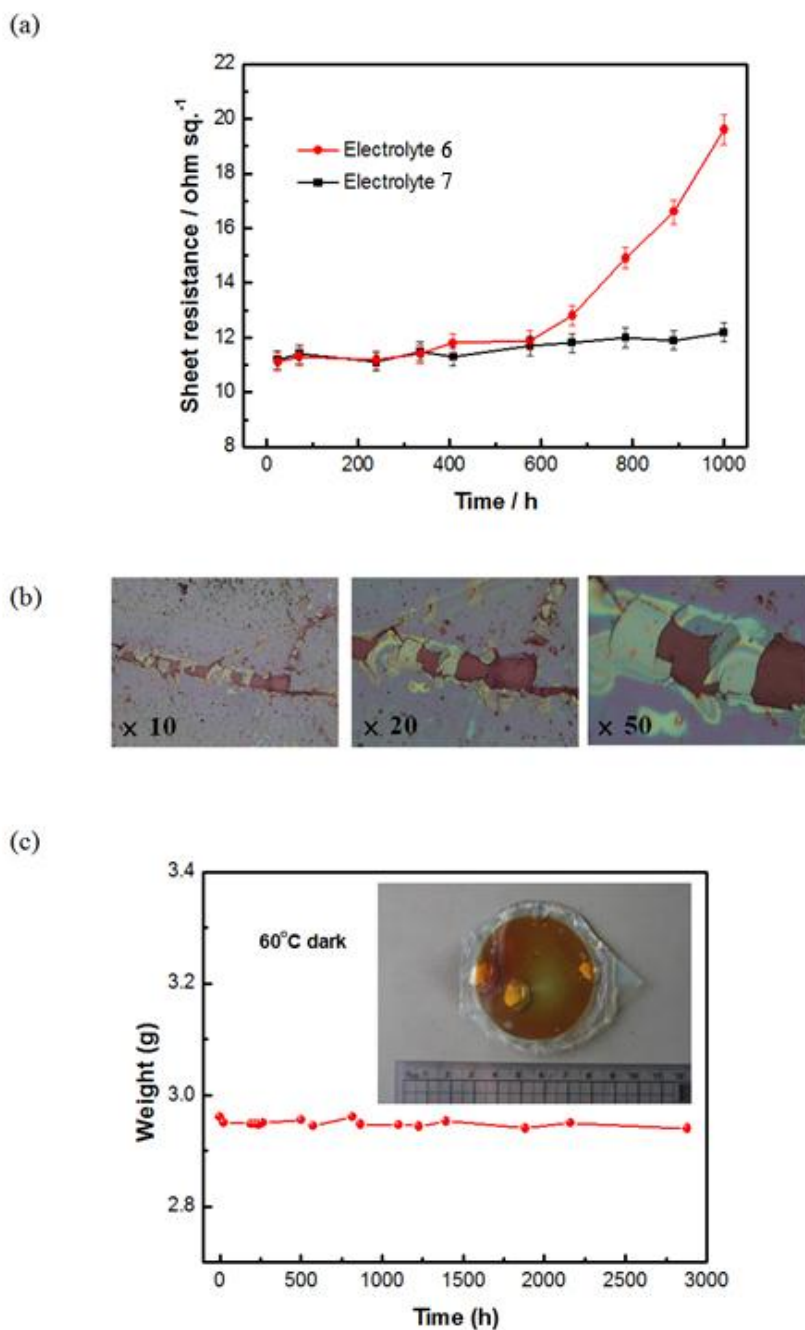


Fig. 5-8. (a) The relationship between the sheet resistance of ITO/PEN and the immersion time in electrolyte at 60 °C. (electrolyte 6: 0.5 M PMII and 0.05 M I<sub>2</sub> in MPN; electrolyte 7: 0.5 M LiI and 0.05 M I<sub>2</sub> in MPN). (b) The OM images of ITO/PEN film after immersion in electrolyte II at 60 °C. (c) The sealing test cell and the weight loss of cell during thermal treatment at 60 °C in the dark.

A 60 $\mu$ m hot-melt type spacer was used to seal the test cell for preventing the electrolyte from leaking. After heat-sealing at 125 °C for 10 sec, the electrolyte consisted of 0.8M PMII/0.1M I<sub>2</sub>/0.5M NMBI in MPN was injected in the spacer between two electrodes through the injection holes. The injection holes and edge of the test cell were then sealed with a UV glue and cured under UV light for 15 sec. Figure 5-8(c) presents the test cell structure (inset image) and the weight loss data. The weight loss was only -0.43 % after more than 2700 h at 60 °C in dark, indicating that the sealing condition was sufficient to avoid electrolyte leakage in plastic DSCs.

For light aging test, the performance of the devices was tested under continuous light irradiation (100 mW cm<sup>-2</sup>) at 60 °C. It increases to a maximum initially then maintains at a steady state after 100 h as shown in Fig. 5-9. The apparent increase in J<sub>SC</sub> and conversion efficiency may be due to improvement in electrolyte penetration into the mesoporous TiO<sub>2</sub> film, lowering of the TiO<sub>2</sub> conduction band boundary and activation of the Pt-coated counter electrode as reported previously. [83] Note that devices exhibit different conversion efficiency improvements with different cation iodides. In Fig. 5-9, J<sub>SC</sub> and conversion efficiency of the device with electrolyte I increased significantly from 3.81 to 6.89 mA cm<sup>-2</sup> and from 1.85 % to 3.14 %, respectively, under 100 h continuous light irradiation. On the other hand, the device with electrolyte II achieves an efficiency value of 2.38 % from the initial value of 1.84

%, which  $J_{SC}$  only slightly increases from 4.03 to 4.81  $\text{mA cm}^{-2}$  in Fig. 5-9. This improvement results from  $\text{TBA}^+$  on the  $\text{TiO}_2$  film surface that protected the voids in the dye-coated  $\text{TiO}_2$  film in turn blocked undesirable interfacial charge recombination and suppressed surface protonation. The gradual decrease in conversion efficiency of cell after 100 h in Fig. 5-9(b) suggests that the conformation, dye alignment, and intermolecular interactions of N719 on the surface of  $\text{TiO}_2$  film should change during the aging process.

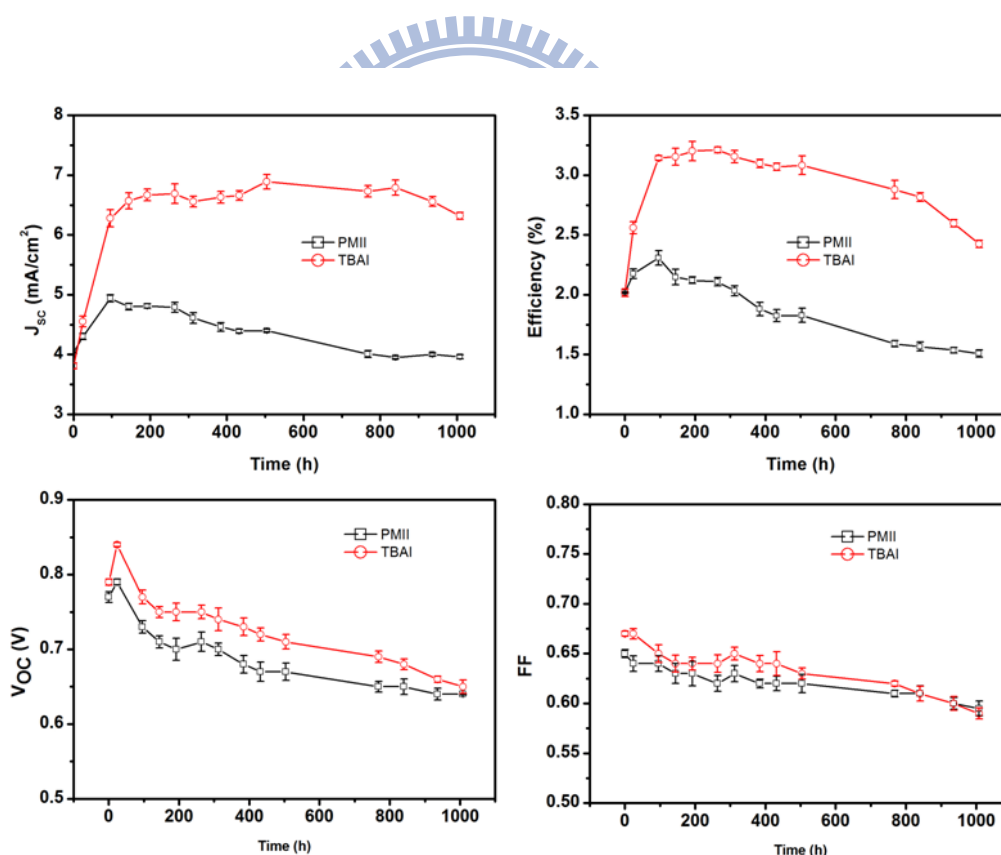


Fig. 5-9. Photovoltaic parameters ( $J_{SC}$ ,  $V_{OC}$ , FF and  $\eta$ ) for plastic DSC with TBAI or PMII after visible light soaking (1 sun) at 60 °C. The TBAI electrolyte (EL 4) is 0.8 M TBAI, 0.1 M  $\text{I}_2$ , and 0.5 M NMBI in MPN. The PMII electrolyte (EL 5) is 0.8 M PMII, 0.1 M  $\text{I}_2$ , and 0.5 M NMBI in MPN.

To fairly evaluate device durability, the photovoltaic parameters of the devices at the steady state obtained after 100 h aging were used as a baseline. After continuous aging for 1000 h, the devices with electrolytes I and II still maintained 96.9 % and 72.3 % of the baseline efficiency measured at 100 h. This performance is better than that of previously reported. [82, 84] The major factor of degradation in the efficiency of the devices is due to a decrease of  $V_{oc}$  ( $\sim 0.13$  V) that is caused by surface protonation under the accelerated aging test. [19, 85]

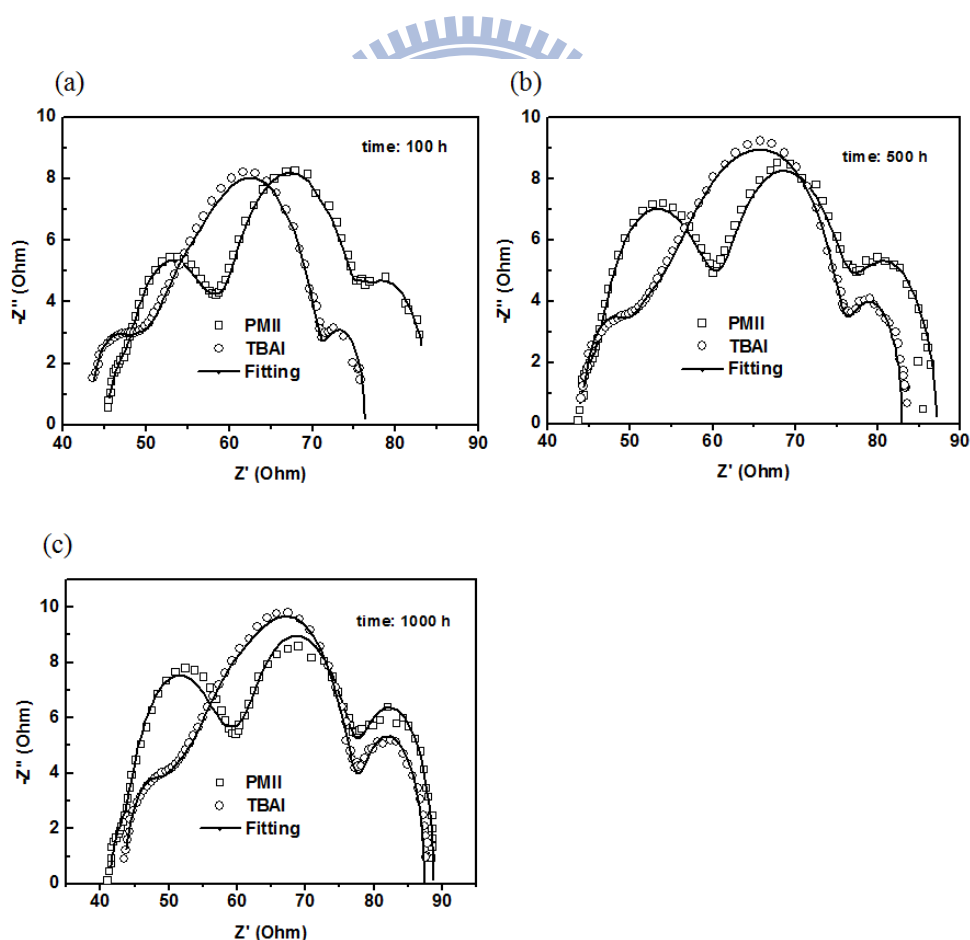


Fig. 5-10. EIS results of plastic DSCs with different iodides under one sun light soaking for (a) 100, (b) 500, and (c) 1000 h. The data was measured at  $V_{oc}$  under AM 1.5 one-sun irradiation and fitted based on the equivalent circuit model as shown in Fig 2-7. The TBAI electrolyte (EL 4) is 0.8 M TBAI, 0.1 M  $I_2$ , and 0.5 M NMBI in MPN. The PMII electrolyte (EL 5) is 0.8 M PMII, 0.1 M  $I_2$ , and 0.5 M NMBI in MPN.

To understand the effects of different cation iodides, TBAI and PMII, on charge transportation and device durability, the EIS of the devices aged for 100, 500, and 1000 h were measured under open-circuit condition and illumination of 100 mW cm<sup>-2</sup>. Figures 5-10(a) to (c) show the Nyquist plots of the impedance data.

Table 5-3. Parameters determined from fitting EIS data of plastic DSC with electrolytes containing TBAI and PMII, respectively.

Iodide	Light aging time (h)	R <sub>w</sub> (Ω)	R <sub>k</sub> (Ω)	R <sub>k</sub> /R <sub>w</sub>	τ <sub>eff</sub> (ms)	D <sub>eff</sub> (10 <sup>-5</sup> cm <sup>2</sup> s <sup>-1</sup> )	L <sub>n</sub> (μm)
TBAI	100	12.9	13.5	1.05	36.8	1.02	6.2
	500	12.6	13.2	1.05	44.2	0.85	6.1
	1000	18.8	14.4	0.77	48.4	0.57	5.3
PMII	100	28.9	13.2	0.46	16.6	0.99	4.1
	500	37.4	14.3	0.38	15.3	0.90	3.7
	1000	41.4	14.4	0.35	14.5	0.86	3.5

a. The data was measured at V<sub>OC</sub> under AM 1.5 one-sun irradiation and fitted based on the equivalent circuit model as shown in Fig 2-7.

b. The TBAI electrolyte (EL 4) is 0.8 M TBAI, 0.1 M I<sub>2</sub>, and 0.5 M NMBI in MPN.

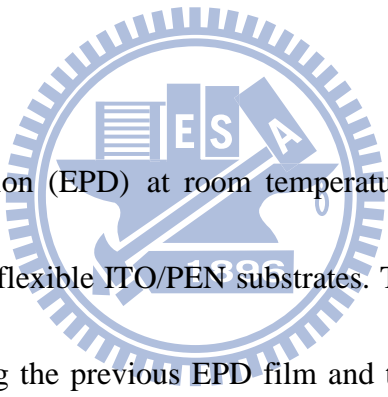
c. The PMII electrolyte (EL 5) is 0.8 M PMII, 0.1 M I<sub>2</sub>, and 0.5 M NMBI in MPN.

The EIS-fitting data from these devices are listed in Table 5-3. The R<sub>w</sub> values increase with light soaking time for electrolyte containing either TBAI or PMII that lowers the estimated electron diffusion coefficient (D<sub>eff</sub>) and shortens the diffusion length,  $L_n = L(R_k/R_w)^{1/2}$ , where L is the thickness of TiO<sub>2</sub> film. However, the effective electron lifetime, τ<sub>eff</sub>, increases with the light soaking time. It implies that



the recombination of electrons with triiodide at the interface of TiO<sub>2</sub> NPs and the electrolyte has inhibited during the prolonged stability test resulting in a stable photocurrent output. Furthermore, the device with electrolyte I has a higher resistance of charge transfer at the Pt/electrolyte interface than that with electrolyte II as shown in Figure 5-10. This means that the electrolyte containing TBAI had a lower triiodide reduction rate at the Pt/electrolyte interface that leads to the lower FF value as shown in Fig. 5-9.

## 5.5 Summary



Electrophoretic deposition (EPD) at room temperature and compress treatment prepare TiO<sub>2</sub> thin films on flexible ITO/PEN substrates. The multiple EPDs filled up the cracks caused by drying the previous EPD film and the slow 2<sup>nd</sup> deposition rate obtained a high conversion efficiency of 5.54%. EIS analyzed the great enhancement of the electron collection which improved the electron diffusion coefficient about 1 order of magnitude in crack-less multiple-EPD TiO<sub>2</sub> films. When the 100nm TiO<sub>2</sub> NPs was deposited on P-90 EPD film in a DSC, the device shows the best photovoltaic performance with an energy conversion efficiency of 6.63% due to the 100nm TiO<sub>2</sub> NPs efficiently scattered sunlight, especially in long wavelength region.

The durability of flexible devices with different cation iodides also has been

demonstrated. Under prolonged one-sun light-irradiation and 60 °C-thermal stress aging, our plastic DSC devices showed an initial improvement in performance of 96.9 % followed by an extended steady-state period of more than 1000h. The presence of TBAI in the electrolyte provides higher photocurrent and better durability. This improvement is a result of TBA<sup>+</sup> on the TiO<sub>2</sub> film surface, which sterically protects the voids in the dye-coated TiO<sub>2</sub> film in turn blocks undesirable interfacial charge recombination to suppress surface protonation.



# Chapter 6 Conclusions and Perspectives

## 6.1 Conclusion

In this thesis, my main objectives can be separated into two parts: (I) The hierarchical ZnO photoanode electrode (PE) composed by tetrapod-like ZnO (T-ZnO) nanoparticles (NPs) (II) The multiple electrophoresis deposition (EPD) method to reduce the micro crack on the PE. The main goal is to realize and develop a good PE for high performance DSC.

First, the D149-sensitized tetrapod-like ZnO DSC is demonstrated with 4.9% conversion efficiency through a trade-off solution to optimize the electron transport properties and the photoanode surface area. The outstanding electron transport ability of ZnO tetrapod network is also investigating by the electron diffusion coefficient  $D_{\text{eff}} = 1.53 \times 10^{-3} \text{ cm}^2 \text{ s}^{-1}$  and the effective electron diffusion length  $L_n = 46 \text{ }\mu\text{m}$ . On the other hand, by using the time-response photocurrent transients and the electrochemical impedance spectrum analysis, the tetrapod-like ZnO DSCs have better solar conversion efficiency and larger short-circuit photocurrent than that made of commercial powders as a result of the tetrapod-like framework provides a suitable structure of efficient ionic diffusion. Finally, the tetrapod-like ZnO photoanode with

efficient electron conductivity in it and good ion diffusion ability in its pore is easy to make mass production with a screen-printing method or doctorblade method, in contrast to other 1D nanostructure photoanodes. And the concept of tetrapod structure powder is also suitable to other semiconductor PE in DSCs for future applications.

Second, the preparation of PE at low temperature causes many micro cracks on/in PE which degrade the photovoltaic (PV) performance of DSCs. We provide a multiple electrophoretic deposition (EPD) method to reduce the micro cracks by filling up the cracks and enhance the PV performance (from 4.09% conversion efficiency to 5.54%). The great enhancement results in the electron collection that improves the electron diffusion coefficient about 1 order of magnitude in crack-less multiple-EPD TiO<sub>2</sub> films analyzed by EIS. The highest conversion efficiency of 6.63 is obtained by EPD in the 100nm TiO<sub>2</sub> NPs to make the light harvesting more efficient. On the other hand, the long-term stability is tested by replacing the non-volatile solvent of electrolyte. The presence of TBAI in the electrolyte provides higher photocurrent and better durability than PMII one. This improvement is a result of TBA<sup>+</sup> on the TiO<sub>2</sub> film surface, which sterically protects the voids in the dye-coated TiO<sub>2</sub> film in turn blocks undesirable interfacial charge recombination to suppress surface protonation. Finally, the plastic DSC devices showed an initial improvement

in performance of 96.9 % followed by an extended steady-state period of more than 1000h.

## 6.2 Perspectives

The electron collection and dye-loading area (light harvesting) is the most important tasks of photoanode electrode (PE) to make a high efficiency cell. However, these two tasks are trade-off missions. The thinner thickness of PE has better electron collection, and the thicker thickness one has the larger surface area to anchor the dye molecular for improving the light harvesting. And the film quality of PE is also a main issue to affect the electron collection efficiency. So, at this stage, the PE with unique optical structure, such as photonic crystal structure or surface plasma enhanced structure, to minimize the film thickness and to hugely increase the light harvesting may be the next research topic.

# References

- [1] *I.E.O.* Energy Information Administration, July 2010.
- [2] United Nations Development Programme (UNDP) World Energy Assessment, New York (2000).
- [3] [http://en.wikipedia.org/wiki/List\\_of\\_photovoltaic\\_power\\_stations](http://en.wikipedia.org/wiki/List_of_photovoltaic_power_stations).
- [4] T. Markvart, Solar electricity. 2nd Edition, John Wiley & Sons, Chichester, 2000.
- [5] K.A. Tsokos, Physics for the IB Diploma Fifth edition, Cambridge University Press, 2008.
- [6] R. Audubert, *C. Compt. rend.*, 194 (1932) 1124.
- [7] K.J. Wu X, Dhery RG, DeHart C, Duda A, Gessert TA, Asher S, Levi DH, Sheldon P., in: Proceedings of the 17th European Photovoltaic Solar Energy Conference, Munich, 2001, pp. 995–1000.
- [8] M.A. Green, K. Emery, Y. Hishikawa, W. Warta, Progress in Photovoltaics: Research and Applications, 19 (2010) 84-92.
- [9] C.P. Wojtczuk S, Zhang X, Derkacs D, Harris C, Pulver D, Timmons M., in: 35th IEEE PVSC, Honolulu.
- [10] [http://en.wikipedia.org/wiki/Abundance\\_of\\_elements\\_in\\_Earth%27s\\_crust](http://en.wikipedia.org/wiki/Abundance_of_elements_in_Earth%27s_crust)
- [11] M.K. Nazeeruddin, A. Kay, I. Rodicio, R. Humphry-Baker, E. Mueller, P. Liska, N. Vlachopoulos, M. Graetzel, Journal of the American Chemical Society, 115 (1993) 6382-6390.
- [12] M. K. Nazeeruddin, P. Pechy, M. Gratzel, Chemical Communications, (1997) 1705-1706.
- [13] Q. Wang, W.M. Campbell, E.E. Bonfantani, K.W. Jolley, D.L. Officer, P.J. Walsh, K. Gordon, R. Humphry-Baker, M.K. Nazeeruddin, M. Grätzel, The Journal of Physical Chemistry B, 109 (2005) 15397-15409.
- [14] L. Luo, C. J. Lin, C.S. Hung, C.F. Lo, C.Y. Lin, E.W.G. Diau, Physical Chemistry Chemical Physics, 12 (2010) 12973-12977.
- [15] T. Horiuchi, H. Miura, K. Sumioka, S. Uchida, Journal of the American Chemical Society, 126 (2004) 12218-12219.
- [16] A. Mishra, M.K.R. Fischer, P. Bäuerle, Angewandte Chemie International Edition, 48 (2009) 2474-2499.
- [17] A. Hagfeldt, M. Grätzel, Chemical Reviews, 95 (1995) 49-68.
- [18] P. Wang, S.M. Zakeeruddin, J.E. Moser, M.K. Nazeeruddin, T. Sekiguchi, M. Grätzel, Nat Mater, 2 (2003) 402-407.
- [19] C.-Y. Chen, M. Wang, J.-Y. Li, N. Pootrakulchote, L. Alibabaei, C.-h. Ngoc-le, J.-D. Decoppet, J.-H. Tsai, C. Grätzel, C.-G. Wu, S.M. Zakeeruddin, M. Grätzel, ACS

- Nano, 3 (2009) 3103-3109.
- [20] M. Grätzel, *Journal of Photochemistry and Photobiology A: Chemistry*, 164 (2004) 3-14.
- [21] Y. Saito, W. Kubo, T. Kitamura, Y. Wada, S. Yanagida, *Journal of Photochemistry and Photobiology a-Chemistry*, 164 (2004) 153-157.
- [22] U. Bach, D. Lupo, P. Comte, J.E. Moser, F. Weissortel, J. Salbeck, H. Spreitzer, M. Grätzel, *Nature*, 395 (1998) 583-585.
- [23] N.G. Park, J. van de Lagemaat, A.J. Frank, *The Journal of Physical Chemistry B*, 104 (2000) 8989-8994.
- [24] E.M. Kaidashev, M. Lorenz, H.v. Wenckstern, A. Rahm, H.-C. Semmelhack, K.-H. Han, G. Benndorf, C. Bundesmann, H. Hochmuth, M. Grundmann, *Applied Physics Letters*, 82 (2003) 3901-3903.
- [25] J.X. Wang, X.W. Sun, Y. Yang, H. Huang, Y.C. Lee, O.K. Tan, L. Vayssieres, *Nanotechnology*, 17 (2006) 4995-4998.
- [26] D.Y. Song, A.G. Aberle, J. Xia, *Applied Surface Science*, 195 (2002) 291-296.
- [27] F. Pan, C. Song, X.J. Liu, Y.C. Yang, F. Zeng, *Materials Science & Engineering R-Reports*, 62 (2008) 1-35.
- [28] W. Water, S.Y. Chu, Y.D. Juang, S.J. Wu, *Mater. Lett.*, 57 (2002) 998-1003.
- [29] D.R. Sahu, S.Y. Lin, J.L. Huang, *Applied Surface Science*, 252 (2006) 7509-7514.
- [30] J.B. Baxter, E.S. Aydil, *Applied Physics Letters*, 86 (2005).
- [31] M. Law, L.E. Greene, J.C. Johnson, R. Saykally, P.D. Yang, *Nat. Mater.*, 4 (2005) 455-459.
- [32] F. Xu, M. Dai, Y.N. Lu, L.T. Sun, *J. Phys. Chem. C*, 114 (2010) 2776-2782.
- [33] A.E. Suliman, Y.W. Tang, L. Xu, *Solar Energy Materials and Solar Cells*, 91 (2007) 1658-1662.
- [34] E. Hosono, Y. Mitsui, H.S. Zhou, *Dalton Transactions*, (2008) 5439-5441.
- [35] H.M. Cheng, W.H. Chiu, C.H. Lee, S.Y. Tsai, W.F. Hsieh, *J. Phys. Chem. C*, 112 (2008) 16359-16364.
- [36] C.T. Wu, W.P. Liao, J.J. Wu, *Journal of Materials Chemistry*, 21 (2011) 2871-2876.
- [37] H.M. Cheng, W.F. Hsieh, *Nanotechnology*, 21 (2010) 485202.
- [38] H.M. Cheng, W.F. Hsieh, *Energy & Environmental Science*, 3 (2010) 442-447.
- [39] W.H. Chiu, C.H. Lee, H.M. Cheng, H.F. Lin, S.C. Liao, J.M. Wu, W.F. Hsieh, *Energy & Environmental Science*, 2 (2009) 694-698.
- [40] C.H. Lee, W.H. Chiu, K.M. Lee, W.H. Yen, H.F. Lin, W.F. Hsieh, J.M. Wu, *Electrochim. Acta*, 55 (2010) 8422-8429.

- [41] Y.F. Hsu, Y.Y. Xi, C.T. Yip, A.B. Djuric, W.K. Chan, *Journal of Applied Physics*, 103 (2008).
- [42] Y. Li, F. Qian, J. Xiang, C.M. Lieber, *Materials Today*, 9 (2006) 18-27.
- [43] M.Y.A. Rahman, M.M. Salleh, I.A. Talib, M. Yahaya, *Ionics*, 11 (2005) 275-280.
- [44] G. Veerappan, K. Bojan, S.W. Rhee, *Acs Applied Materials & Interfaces*, 3 (2011) 857-862.
- [45] T.N. Murakami, S. Ito, Q. Wang, M.K. Nazeeruddin, T. Bessho, I. Cesar, P. Liska, R. Humphry-Baker, P. Comte, P. Pechy, M. Grätzel, *J. Electrochem. Soc.*, 153 (2006) A2255-A2261.
- [46] P.J. Li, J.H. Wu, J.M. Lin, M.L. Huang, Y.F. Huang, Q.G. Li, *Sol. Energy*, 83 (2009) 845-849.
- [47] G.R. Li, F. Wang, Q.W. Jiang, X.P. Gao, P.W. Shen, *Angew. Chem.-Int. Edit.*, 49 (2010) 3653-3656.
- [48] K. Suzuki, M. Yamaguchi, M. Kumagai, S. Yanagida, *Chemistry Letters*, 32 (2003) 28-29.
- [49] K. Imoto, M. Suzuki, K. Takahashi, T. Yamaguchi, T. Komura, J. Nakamura, K. Murata, *Electrochemistry*, 71 (2003) 944-946.
- [50] W.J. Hong, Y.X. Xu, G.W. Lu, C. Li, G.Q. Shi, *Electrochemistry Communications*, 10 (2008) 1555-1558.
- [51] K.M. Lee, C.Y. Hsu, P.Y. Chen, M. Ikegami, T. Miyasaka, K.C. Ho, *Physical Chemistry Chemical Physics*, 11 (2009) 3375-3379.
- [52] K. Kalyanasundaram, M. Grätzel, *Coordination Chemistry Reviews*, 177 (1998) 347-414.
- [53] N. Papageorgiou, W.F. Maier, M. Grätzel, *J. Electrochem. Soc.*, 144 (1997) 876-884.
- [54] G. Schlichthörl, S.Y. Huang, J. Sprague, A.J. Frank, *The Journal of Physical Chemistry B*, 101 (1997) 8141-8155.
- [55] S.Y. Huang, G. Schlichthörl, A.J. Nozik, M. Grätzel, A.J. Frank, *The Journal of Physical Chemistry B*, 101 (1997) 2576-2582.
- [56] P.J. Cameron, L.M. Peter, *The Journal of Physical Chemistry B*, 109 (2005) 7392-7398.
- [57] S. Lee, J.H. Noh, H.S. Han, D.K. Yim, D.H. Kim, J.-K. Lee, J.Y. Kim, H.S. Jung, K.S. Hong, *The Journal of Physical Chemistry C*, 113 (2009) 6878-6882.
- [58] S.-Q. Fan, B. Fang, H. Choi, S. Paik, C. Kim, B.-S. Jeong, J.-J. Kim, J. Ko, *Electrochim. Acta*, 55 (2010) 4642-4646.
- [59] [http://en.wikipedia.org/wiki/Air\\_mass\\_coefficient](http://en.wikipedia.org/wiki/Air_mass_coefficient)
- [60] K.i. Ishibashi, Y. Kimura, M. Niwano, *Journal of Applied Physics*, 103 (2008) 094507.



- [61] M. Wolf, H. Rauschenbach, *Advanced Energy Conversion*, 3 (1963) 455-479.
- [62] F.A. Lindholm, J.G. Fossum, E.L. Burgess, *Electron Devices, IEEE Transactions on*, 26 (1979) 165-171.
- [63] D. Gentilini, D. D'Ercole, A. Gagliardi, A. Brunetti, A. Reale, T. Brown, A. Di Carlo, *Superlattices and Microstructures*, 47 (2010) 192-196.
- [64] J. Bisquert, *Physical Chemistry Chemical Physics*, 5 (2003) 5360-5364.
- [65] J. Bisquert, G. Garcia-Belmonte, F. Fabregat-Santiago, N.S. Ferriols, P. Bogdanoff, E.C. Pereira, *The Journal of Physical Chemistry B*, 104 (2000) 2287-2298.
- [66] S. Ito, M. Grätzel, F. Fabregat-Santiago, I. Mora-Sero, J. Bisquert, T. Bessho, H. Imai, *The Journal of Physical Chemistry B*, 110 (2006) 25210-25221.
- [67] M. Adachi, M. Sakamoto, J. Jiu, Y. Ogata, S. Isoda, *The Journal of Physical Chemistry B*, 110 (2006) 13872-13880.
- [68] L. Grinis, S. Dor, A. Ofir, A. Zaban, *Journal of Photochemistry and Photobiology A: Chemistry*, 198 (2008) 52-59.
- [69] H. Tian, L. Liu, B. Liu, S. Yuan, X. Wang, Y. Wang, T. Yu, Z. Zou, *J. Phys. D-Appl. Phys.*, 42 (2009) 5.
- [70] D. Vanmaekelbergh, P.E. de Jongh, *The Journal of Physical Chemistry B*, 103 (1999) 747-750.
- [71] A.L. Roest, P.E. de Jongh, D. Vanmaekelbergh, *Physical Review B*, 62 (2000) 16926.
- [72] H.W. Ham, Y.S. Kim, *Thin Solid Films*, 518 (2010) 6558-6563.
- [73] Z.H. Xu Jie, Liang Guijie, Wang Luoxin, Weilin Xu, Cui Weigang, Zengchang Li, *Journal of the Serbian Chemical Society*, 75 (2010) 259-269.
- [74] W. Chen, H. Zhang, I.M. Hsing, S. Yang, *Electrochemistry Communications*, 11 (2009) 1057-1060.
- [75] M. Adachi, M. Sakamoto, J. Jiu, Y. Ogata, S. Isoda, *J. Phys. Chem. B*, 110 (2006) 13872-13880.
- [76] Q. Wang, S. Ito, M. Gratzel, F. Fabregat-Santiago, I. Mora-Sero, J. Bisquert, T. Bessho, H. Imai, *The Journal of Physical Chemistry B*, 110 (2006) 25210-25221.
- [77] W. Kubo, S. Kambe, S. Nakade, T. Kitamura, K. Hanabusa, Y. Wada, S. Yanagida, *The Journal of Physical Chemistry B*, 107 (2003) 4374-4381.
- [78] T. Yamaguchi, N. Tobe, D. Matsumoto, T. Nagai, H. Arakawa, *Solar Energy Materials and Solar Cells*, 94 (2010) 812-816.
- [79] H. Lindstrom, A. Holmberg, E. Magnusson, L. Malmqvist, A. Hagfeldt, *Journal of Photochemistry and Photobiology A: Chemistry*, 145 (2001) 107-112.
- [80] H.M. Cheng, W.F. Hsieh, *Energy & Environmental Science*, 3 (2010) 442-447.
- [81] Z.S. Wang, H. Kawauchi, T. Kashima, H. Arakawa, *Coordination Chemistry*

Reviews, 248 (2004) 1381-1389.

[82] M. Ikegami, J. Suzuki, K. Teshima, M. Kawaraya, T. Miyasaka, *Solar Energy Materials and Solar Cells*, 93 (2009) 836-839.

[83] Z. Zhang, S. Ito, J.-E. Moser, S.M. Zakeeruddin, M. Grätzel, *ChemPhysChem*, 10 (2009) 1834-1838.

[84] K.M. Lee, S.J. Wu, C.Y. Chen, C.G. Wu, M. Ikegami, K. Miyoshi, T. Miyasaka, K.C. Ho, *Journal of Materials Chemistry*, 19 (2009) 5009-5015.

[85] C.Y. Chen, N. Pootrakulchote, S.J. Wu, M. Wang, J.Y. Li, J.H. Tsai, C.G. Wu, S.M. Zakeeruddin, M. Grätzel, *The Journal of Physical Chemistry C*, 113 (2009) 20752-20757.



# Curriculum Vitae

---

Name: Chiu Wei-Hao

Date of Birth: Oct. 29, 1980

Sexuality: Male

Nationality: Taiwan



## Education

---

- 2004-2011 Ph.D. studies in Institute of Electro-Optical Engineering, National Chiao Tung University
- 2002-2004 MS studies in Institute of Electro-Optical Engineering, National Chiao Tung University
- 1998-2002 Undergraduate studies in Department of Physics, National Sun Yat-Sen University

## International Journal Papers

---

1. “Transverse excess noise factor and transverse mode locking in a gain-guided laser”  
Optics Communications 245, 301-308 (2005)  
Ching-Hsua Chen, Po-Tse Tai, **Wei-Hao Chiu**, Wen-Feng Hsieh
2. “Formation of branched ZnO nanowires from solvothermal method and dye-Sensitized solar cells applications”  
Journal of Physical Chemistry C 112, 16359 (2008)  
Hsin-Ming Cheng, **Wei-Hao Chiu**, Chia-Hua Lee, Song-Yeu Tsai, and Wen-Feng Hsieh
3. “Efficient electron transport in tetrapod-like ZnO metal-free dye sensitized solar cells”  
Energy & Environmental Science, 2, 694 (2009)  
**Wei-Hao Chiu**, Chia-Hua Lee, Hsin-Ming Cheng, Hsiu-Fen Lin, Shih-Chieh Liao, Jehn-Ming Wu and Wen-Feng Hsieh

4. Dye-sensitized solar cells with a micro-porous TiO<sub>2</sub> electrode and gel polymer electrolytes prepared by in situ cross-link reaction  
Solar Energy Materials and Solar Cells **93**, 2003-2007 (2009)  
Kun-Mu Lee, Chih-Yu Hsu, **Wei-Hao Chiu**, Meng-Chin Tsui, Yung-Liang Tung, Song-Yeu Tsai, and Kuo-Chuan Ho
  
5. “Effects of Mesoscopic Poly(3,4-ethylenedioxythiophene) Films as Counter Electrodes for Dye-Sensitized Solar Cells”  
Thin Solid Films, **518**, 1716-1721 (2010)  
Kun-Mu Lee, **Wei-Hao Chiu**, Hung-Yu Wei, Chih-Wei Hu, Vembu Suryanarayanan , Weng-Feng Hsieh and Kuo-Chuan Ho
  
6. “Influence of tetrapod-like ZnO morphology and electrolytes on energy conversion efficiency of dye-sensitized solar cells”  
Electrochimica Acta, **55**, 8422-8429(2010)  
Chia-Hua Lee, **Wei-Hao Chiu**, Kun-Mu Lee, Wen-Hsiang Yen, Hsiu-Fen Lin , Wen-Feng Hsieh, Jenn-Ming Wu
  
7. “High efficiency flexible dye-sensitized solar cells by multiple electrophoretic deposition processes”  
Journal of Power Sources **196**, 3683-3687 (2011)  
**Wei-Hao Chiu**, Kun-Mu Lee, and Wen-Feng Hsieh
  
8. “Improved performance of flexible dye-sensitized solar cells by introducing an interfacial layer on Ti substrates”  
Journal of Materials Chemistry **21**, 5114-5119 (2011)  
Chia-Hua Lee, **Wei-Hao Chiu**, KunMu Lee, Wen-Feng Hsieh, and Jenn-Ming Wu
  
9. “Improvement on the long-term stability of flexible plastic dye-sensitized solar cells”  
Journal of Materials Chemistry (Accepted)  
Kun-Mu Lee, **Wei-Hao Chiu**, Ming-De Lu, and Wen-Feng Hsieh

## Conference Papers

---

1. "Branched ZnO nanowires for enhancing energy conversion efficiency of dye-Sensitized Solar Cells"  
2008 MRS-T (中華民國材料科學學會年會), Paper No. P07-008 (佳作)  
Hsin-Ming Cheng, **Wei-Hao Chiu**, Chia-Hua Lee, Song-Yeu Tsai, and Wen-Feng Hsieh
2. "Branched ZnO nanowires for enhancing energy conversion efficiency of dye-Sensitized Solar Cells"  
2008 International Symposium on Solar Cell Technologies (ISSCT), Paper No. DP-007  
Hsin-Ming Cheng, **Wei-Hao Chiu**, Chia-Hua Lee, Song-Yeu Tsai, and Wen-Feng Hsieh
3. "The influence of the iodine concentrations in ionic liquid-type electrolyte"  
2008 International Symposium on Solar Cell Technologies (ISSCT)  
Yung-Liang Tung, Jia-Yin Wu, **Wei-Hao Chiu**, Jen-An Chen, Hsin-Yi Hsu
4. "Excellent electron diffusion property in tetrapod-like ZnO metal-free dye sensitized solar cell"  
3rd INTERNATIONAL CONFERENCE on the INDUSTRIALISATION of DSC (2009)  
**Wei-Hao Chiu**, Chia-Hua Lee, Hsin-Ming Cheng, Hsiu-Fen Lin, and Wen-Feng Hsieh
5. "Tetrapod-shaped ZnO nanostructure film as photoelectrode in dye-sensitized solar cells"  
3rd INTERNATIONAL CONFERENCE on the INDUSTRIALISATION of DSC (2009)  
Chia-Hua Lee, **Wei-Hao Chiu**, Hsin-Ming Cheng, Hsiu-Fen Lin
6. "High-Efficiency ZnO Nanoparticle Based Dye-Sensitized Solar Cells with Metal-Free Indoline Sensitizers"  
2009 MRS-T (中華民國材料科學學會年會)  
Hsin-Ming Cheng , **Wei-Hao Chiu** , and Wen-Feng Hsieh

7. "Tetrapod-like ZnO metal-free dye-sensitized solar cells with outstanding electron transport properties"  
2009 Conference on Optics and Photonics Taiwan (OPT)  
**Wei-Hao Chiu**, Chia-Hua Lee, Hsin-Ming Cheng, Hsiu-Fen Lin, Shih-Chieh Liao, Jenn-Ming Wu and Wen-Feng Hsieh
8. Performances of tetrapod-like ZnO dye-sensitized solar cells with ionic liquid electrolyte  
2009 International Symposium on Dye-Sensitized Solar Cells (Taiwan)  
**Wei-Hao Chiu**, Kun-Mu Lee, Hsin-Ming Cheng, and Wen-Feng Hsieh
9. Hierarchical frameworks film assembled by tetrapod-like nanoparticles for dye-sensitized solar cells applications  
2010 中華民國物理年會  
**Wei-Hao Chiu**, Hsin-Ming Cheng, Kun-My Lee, Chia-Hua Lee, Meng-Chin Ysui, Hsiu-Fen Lin Shih-Chieh Liao, Wen-Feng Hsieh
10. CYC B6L 老化探討  
5th Aseanian conference on dye-sensitized and organic solar cell  
Yung-Liang Tung, Meng-Chin Tsui, Yao-Shan Wu, Kun-Mu Lee, Sz-Ping Fu,  
**Wei-Hao Chiu**, and Chun-Guey Wu
11. Fabrication of high quality TiO<sub>2</sub> thin films for high conversion efficiency dye-sensitized solar cells by multiple electrophoresis depositions  
2010 International Conference on Solid State Devices and Materials (SSDM 2010)  
**Wei-Hao Chiu**, Kun-Mu Lee, and Wen-Feng Hsieh
12. Efficient flexible dye-sensitized solar cells with high quality TiO<sub>2</sub> photoanode prepared by multiple electrophoresis deposition  
2010 Conference on Optics and Photonics Taiwan (OPT)  
**Wei-Hao Chiu**, Kun-Mu Lee, and Wen-Feng Hsieh
13. Surface passivation: effects of CDCA co-adsorbent on the durability of dye-sensitized solar cells  
2010 Conference on Optics and Photonics Taiwan (OPT)  
Kun-Mu Lee, **Wei-Hao Chiu**, Chia-Yuan Chen, Shi-Jhang Wu, Jia-Yin Wu, Yao-Shan Wu, Chuan-Ya Hung and Chun-Guey Wu